A dissertation for the degree of PhD in Science

Study of the characteristics of pulsating aurora using multi-point high-speed optical observations

多地点高速光学観測を用いた脈動オーロラの性質に関する研究

Yuki Kawamura

Graduate School of Informatics and Engineering

The University of Electro-Communications

Supervisor: Professor Keisuke Hosokawa

March 2021

Study of the characteristics of pulsating aurora using multi-point high-speed optical observations

多地点高速光学観測を用いた脈動オーロラの性質に関する研究

Screening Committee:
Chief Examiner: Prof. Keisuke Hosokawa
Member: Associate Prof. Takuo Tsuda
Member: Prof. Yasuhide Hobara
Member: Associate Prof. Toshiharu Kojima
Member: Prof. Naoto Kishi

概要

脈動オーロラ (Pulsating Aurora: PsA) は、数秒から数十秒の変化 (主脈動) の上に秒以下の細かい変動 (内部変調) が重畳する階層的周期構造を有するディフーズオーロラの一種である。本論文では、複数地点に設置された高速光学観測機器を用いて、PsA の階層的周期構造の制御機構について議論する。第 1 章では、本論文の背景を述べる。第 2 章では、本論文に用いる高速光学観測機器について紹介する。第 3 章では、PsA 電子のエネルギー推定手法を紹介し、そのエネルギーが多様であり、朝方に行くほど、そのエネルギーが高くなる傾向にあることを示す。第 4 章では、第 3 章で示した PsA 電子のエネルギーの多様性に基づき、その最大の特徴である階層的周期構造の生成機構を議論する。第 5 章では研究全体を総括し、今後の展望を述べる。

Abstract

Pulsating aurora (PsA) is a type of diffuse aurora showing characteristic hierarchical temporal variations with subsecond fluctuations (internal modulation) superimposed on slower variations (main pulsation). Simultaneous ground-based and satellite observations have recently revealed that these hierarchical temporal variations are characterized by magnetospheric chorus waves (e.g., *Nishimura et al.*, 2010). In addition, the hierarchical temporal variations of PsA are reportedly due to the periodicity of the chorus waves as well as the transit time required for electrons, which contribute to PsA emission, to precipitate from the magnetosphere to the ionosphere (*Miyoshi et al.*, 2010; *Nishiyama et al.*, 2014). However, the formation mechanism of the hierarchical temporal variations, which are the most distinctive feature of PsA, is still unclear. The reason is that conventional ground-based observations are designed to be conducted simultaneously with satellite observations and do not have sufficient temporal resolution to capture the internal modulation, which occurs on subsecond time scales, over a wide field of view. In this thesis, we discuss the generation mechanism of the hierarchical temporal variations of PsA by investigating the energy of the PsA electrons through multipoint high-speed observations. In Chapter 1, we provide a general introduction to the research presented in this thesis and describe the characteristics of PsA. In Chapter 2, we present detailed information about the ground-based optical instruments employed in this work.

In Chapter 3, we present a statistical analysis of the lifetime of $O(^1S)$ to determine the emission altitude of PsA using a ground-based five-wavelength photometer that has been operating in Tromsø, Norway, since February 2017. The PsA intervals were extracted using an electron-multiplying charge-coupled device (EMCCD) all-sky imager for 37 nights from January to March 2018. By performing a cross-correlation analysis between the time series of the auroral emissions at 427.8 nm (N_2^+ first negative band) and 557.7 nm (oxygen emission), the distribution of the $O(^1S)$ lifetime was derived. The mean lifetime was 0.67 s, and the mode was approximately 0.70 s. The emission altitude of the PsA was estimated from the lifetime of $O(^1S)$; subsequently, a case study was conducted in which we compared the temporal variation of the emission altitude with the peak height of E region ionization, which was obtained from simultaneous observations by the European Incoherent SCATter (EISCAT) UHF radar. We confirmed overall agreement

between the two parameters, indicating the feasibility of the current method for estimating the energy of precipitating electrons causing PsA. In addition, we derived the statistical characteristics of the emission altitude of PsA. The result shows that the emission altitude is lower on the morning side than in the midnight sector, which indicates that the PsA electrons have higher energies in the later magnetic local time (MLT) sector. In particular, the emission altitude decreases at approximately 06 MLT. However, the model calculation suggests that the energy of cyclotron resonance between magnetospheric electrons and whistler-mode chorus waves does not vary significantly with MLT. This result implies that the observed change in the emission altitude cannot be explained solely by the MLT dependence of the resonance energy.

In Chapter 4, we present an analysis of the characteristics of multiple temporal variations (the main pulsation and internal modulation) of PsA using four EMCCD all-sky imagers in Scandinavia. We analyzed an interval in which an intense PsA was observed simultaneously at all four stations. The period of the main pulsation generally ranged from 4 to 8 s, and the dominant frequency of the internal modulation was approximately 3 Hz. These results are in good agreement with those obtained in previous studies, confirming the validity of the present approach. We found that 43% of all PsA cases are accompanied by internal modulations of $\sim$3 Hz. More interestingly, the internal modulation was less frequent at higher latitudes. To discuss the factors controlling these characteristics of the internal modulation, we reproduced the time series of PsA emissions by considering the time delay from the occurrence of chorus waves in the magnetosphere to the arrival of scattered electrons at the ionosphere. The simulation suggested that the internal modulation can be smeared due to the integrated contributions of PsA electrons, which exhibit different energies and reach the ionosphere with different time delays. This smearing effect is more effective at higher latitudes because of the longer magnetic field lines. Hence, this mechanism can explain the observational result that the internal modulation was less frequent at higher latitudes. Thus, we found that the temporal variation of PsA, especially their subsecond modulation, does not reflect the time series of chorus waves and is rather largely influenced by the delay time of PsA electrons.

The results presented in Chapters 3 and 4 demonstrate that the energy of PsA electrons ranges from 5 to 30 keV and the nature of the hierarchical temporal variations of PsA is determined not only by the amplitude variation of the chorus waves in the magnetosphere, but also by the variation in the delay time of PsA electrons, whose energy ranges from 5

to 30 keV from the magnetosphere to the ionosphere. Because the variation in the delay time depends on the energy of PsA electrons, its effect is expected to be less significant (i.e., the internal modulation is expected to be clearer) in PsA caused by higher-energy electrons. Thus, we conclude that the variation in electron energy plays a significant role in characterizing the hierarchical temporal variations of PsA. This finding further implies that the discreteness (i.e., visibility) of the internal modulation can be used as an indicator of the energy of the precipitating electrons causing a PsA.

Acknowledgments

The author would like to express his utmost gratitude to Professor Keisuke Hosokawa at The University of Electro-communications (UEC) for his outstanding supervision and encouragement of the research conducted as a part of this thesis. The author has learned many things under his supervision. In particular, he inspired the author to think effectively, ask questions, and consider assumptions. Further, he taught the author how to present research in a way that is easy to understand. This thesis could not have been completed without his supervision.

Dr. Shin-ichiro Oyama at the Institute for Solar-Earth Environment (ISEE) of Nagoya University is also gratefully acknowledged for his contributions. He supported the author throughout his research. Further, he provided the author with an opportunity to join a bilateral project of Japan and Russia. The author is grateful to Associate Professor Yasunobu Ogawa at the National Research Institute of Polar Research (NIPR) for providing support and insightful suggestions with regard to ground-based optical data. The author would like to express his special thanks to Professor Yoshizumi Miyoshi at the ISEE of Nagoya University for providing several valuable recommendations related to the theory of plasma waves in the magnetosphere. The author would like to sincerely acknowledge Associate Professor Satonori Nozawa at ISEE of Nagoya University for his kindness and helpful assistance with regard to handling the data of the five-wavelength photometer. The author wishes to express his hearty thanks to Associate Professor Satoshi Kurita at the Research Institute for Sustainable Humanosphere of Kyoto University for his useful instructions regarding satellite data processing and to Dr. Jun Sakai, Associate Professor Takuo Tsuda, Dr. Toru Takahashi, Dr. Mariko Teramoto, and Dr. Yuta Hozumi for their kind suggestions regarding this research. Professor Andrei Demekhov at the Polar Geophysical Institute (PGI) of Russia is also gratefully acknowledged for giving the author an opportunity to present his research at a Russian workshop and giving special advice

about skiing. The author expresses his appreciation to Mr. Kazu Okamura, Mr. Kohei Takami, Mr. Suguru Kawamura, Mr. Taiki Kishiyama, Mr. Satoshi Ebukuro, Mr. Sota Nanjo, Mr. Haruo Narikawa, and Mr. Shunpei Abe for their useful suggestions regarding this research.

The author is supported by a grant offered by a research fellowship of the Japan Society for the Promotion of Science (JSPS) for Young Scientists. The work described in Chapter 3 was supported by the Japan Society for the Promotion of Science (JSPS) Kakenhi (15H05747, 17H02968, JPJSBP12019814, 20H01959, and 20J12913). The work in Chapter 4 was supported by JSPS Kakenhi (15H05747, 16H06286, and 20J12913) and by a JSPS Bilateral Open Partnership Joint Research Project (JPJSBP120194814).

The author thanks the director and staff of EISCAT for operating the facility and supplying the relevant data. EISCAT is an international association supported by research organizations in China (CRIPR), Finland (SA), Japan (ISEE and NIPR), Norway (NFR), Sweden (VR), and the United Kingdom (UKRI).

Data from the EMCCD all-sky imagers were obtained from the ERG Science Center operated by the Institute of Space and Astronautical Science of the Japan Aerospace eXploration Agency (JAXA) and ISEE of Nagoya University (https://ergsc.isee.nagoya-u.ac.jp/index.shtml.en, *Miyoshi et al.*, 2018). The operation of the instruments in Tromsø was supported by the Tromsø Geophysical Observatory (TGO) at the Arctic University of Norway (UiT). The operation of the all-sky imagers in Sodankylä was supported by the Sodankylä Geophysical Observatory (SGO). The operation of the all-sky imagers in Tjautjas was supported by the Swedish Institute of Space Physics (IRF). The operation of the EMCCD all-sky imager in Kevo was supported by the Finnish Meteorological Institute (FMI) and Turku University.

Finally, I would like to express my deepest gratitude to my family for their continuous encouragement, especially my parents, who encouraged me to proceed with my research during graduation.

Contents

Abstract **i**

Acknowledgments **ix**

List of figures **xviii**

List of tables **xix**

1 Introduction **1**

1.1 Research field of this thesis 1

1.1.1 Magnetosphere 1

1.1.2 Ionosphere 3

1.1.3 Substorm 5

1.2 Particle motion in the magnetosphere 7

1.2.1 Magnetic mirror 8

1.2.2 Equatorial pitch angle 9

1.2.3 Loss cone 9

1.3 Aurora 10

1.3.1 Auroral emission 10

1.3.2 Types of aurora 11

1.4 Pulsating aurora 13

1.4.1 Morphology 13

1.4.2 Emission and ionization altitude 15

1.4.3 Temporal characteristics 16

1.4.4 Generation mechanism 22

1.5 Open questions and motivation of the thesis 26

2 Instruments **28**

2.1 Five-wavelength photometer 28

2.2 EMCCD all-sky imagers 31

3 Estimation of the emission altitude of pulsating aurora using the five-wavelength photometer **35**

3.1 Introduction 35

3.2 Instruments and datasets 37

3.3 Methodology for estimating the lifetime of $O(^1S)$ 38

3.4 Statistics of distribution of the lifetime of $O(^1S)$ 40

3.5 Calculating the effective altitude of pulsating aurora 41

3.6 Accuracy of estimating of the emission altitude 43

3.7 Dependence of altitude of pulsating aurora on magnetic local time 45

3.8 Discussion 46

3.9 Conclusions 47

4 Factors controlling the internal modulation of pulsating aurora: Multi-point high-speed optical observations in Scandinavia **49**

4.1 Introduction 49

4.2 Instruments and Datasets 51

4.3 Method 53

4.4 Results 57

4.4.1 Distribution of multiple temporal variations of PsA 57

4.4.2 Proportion of the internal modulation 59

4.5 Discussion 60

4.6 Conclusions 68

5 Concluding remarks **70**

5.1 Summary and conclusions 70

5.2 Future work 72

Publications **74**

References **77**

List of Figures

1.1 Schematic diagram of the large-scale structure of the Earth's magnetosphere. . . . 3
1.2 Altitude profiles of the main constituents of the ionosphere. This figure is from *Johnson* (1966). . . . 4
1.3 Altitude profiles of rates of collisional ionization by precipitating electrons from the magnetosphere. This figure is from *Rees* (1989). . . . 5
1.4 Schematic diagram of auroral development during auroral substorm. This figure is from *Akasofu* (1964). . . . 7
1.5 Auroral image taken by the crew of the International Space Station. This image was obtained from the Earth Science and Remote Sensing Unit, NASA Johnson Space Center, The Gateway to Astronaut Photography of Earth (eol.jsc.nasa.gov). . . . 12
1.6 Occurrence distribution of PsA versus MLT. The dotted line indicates the number of observed events. The dashed line indicates the number of observed PsA events at each MLT. The dot-dashed line indicates the occurrence rate of PsA events among all observations. This figure is from *Jones et al.* (2011). . . . 14
1.7 MLT distribution of observed PsA events (upper panel) and occurrence distribution of the E region peak height (h_mE) (lower panel). The occurrence rate is self-normalized in the lower panel. This figure is from *Hosokawa and Ogawa* (2015). . . . 16

1.8 Typical example of the 3 Hz modulation obtained from a narrow-field TV imager. Image taken by the narrow-field TV imager at 13:36:09 UT on February 10, 1975 (upper panel). Optical time series sampled in the white box in the top panel from 13:34:50 to 13:36:30 UT on the same day (lower panel). These figures are from *Royrvik and Davis* (1977). 18
1.9 Latitudinal dependence of the main pulsation of PsA. This figure is from *Duncan et al.* (1981). 19
1.10 Occurrence distribution of the period of the main pulsation (dashed line) and the duration of the ON phase (solid line) and OFF phase (shaded line). This figure is from *Yamamoto* (1988). 21
1.11 Histogram of the frequency of the internal modulation (upper left panel) and the period of the main pulsation (upper right panel). Scatter plots of the frequency of the internal modulation (lower left panel) and the period of the main pulsation (lower right panel) as a function of auroral intensity. This figure is from *Nishiyama et al.* (2014). 21
1.12 Frequency–time diagram of magnetic field observed by THEMIS satellite in 8 min interval (08:13–08:21 UT, October 15, 2008) (lower panel). Magnified view of 5 s indicated by red arrow in bottom panel (upper panel). This figure is from *Li et al.* (2012). 23
1.13 Schematic diagram of simultaneous observations conducted by *Nishimura et al.* (2010) (upper left panel). THEMIS satellite observations of bursts of chorus showing the frequency–time diagram of the electric field. White horizontal line indicates the local electron cyclotron frequency (f_{ce}), which is calculated from the measured magnetic field (upper right panel). Snapshots of the all-sky imager, which is projected to the geographic coordinates at 110 km. The red arrow indicates the PsA patch that shows the highest correlation with the chorus wave (lower left panel). Direct comparison between the amplitude variation of the chorus wave integrated over a frequency range of 0.05 to 0.5 f_{ce} and the optical time series of PsA at the highest correlation pixel (lower right panel). This figure is from *Nishimura et al.* (2010). 24

1.14 Direct comparison of the internal modulation of the PsA and the individual chorus elements. Magnified view of a single main pulsation of the PsA (upper left panel) and the corresponding bursts of chorus (lower left panel) from a simultaneous observation in Scandinavia. Magnified view of a single main pulsation (upper right panel) and the corresponding bursts of chorus (lower right panel) from a simultaneous observation in Alaska. This figure is from *Hosokawa et al.* (2020a). 25

2.1 Schematic diagram of the five-wavelength photometer. This figure is from *Nozawa et al.* (2018). 29

2.2 Time series of auroral emission at 427.8, 557.7, 630.0, 777.4, and 844.6 nm obtained with five-wavelength photometer during a 1 min interval from 03:39 to 03:40 UT on February 14, 2018. 30

2.3 EMCCD all-sky imager (Hamamatsu Photonics, C9100-23B) that was used in Tjautjas, Sweden. 31

2.4 Transmission characteristics of BG3 glass filter used on the EMCCD all-sky imagers. The vertical lines mark typical auroral emission lines (427.8, 557.7, and 630.0 nm). This figure is from *Hosokawa et al.* (2020b), which has been submitted to *J. Geophys. Res.: Space Phys.* 32

2.5 Typical example of the hierarchical temporal variations of PsA obtained with the EMCCD all-sky imager in Tjautjas, Sweden on March 15, 2018. Optical time series from 00:59 to 01:04 UT in the form of a south-to-north keogram (top panel), magnified view of the 1 min optical time series within the green box in the southern half of the top panel (middle panel), and two time series of the raw count sampled along the red and blue lines in the middle panel (bottom panel). This figure is from *Hosokawa et al.* (2020b), which has been submitted to *J. Geophys. Res.: Space Phys.* 34

3.1 **a** Image recorded by the EMCCD all-sky imager in Tromsø at 03:02:30 UT on February 24, 2018. The red circle indicates the FOV of the five-wavelength photometer. Time series of auroral emissions at **b** 427.8 nm and **c** 557.7 nm obtained from the five-wavelength photometer in a 1 min interval from 03:02 to 03:03 UT on the same day. 38

3.2 Time series of auroral emissions at **a** 427.8 nm and **b** 557.7 nm observed at Tromsø for a 1 min interval from 03:02 to 03:03 UT on February 24, 2018. **c** Comparison of time series of 557.7 nm (dashed line) and 427.8 nm (solid line) emissions. The time series of the 427.8 nm emission is delayed by 0.67 s, which corresponds to the lifetime of $O(^1S)$. 39
3.3 **a** Statistical distribution of the lifetime of $O(^1S)$. The distributions of the lifetime for three MLT sectors: **b** 20–03 MLT, **c** 03–05 MLT, and **d** 05–08 MLT. 41
3.4 Altitude profile of $n(O_2)$ obtained by MSIS model calculation. 43
3.5 **a** Altitude–time plot of the ionospheric raw electron density (i.e., power profile data) obtained by the EISCAT UHF radar during a PsA from 00:30 to 03:00 UT on February 19, 2018. **b** Time series of the emission altitude of the PsA estimated from the lifetime of $O(^1S)$ (blue line) and the peak height of E region ionization (h_mE) from the EISCAT UHF radar (red line). 44
3.6 **a** MLT distribution of intervals of PsA sampled from 37 nights of observations. **b** Dependence of PsA altitude on MLT. The red crosses and vertical bars indicate the average and standard deviation, respectively, of the PsA altitude calculated in each 1 h MLT bin. 45

4.1 Mosaic image of four EMCCD all-sky imager observations at 01:05:00 UT on March 15, 2018. 52
4.2 **a** South-to-north keogram from all-sky images taken in Tjautjas during a 10 s interval, from 01:03:20 to 01:03:30 UT, on March 15, 2018. **b** Time series of raw auroral luminosity along the horizontal black line in **a**. . . . 53
4.3 **a** Temporal variation of PsA observed by the EMCCD all-sky imager at Tjautjas during a 4 min interval from 01:01:00 to 01:04:00 UT on March 15, 2018. **b** Time derivative of the original time series in **a**. **c** Period–time diagram obtained by applying the S-transformation to the time-derivative time series in **b**. **d** Magnified view of the time series in **a** during a 10 s interval from 01:03:20 to 01:03:30 UT. **e** Component of the internal modulation obtained by subtracting the background trend of the main pulsation. **f** Frequency–time diagram obtained by applying the wavelet transform to the fluctuating component data in **e**. 56

4.4 Distributions of **a** period of main pulsation and **b** frequency of internal modulation during the 1 h interval analyzed in this study. 58
4.5 **a** Spatial distribution of PsAs with/without internal modulation at 01:00:00 UT on March 15, 2018. The red and blue dots indicate PsAs with/without internal modulation, respectively. **b** Latitudinal dependence of the percentage of PsAs with internal modulation. 60
4.6 Schematic diagram of TOF simulation from *Miyoshi et al.* (2010). 61
4.7 Variation of τ with electron energy between 5 and 30 keV for three L values (L = 5, 6, and 7). Colors indicate the chorus frequency f normalized by the electron gyrofrequency f_{ce}. 63
4.8 **a** Fundamental (input) time series with a modulation frequency of 3 Hz at a geographic latitude of 68.5°. **b** Time series of PsA emission reproduced considering the variation effect. **c** Frequency–time diagrams of the reproduced time series shown in **b**. 65
4.9 Latitudinal distribution of the wavelet amplitude of the internal modulation. 66
4.10 **a** Fundamental (input) time series with a modulation frequency of 3 Hz. **b**, **c** Reproduced time series of PsA emission at geographical latitudes of 66° (**b**) and 70° (**c**). 67

List of Tables

4.1 Locations of four EMCCD all-sky imagers in northern Scandinavia 51

Chapter 1

Introduction

The subject of this thesis is the characteristics of pulsating aurora (PsA). This chapter provides background information; the results are presented in subsequent chapters. Sections 1.1 and 1.2 provide general information about the space environment around the Earth and the motion of particles in this environment according to *Baumjohann and Treumann* (1997). Section 1.3 briefly introduces the auroral emission mechanism and types of auroras. Section 1.4 reviews the observations of PsA, and Section 1.5 describes the unresolved issues and motivation for this thesis.

1.1 Research field of this thesis

1.1.1 Magnetosphere

In this section, we describe the magnetosphere, which is the source of the electrons responsible for producing PsA, the main subject of the thesis. Earth is a magnetized planet with its own magnetic field. This magnetic field can be approximated by a dipole field, and the region dominated by this planetary magnetic field is called the magnetosphere. The Earth's dipole field can be approximated as follows:

$$B(\lambda, r_{eq}) = B_E(\frac{r_{eq}}{R_E})^{-3}\frac{(1+3\sin^2\lambda)^{\frac{1}{2}}}{\cos^6\lambda} \tag{1.1}$$

where r_{eq} is the radial distance to a particular magnetic field line on the equatorial plane of the magnetosphere, B_E is the equatorial magnetic field on the Earth's surface, and λ is the magnetic latitude. Here, for simplicity, the L value is introduced as a unit of distance.

$$L = \frac{r_{eq}}{R_E} \tag{1.2}$$

L is the largest distance to a magnetic field line in the equatorial plane in terms of the Earth's radius, R_E. By inserting equation 1.2 into equation 1.1, the Earth's dipole field can be expressed as

$$B(\lambda, L) = \frac{B_E}{L^3} \frac{(1 + 3\sin^2\lambda)^{\frac{1}{2}}}{\cos^6\lambda} \tag{1.3}$$

Figure 1.1 shows a schematic diagram of the large-scale structure of Earth's magnetosphere. The boundary between the Earth's magnetosphere and the solar wind is called the magnetopause. The magnetopause is usually located at a distance that is approximately equal to 10 R_E, but it penetrates inward beyond geostationary orbit (6.6 R_E) during periods of disturbance such as coronal mass ejections. A bow shock is thus formed because the solar wind is blocked by the magnetosphere. The bow shock is located at $\sim$13 R_E, where the kinetic energy of solar wind particles is converted to thermal energy. The region between the bow shock and the magnetopause is called the magnetosheath. The plasma in this region is compressed and is denser and hotter than typical plasma in the solar wind. The magnetosphere is highly stretched in the anti-sunward direction, and this stretched region is called the magnetotail. Hot plasma is stored in a region called the plasma sheet, which is near the central part of the magnetotail. The typical electron density, temperature, and intensity of the magnetic field in the plasma sheet are $n_e \sim 0.5$ cm^{-3}, $T_e \sim 5 \times 10^6$ K, and $B \sim 10$ nT, respectively. The plasma sheet is a source of the energetic particles that are responsible for the aurora. The thickness of the plasma sheet is a few R_E, and the regions outside the plasma sheet in the magnetotail are called lobes. Lobes are located on both the northern and southern sides of the plasma sheet, where the magnetic field pressure is higher than the plasma pressure. The average electron density, temperature, and magnetic field strength in the lobes are $n_e \sim 10^{-2}$ cm^{-3}, $T_e \sim 5 \times 10^5$ K, and $B \sim 30$ nT, respectively. The region of high-energy plasma on the near-Earth side of the plasma sheet is called the radiation belt or Van Allen belt. The L value of the radiation belt is 2–6 R_E, and particles in this region oscillate between mirror points located in the northern and southern hemispheres (see Section 1.2 for details). The intensity of the magnetic field ranges from 100 to 1000 nT, and the typical electron density and temperature are $n_e \sim 1$ cm^{-3} and $T_e \sim 5 \times 10^7$ K, respectively. The energy of particles in this region is very high, ranging from 30 keV up to several MeV. These energetic particles in the radiation belt are known to cause satellites to malfunction; therefore, understanding and predicting the variability of energetic particles in the radiation belt is important in

the framework of space weather. Further inside the radiation belt region is the plasmasphere, which is filled with cold ($T_e \sim 5 \times 10^3$ K) and dense ($n_e \sim 5 \times 10^2$ cm^{-3}) plasma originating from the outflow of the Earth's ionospheric plasma. In the equatorial plane, the plasmasphere extends to 4 R_E, and its boundary is called the plasmapause. At the plasmapause, the electron density decreases sharply to below 1 cm^{-3}.

When the dynamic pressure of the solar wind increases or when the magnetic field of the solar wind has a large southward component, the magnetosphere becomes more active, and various phenomena such as magnetic storms and magnetospheric substorms occur. These phenomena significantly change the plasma conditions in the magnetosphere and affect the ionosphere, which is connected to the magnetosphere via the magnetic field lines. The aurora is one of the most visible examples of such disturbances in near-Earth space. In the next section, we will introduce the Earth's ionosphere, the region in which auroras occur.

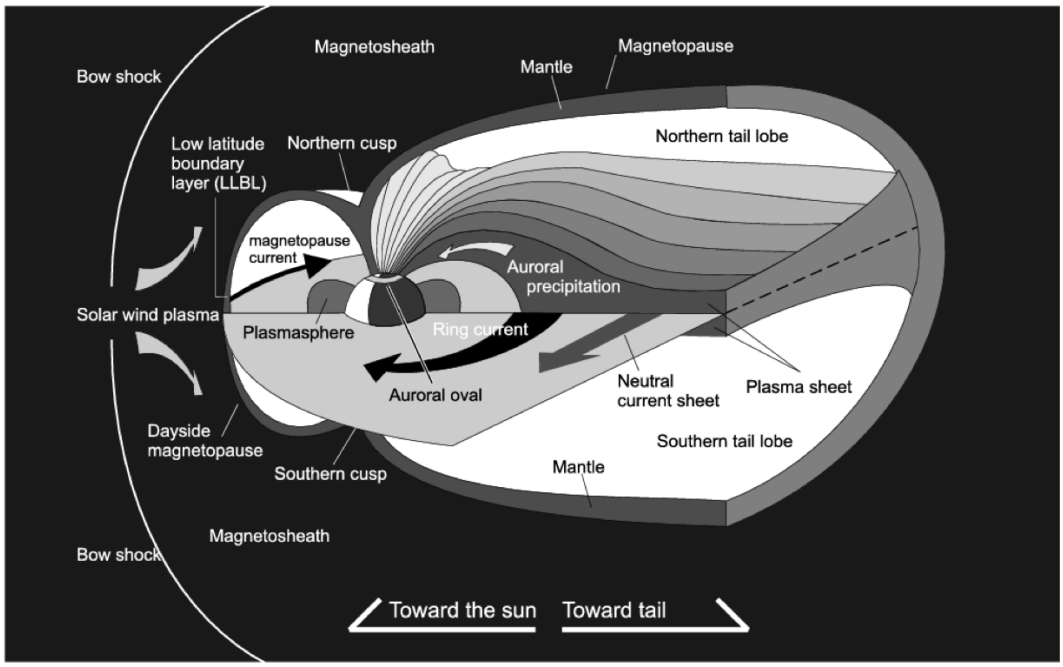

Figure 1.1: Schematic diagram of the large-scale structure of the Earth's magnetosphere.

1.1.2 Ionosphere

The Earth's upper atmosphere is partially ionized by extreme ultraviolet (EUV) radiation from the Sun; this region is called the ionosphere. The ionosphere is located at an altitude

of 60 to 1000 km and can be broadly classified into three main regions, namely, the D region (60–90 km), E region (90–150 km), and F region (above 150 km); this categorization depends on the altitude profiles of the electron density and the types of dominant ions. Figure 1.2 shows the altitude profiles of the density of the main constituents of the ionosphere. The type of dominant ion depends primarily on the altitude; in the E and F regions, molecular ions (NO^+, O_2^+) and atomic oxygen ions are dominant, respectively.

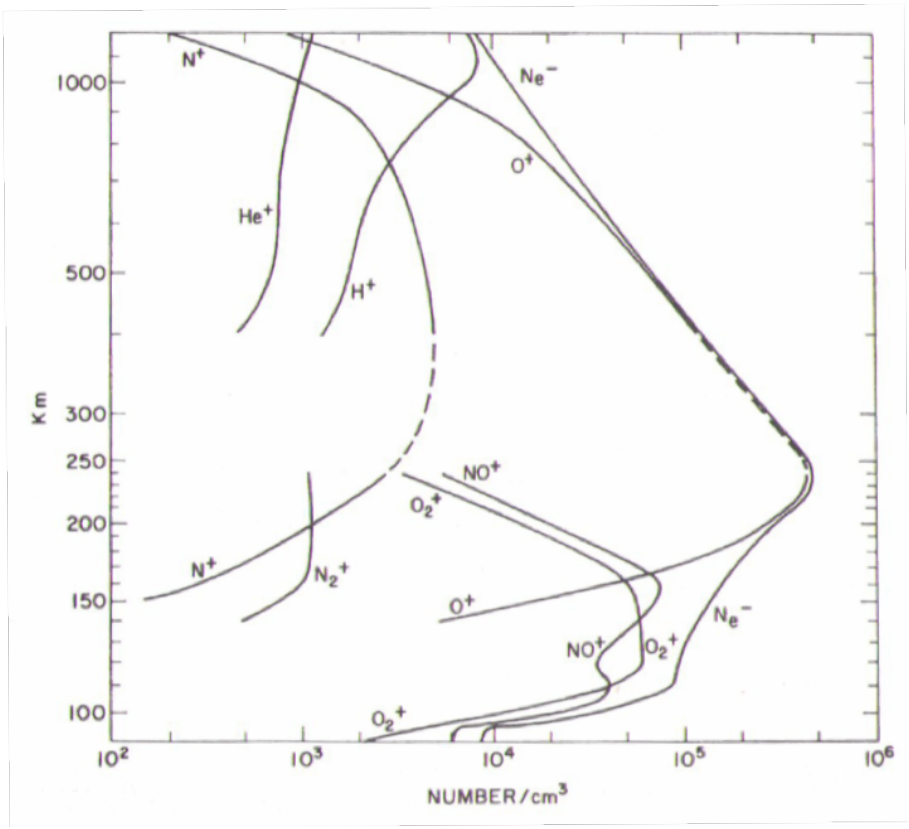

Figure 1.2: Altitude profiles of the main constituents of the ionosphere. This figure is from *Johnson* (1966).

In addition to the ionization caused by solar EUV radiation, collisional ionization also occurs when magnetospheric particles are precipitated into Earth's ionosphere along the magnetic field lines. At higher latitudes, where the magnetic latitude exceeds 60°, the Earth's ionosphere and magnetosphere are coupled via magnetic field lines. Figure 1.3 shows the altitude profiles of the ionization rates for precipitating electrons with various energies. The vertical and horizontal axes indicate the altitude and ionization rate, respectively. Higher-energy electrons can penetrate to lower altitudes and also cause collisional ionization at those altitudes. Further, an aurora is generated in a ring-like

region that surrounds the magnetic pole due to the precipitation of particles (mainly electrons) originating from the plasma sheet in the magnetosphere. These collisional ionizations caused by particle precipitation from the magnetosphere occur mainly in the E region at altitudes of approximately 100 km.

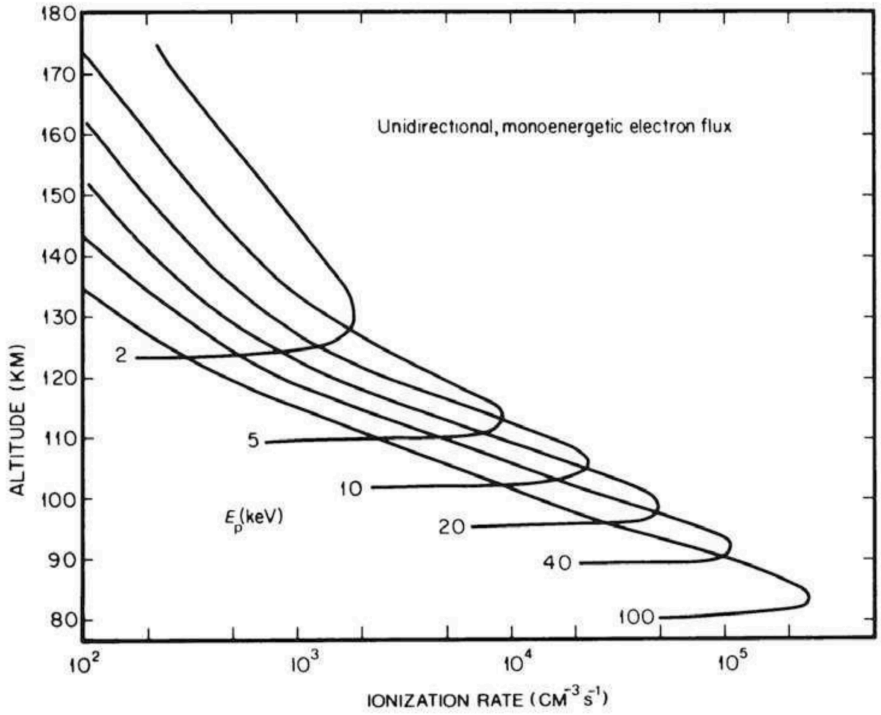

Figure 1.3: Altitude profiles of rates of collisional ionization by precipitating electrons from the magnetosphere. This figure is from *Rees* (1989).

1.1.3 Substorm

Aurora-related phenomena occur on a scale of thousands of kilometers and follow a characteristic cycle on a time scale of 1–2 h. The typical variability of this auroral activity is called the auroral substorm. The substorm was first proposed by *Akasofu* (1964), and Figure 1.4 shows a schematic diagram of the evolution of an aurora in the auroral substorm. At time $T = 0$, the nightly auroral band (A) expands toward the equator and increases in brightness (initial brightening) (B). Next, the auroral activity increases, and many auroral arcs appear (auroral breakup), which expand in the poleward and longitudinal directions (C). After expanding, they form a central bulge, a structure called an auroral bulge (D). On the night side, a patchy PsA spreads to the morning side. Subsequently, the auroral activity subsides, and the region returns to a quiet state over the next few hours (E, F).

In addition, the magnetosphere also changes significantly during the auroral substorm cycle; these changes are referred to as the magnetospheric substorm. When the interplanetary magnetic field (IMF), which is the magnetic field embedded in the solar wind, has a southward component, magnetic reconnection occurs at the dayside magnetopause. This reconnection allows the IMF to merge with the Earth's magnetosphere. Consequently, the energy of the solar wind is stored in the magnetotail and compresses the central part of the magnetotail from above and below, resulting in thinning of the plasma sheet (growth phase). When the plasma sheet is sufficiently thin, magnetic reconnection again occurs rapidly in the center of the magnetotail plasma sheet at a distance of 20–30 R_E, the so-called near-Earth neutral line, and the plasma is injected in the direction toward the Earth and the magnetotail (expansion phase). Accompanying this Earthward plasma injection in the magnetosphere, in the ionosphere, the aurora becomes brighter on the nightside and spreads rapidly. Subsequently, when the IMF turns northward, the magnetosphere returns to the quiet state (recovery phase).

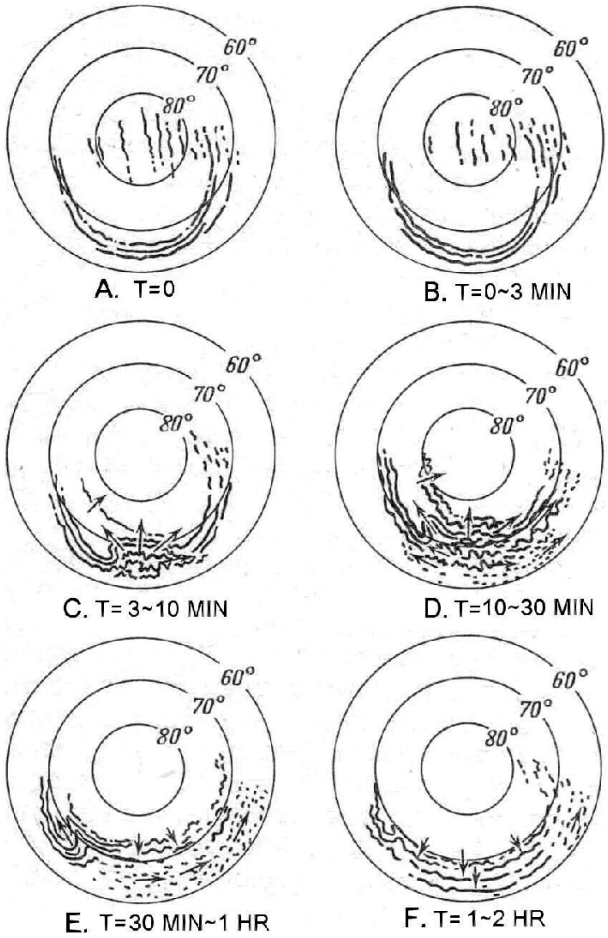

Figure 1.4: Schematic diagram of auroral development during auroral substorm. This figure is from *Akasofu* (1964).

1.2 Particle motion in the magnetosphere

The equation of motion for a charged particle moving in a magnetic field $\boldsymbol{B}$ and electric field $\boldsymbol{E}$ is expressed as follows:

$$m\frac{d\boldsymbol{v}}{dt} = q(\boldsymbol{E} + \boldsymbol{v} \times \boldsymbol{B}) + \boldsymbol{F} \tag{1.4}$$

where m, q, and $\boldsymbol{v}$ are the mass, charge, and velocity of the particle, respectively, and $\boldsymbol{F}$ is any arbitrary force (other than the Coulomb and Lorentz forces). According to this equation of motion, the particle has three main periodic motions: gyro (cyclotron) motion, bounce motion, and drift motion. In this section, we will focus mainly on bounce motion and discuss it in detail.

1.2.1 Magnetic mirror

As mentioned in the previous section, the Earth's magnetic field can be approximated by a dipole field. Substituting the magnetic latitude $\lambda = 0°$ into equation(1.1) yields the magnetic field in the equatorial plane:

$$B_{eq} = \frac{B_E}{L^3} \tag{1.5}$$

The magnetic moment μ of a particle' s motion along this inhomogeneous magnetic field is written as follows:

$$\mu = \frac{mv_{\|}^2}{2B} = \frac{mv^2 \sin^2 \alpha}{2B} = \text{Const.} \tag{1.6}$$

where m is the mass of the particle, v is the velocity of the particle ($v_{||}$ is its parallel component), B is the intensity of the magnetic field, and α is the pitch angle. The pitch angle is the angle between the magnetic field lines and the parallel component of the particle's velocity and is given by the following equation:

$$\alpha = \tan^{-1}(\frac{v_\perp}{v_\|}) \tag{1.7}$$

where $v_\perp$ and $v_\|$ are the velocity components perpendicular and parallel to the magnetic field lines of the particles, respectively. Because the magnetic moment is a constant, $v_\perp$ decreases as the magnetic field increases to cancel it out, for example, when the particle moves along a field line to a region with a stronger magnetic field. Now consider the law of conservation of kinetic energy, which is expressed as follows:

$$\frac{1}{2}m(v_\|^2 + v_\perp^2) = \text{Const.} \tag{1.8}$$

The kinetic energy is also a constant, like the magnetic moment μ; thus, when $v_\perp$ increases, $v_\|$ decreases, resulting in an increase in the pitch angle. When the pitch angle reaches 90° (at the mirror point), all the velocity components of the particle are perpendicular to the magnetic field lines, and the particle cannot precipitate any farther along the magnetic field lines. Instead, the particle is pushed back by the parallel component of the gradient $\boldsymbol{B}$, which is the so-called mirror force:

$$F = -\mu \frac{\partial \boldsymbol{B}}{\partial \boldsymbol{z}} = -\mu \nabla_\| \boldsymbol{B} \tag{1.9}$$

where $\boldsymbol{B}$ is the magnetic field, and $\boldsymbol{z}$ is the direction along the magnetic field lines. The particles are subjected to a force in the opposite direction when they move toward a stronger magnetic field.

In the geometry of an inhomogeneous magnetic field, such as the Earth's magnetic field, where the magnetic field is minimized in the equatorial plane, particles are trapped within the magnetic field as they move back and forth between the two mirror points (i.e., in the northern and southern hemispheres), which is called the magnetic mirror effect.

1.2.2 Equatorial pitch angle

As mentioned in the previous section, trapped particles move back and forth between the mirror points in the northern and southern hemispheres. Now, the position of the mirror point of a particle (e.g., the magnetic latitude or distance from the ionosphere) is closely related to the so-called equatorial pitch angle, which is given by the following equation:

$$\sin^2 \alpha_{eq} = \frac{B_{eq}}{B_m} = \frac{\cos^6 \lambda_m}{(1 + 3\sin^2 \lambda_m)^{\frac{1}{2}}} \tag{1.10}$$

where α_{eq} is the equatorial pitch angle, B_{eq} is the intensity of the magnetic field at the equatorial plane, B_m is that at the mirror point of the particular particle, and λ is the magnetic latitude of the mirror point. This equation shows that the equatorial pitch angle does not depend on the L value but depends only on the magnetic latitude of the mirror point. Thus, the magnetic latitude of the particle's mirror point is determined only by the equatorial pitch angle. Therefore, if the equatorial pitch angle α_{eq} is sufficiently small, the particle has a large parallel component of the velocity along the magnetic field lines and can penetrate into a region of higher magnetic latitude.

1.2.3 Loss cone

A particle with a sufficiently high latitude at the mirror point can collide with molecules and atoms in the Earth's atmosphere instead of making a bouncing motion. For simplicity, assuming that the mirror point is the Earth's surface, the loss cone, that is, the equatorial pitch angle at which a particle can precipitate into the Earth's atmosphere, is derived as follows:

$$\sin^2 \alpha_l = \frac{B_{eq}}{B_E} = \frac{\cos^6 \lambda_E}{(1 + 3\sin^2 \lambda_E)^{\frac{1}{2}}} \tag{1.11}$$

where α is the angle of the loss cone, B_E is the intensity of the magnetic field at the Earth's surface, and λ_E is the magnetic latitude of the Earth's surface, respectively. The width of the loss cone does not depend on the charge, mass, or energy of the particles,

but only on the radius of the magnetic field lines. The width of the loss cone is generally quite small, for example, less than a few degrees in the auroral region.

1.3 Aurora

As described above, the Earth's magnetosphere and ionosphere are coupled via magnetic field lines, and electrons with energies ranging from a few hundred eV to a few hundred keV tend to precipitate from the magnetosphere (primarily from the plasma sheet) along the magnetic field lines. The precipitating electrons collide with atomic and molecular ions in the ionosphere and transfer their energy to the Earth's ionospheric atoms and molecules; subsequently, they attain their excited states. When they return to their more stable states, they release photons in the form of auroral emissions.

1.3.1 Auroral emission

Auroral emission is characterized by several main emission lines of nitrogen molecules, oxygen molecules, oxygen atoms, or their ions, which form the majority of the Earth's atmosphere (and ionosphere). Here, we introduce three typical emission lines in auroral emission.

- **427.8 nm emission**

  Emission at 427.8 nm occurs when the excited state of the first negative band, $N_2^+(B^2\Sigma_u^+)$, transitions to the ground state, $N_2^+(X^2\Sigma_g^+)$. The excited state of $N_2^+(B^2\Sigma_u^+)$ is produced by collisional ionization with precipitating electrons, which can be expressed as

  $$N_2 + e \rightarrow N_2^+(B^2\Sigma_u^+) + e + e \tag{1.12}$$

  The emission at 427.8 nm is due to a permitted transition and is immediately observed after electron precipitation. Its lifetime is $\sim 10^{-8}$ s (*Nozawa et al.*, 2018), so it is useful for observing auroras with fast modulations, such as the PsA described below.

- **557.7 nm emission**

  The emission at 557.7 nm is the brightest auroral emission and is produced by the transition from the excited state of $O(^1S)$ to the $O(^1D)$ state. Although the excitation process of $O(^1S)$ is still unclear, there are three candidate mechanisms:

1. Direct collision of secondary electrons due to precipitating electrons

$$O(^3P) + e \rightarrow O(^1S) + e \tag{1.13}$$

2. Dissociative recombination with O_2^+ ions

$$O_2^+ + e \rightarrow O(^1S) + O(^1S) + e \tag{1.14}$$

3. Energy transfer from the excited N_2 molecule

$$N_2(A^2\Sigma_+^2) + O \rightarrow O(^1S) + N_2 \tag{1.15}$$

The emission at 557.7 nm is associated with a forbidden transition, unlike that at 427.8 nm, and the corresponding lifetime is approximately 0.7 s (*Brreke and Henriksen*, 1972). In the forbidden transition, the excited states are likely to lose their energy in collisions with other particles rather than by optical emission. Therefore, at an altitude of ∼100 km, the excited state of O(^{1}S) loses its energy not by optical emission but through collisions that occur because of the dense neutral atmosphere at that altitude. In Chapter 3, we use the lifetime of this emission at 557.7 nm to estimate the emission altitude of the PsA.

- **630.0 nm emission**

  The third emission line is observed at 630.0 nm and is caused by the transition from O(^{1}D) to the ground state O(^{3}P). The O(^{1}D) state is produced not only by the transition from the O(^{1}S) state, but also by collisions with precipitating electrons, which are represented by the following equation:

$$O(^3P) + e \rightarrow O(^1D) + e \tag{1.16}$$

  The emission at 630.0 nm is also due to a forbidden transition, like that at 557.7 nm, which has a lifetime of approximately 110 s (*Rees and Roble*, 1975). At altitudes below ∼250 km, strong emission does not occur at 630.0 nm owing to collisional de-excitation; thus, the 630.0 nm emission layer is typically located between 250 and 500 km.

1.3.2 Types of aurora

As described above, auroras result from the precipitation of energetic electrons from the magnetosphere, which is caused by several processes. Auroras are classified into several

categories according to these processes. Figure 1.5 shows an auroral image captured from the International Space Station. The green curtain-like aurora in the upper part of the image is the discrete aurora, and the irregularly shaped aurora in the lower part of the image is the diffuse aurora. These two types of aurora are described briefly below.

Figure 1.5: Auroral image taken by the crew of the International Space Station. This image was obtained from the Earth Science and Remote Sensing Unit, NASA Johnson Space Center, The Gateway to Astronaut Photography of Earth (eol.jsc.nasa.gov).

- **Discrete aurora**

  Discrete auroras are curtain-shaped, as shown in the upper part of Figure 1.5. Auroral arcs are the most well-known form of discrete aurora. An auroral arc is a structure that is elongated in the east-west direction; it is a luminous layer several kilometers in thickness. The energy of the electrons associated with the auroral arc has a specific peak ranging from a few keVs to a dozen or so keV. This peak energy increases and decreases with latitude, showing an inverted-V structure (*Frank and Ackerson*, 1971). Satellite observations have also shown a potential difference of several keVs at the onset of auroral arcs (*Mozer et al.*, 1977); electrons are accelerated by the upward electric field along these magnetic field lines to form auroral arcs (*Torbert and Mozer*, 1978; *Lin and Hoffman*, 1982).

- **Diffuse aurora**

  A diffuse aurora is caused by the precipitation of electrons from the central plasma sheet or inner magnetosphere. PsA, which is the main subject of this thesis, is a

type of diffuse aurora. Wave-particle interactions due to cyclotron resonance have long been proposed as a mechanism for the formation of diffuse aurora (*Kennel and Petschek*, 1966). Recent satellite observations have revealed that chorus waves and electrostatic electron cyclotron harmonic (ECH) waves play an important role in the pitch-angle scattering of electrons, which contributes to the formation of diffuse aurora (*Thorne et al.*, 2010). In addition, unlike the mono-energetic discrete auroral arcs, the electrons contributing to the diffuse auroral emission are distributed over a wide energy range (a few keVs to a few tens of keVs). It has also been reported that the ECH waves and upper band chorus contribute to the pitch-angle scattering of low-energy electrons, and the lower band chorus causes the pitch-angle scattering of high-energy electrons (e.g., *Ni et al.*, 2008). However, the wave-particle interaction process is still unclear and needs to be elucidated in detail; thus, the diffuse auroras associated with wave-particle interactions are regarded as an active area of research in space science.

1.4 Pulsating aurora

PsA is a type of diffuse aurora that exhibits ON and OFF phases within a period of few seconds to a few tens of seconds. Most diffuse auroras exhibit such quasi-periodic variations in their luminosity; thus, PsA is a universal auroral phenomenon that appears mainly on the morning side.

1.4.1 Morphology

PsA is generally observed between the midnight and dawn sectors (*Royrvik and Davis*, 1977). *Jones et al.* (2011) derived the occurrence distribution of PsA using two all-sky imagers at Gillam (66.1°N, 333.9°E) and Fort Smith (67.3°N, 306.7°E) in North America. Figure 1.6 shows the occurrence distribution of PsA as a function of MLT. The dotted, dashed, and dot-dashed lines show the number of events observed, number of PsA events, and occurrence rate of PsA among all the observations, respectively. The occurrence rate increases dramatically after 00 MLT and remains high (nearly 60%) until dawn. They also investigated the duration of PsA and found a typical duration of approximately 1.5 h. Furthermore, dayside PsA was also reported at high latitudes in previous studies (*Han*

et al., 2015; *Motoba et al.*, 2017).

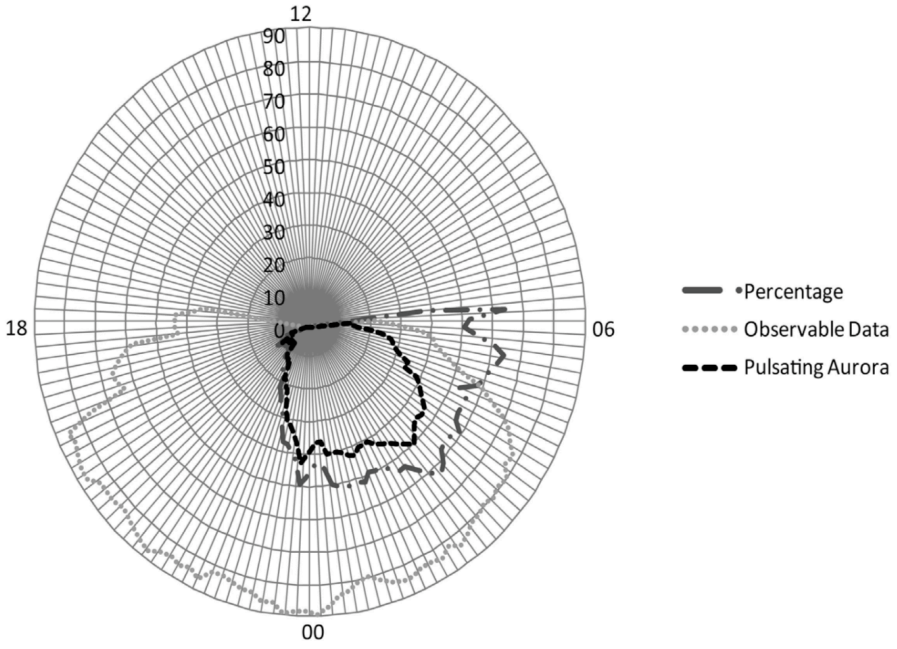

Figure 1.6: Occurrence distribution of PsA versus MLT. The dotted line indicates the number of observed events. The dashed line indicates the number of observed PsA events at each MLT. The dot-dashed line indicates the occurrence rate of PsA events among all observations. This figure is from *Jones et al.* (2011).

The spatial structures of PsA can be broadly divided into two types (*Royrvik and Davis*, 1977; *Yamamoto*, 1988; *Sato et al.*, 2002):

1. Arc structures, which generally extend in the east-west direction

2. Patch structures, which appear as clusters of patches having irregular shapes

PsA is known to show characteristic propagation modes during the ON phase, which are poleward, equatorward, and longitudinal propagation (*Oguti*, 1975). In addition to the rapid propagation during the ON phase, patches of PsA tend to move with the speed of ionospheric convection. It was shown that the direction of propagation changes around midnight (*Nakamura and Oguti*, 1987). The direction before midnight is duskward, whereas that after midnight is dawnward. As mentioned above, the speed of propagation reportedly follows the speed of the $\boldsymbol{E} \times \boldsymbol{B}$ drift (*Yang et al.*, 2015).

1.4.2 Emission and ionization altitude

The emission altitude of PsA has been intensively studied since the 1970s owing to its close relationship with the energy of the precipitating electrons. *Brown et al.* (1976) estimated the emission altitude of PsA by applying triangulation to two all-sky TV imagers at College, Alaska. They found that the emission altitude of PsA ranges between 82 and 115 km. A recent similar analysis by *Partamies et al.* (2017) revealed that the emission altitude of PsA tended to be lower on the morning side. However, these results obtained via optical observations are not statistically significant because of the limited data available. In addition to these optical observations, incoherent scatter (IS) radar observations have also been conducted to investigate the variation of electron density during PsA. *Jones et al.* (2009) estimated the energy of PsA electrons and the thickness of the emission layer using the Poker Flat Incoherent Scatter Radar (PFISR). They found that the electrons responsible for PsA have energies of 6–8 keV and that the emission layer is 15–25 km thick. More recently, *Hosokawa and Ogawa* (2015) verified an MLT variation in the ionization height from the electron density profile during PsA using the European Incoherent SCATter (EISCAT) radar. Figure 1.7 shows the distribution of the ionization height as a function of MLT (*Hosokawa and Ogawa*, 2015). The top and bottom panels show the MLT distributions of all the PsA events and the occurrence distribution of h_mE versus MLT, respectively, where h_mE is the peak height of the electron density in the E region and is an indicator of the altitude at which the PsA causes ionization. In the bottom panel, the peak is almost constant from 00 to 06 MLT. However, after 06 MLT, the peak becomes lower below 100 km, and they concluded that the energy of the precipitating PsA electrons is higher on the morning side. The typical energy of PsA electrons is a few keVs to tens of keVs (*Sandahl et al.*, 1980). However, several studies have reported that more energetic electrons are precipitated during PsA (*Miyoshi et al.*, 2015b). These very energetic electrons can precipitate into the mesosphere, which is located at an altitude below 90 km. *Turunen et al.* (2016) detected ionization at an altitude of 68 km using the EISCAT VHF radar and showed that this precipitation of energetic electrons results in an increase in NO_x and HO_x and eventually a decrease in O_3.

As descried above, the variations in the electron density and ionization altitude during PsA have been investigated in detail using IS radars. However, the statistical properties of the emission altitude of PsA have not been investigated. Therefore, in Chapter 3, we

derive the statistical characteristics of the emission altitude of PsA from the lifetime of $O(^1S)$.

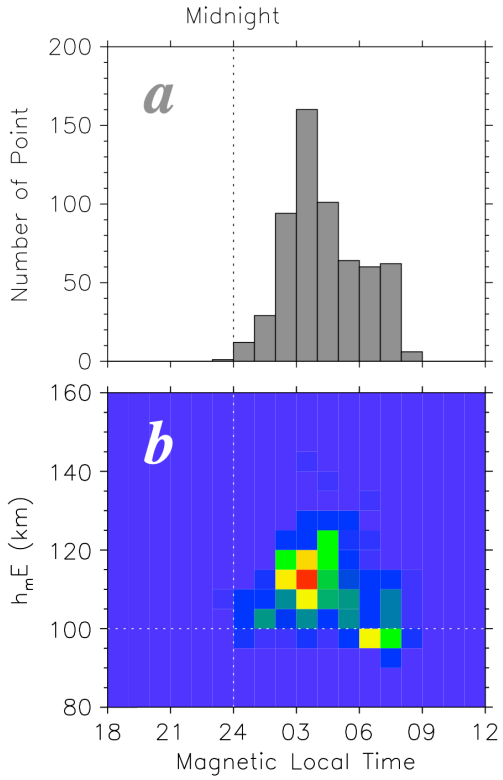

Figure 1.7: MLT distribution of observed PsA events (upper panel) and occurrence distribution of the E region peak height (h_mE) (lower panel). The occurrence rate is self-normalized in the lower panel. This figure is from *Hosokawa and Ogawa* (2015).

1.4.3 Temporal characteristics

The most significant characteristic of PsA is hierarchical temporal variations, in which more rapid subsecond variations (called internal modulations) are superimposed on the so-called main pulsation, whose period ranges from a few seconds to a few tens of seconds (*Lessard*, 2012, and references therein). These hierarchical temporal variations in PsA have been investigated in previous studies through ground-based observations with high temporal resolution such as those using a narrow-field TV imager. *Royrvik and Davis* (1977) observed a 3 Hz modulation (they described the internal modulation as a 3 Hz modulation) using a narrow-field TV imager at College, Alaska. Figure 1.8 shows a typical example of the hierarchical temporal variations in PsA, as observed in the study of *Royrvik and Davis* (1977). The top panel shows an image captured by the narrow-field

TV imager, and the bottom panel shows the optical time series inside the white box in the top panel. Several increases in luminosity appear in the bottom panel; they correspond to the main pulsation. Moreover, a fine-scale (i.e., faster) variation is embedded in the ON phase of the main pulsation, which shows the signature of the 3 Hz modulation (i.e., the internal modulation). These ground-based observations in the 1960s to 1970s revealed the existence of hierarchical temporal variations of PsA. However, the observations are limited as they were obtained at a single observation station.

To reveal the large-scale characteristics of PsA, Japan and Canada conducted a joint observation campaign in January and February 1980. This campaign led to successful ground-based optical observations at several stations, along with rocket and satellite observations. The details were reported by *McEwen and Duncan* (1980). These observations produced a number of significant results; here, we introduce the principal results regarding the hierarchical temporal variations of PsA. All-sky TV imagers were installed at four stations in Alaska, and the field of view (FOV) of these four imagers covered a latitude range of 61.3°N to 67.8°N. *Duncan et al.* (1981) verified the latitudinal dependence of the period of the main pulsation using all-sky TV imagers installed at Saskatoon, Rabbit Lake, Southend, and La Ronge. Figure 1.9 shows the distribution of the period of the main pulsation for each observation point derived by *Duncan et al.* (1981). Note that periodicities longer than 18 s are shaded. Figure 1.9 clearly shows that the period of the main pulsation becomes longer with increasing latitude.

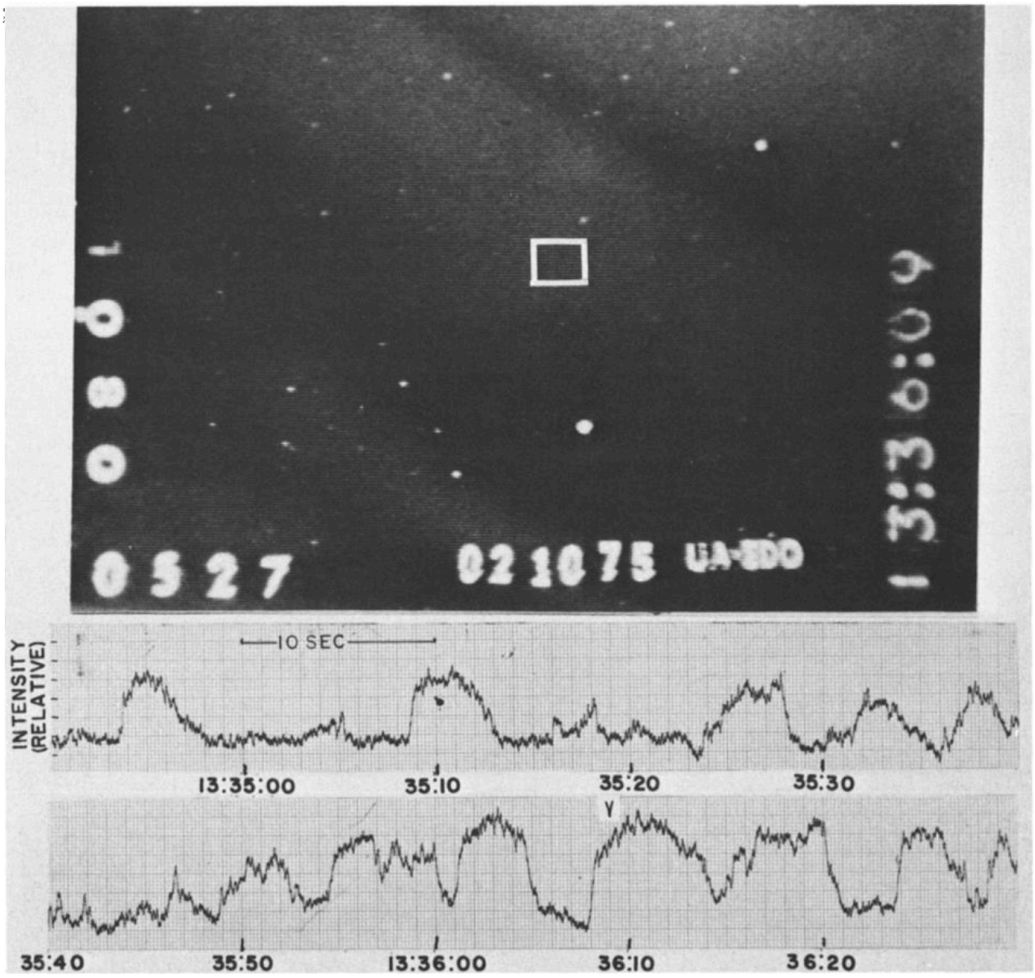

Figure 1.8: Typical example of the 3 Hz modulation obtained from a narrow-field TV imager. Image taken by the narrow-field TV imager at 13:36:09 UT on February 10, 1975 (upper panel). Optical time series sampled in the white box in the top panel from 13:34:50 to 13:36:30 UT on the same day (lower panel). These figures are from *Royrvik and Davis* (1977).

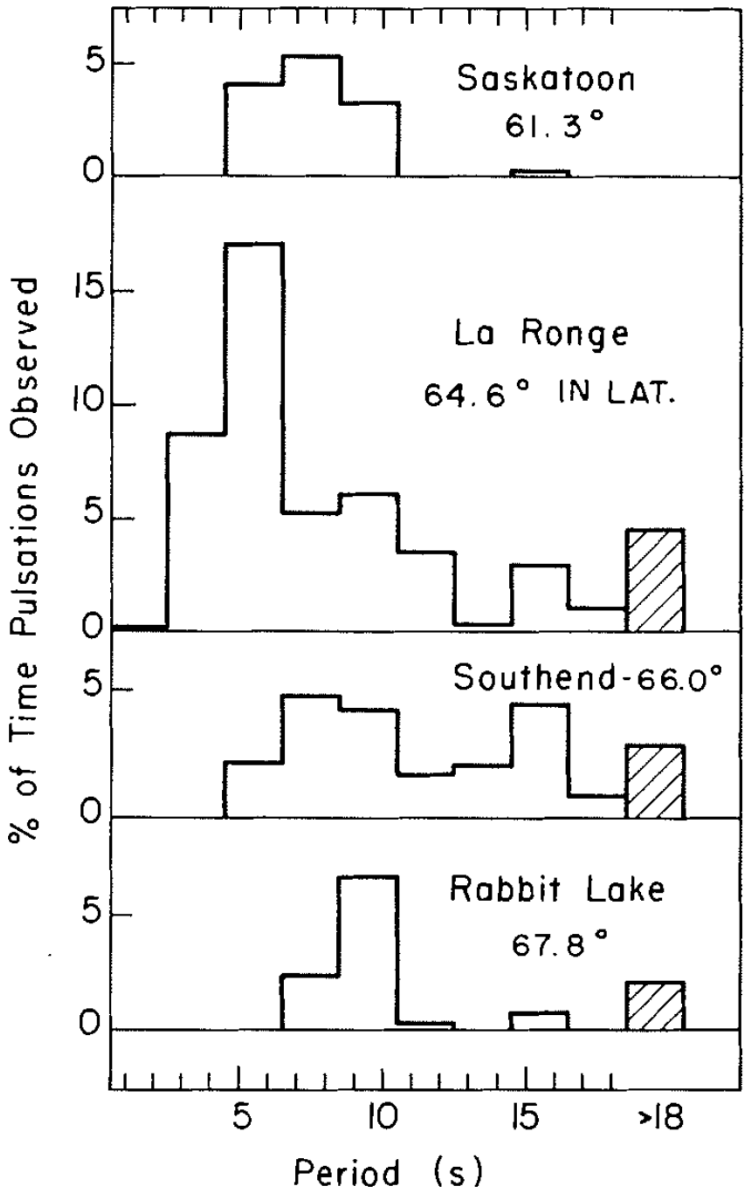

Figure 1.9: Latitudinal dependence of the main pulsation of PsA. This figure is from *Duncan et al.* (1981).

Yamamoto (1988) statistically investigated the period of the main pulsation using the all-sky TV imager installed at La Ronge. Figure 1.10 shows the period distribution of the main pulsation derived by *Yamamoto* (1988). The solid, shaded, and dashed lines indicate the duration of the ON phase, duration of the OFF phase, and period of the main pulsation, respectively. The mean duration of the ON phase is 6.2 ± 1.7 s, and that of the OFF phase is 14.5 ± 5.3 s; further, the mean period of the main pulsation is 20.7 ± 5.4 s. Note that the majority of the main pulsations are distributed from 20 to 30 s,

and there are a few main pulsations with short periods of a few seconds. However, these results are not statistically significant because a limited amount of data was used in the analyses.

In the 2010s, several groups reported that there is a one-to-one correspondence between PsA and whistler-mode chorus waves in the magnetosphere (*Nishimura et al.*, 2010; *Kasahara et al.*, 2018; *Kawamura et al.*, 2019). In addition, a number of studies have investigated the rapid variations of the internal modulation of PsA using ground-based optical instruments with high temporal resolution, such as electron-multiplying charge-coupled device (EMCCD) imagers (*Samara and Michell* 2010; *Nishiyama et al.*, 2014). *Nishiyama et al.* (2014) performed a statistical analysis of the hierarchical temporal variation of PsA on the basis of 53 events observed at Poker Flat, Alaska, between December 2011 and March 2012. They employed an EMCCD imager with a wide FOV, and their temporal resolution was 100 Hz. Figure 1.11 shows the distributions of the hierarchical temporal variations and the distributions of the periods as a function of the auroral intensity derived by *Nishiyama et al.* (2014). The top two panels show the occurrence distributions of the main pulsation and internal modulation, respectively. The frequencies of the internal modulation are distributed between 1.5 and 3.3 Hz, and a few fast modulations beyond 3 Hz were observed. They suggested that the variation of the travel time of PsA electrons from the magnetosphere to the ionosphere may smear the fine-scale (more rapid) modulations beyond 3 Hz. The periods of most of the main pulsations are distributed from 4 to 12 s, and no main pulsations were observed at periods of a few tens of seconds, as shown by *Yamamoto* (1988). The bottom two panels show scatter plots of the main pulsation and internal modulation versus auroral intensity. Although the internal modulation is correlated with the auroral intensity (correlation coefficient: 0.58), the main pulsations do not have a similar correlation. *Samara and Michell* (2010) also observed fine pulsations with frequencies ranging from 0.5 to 15 Hz using narrow-field EMCCD imagers; these modulation frequencies are consistent with the observational repetition frequency of the chorus waves (*Tracktengerts et al.*, 2014). Modulations more rapid than the internal modulation have also been reported (e.g., *Ozaki et al.*, 2018). In particular, *Kataoka et al.* (2012) used a Phantom V710 high-speed camera with a frame rate of 500 images per second and reported modulations of a few tens of Hz at the edges of a PsA patch.

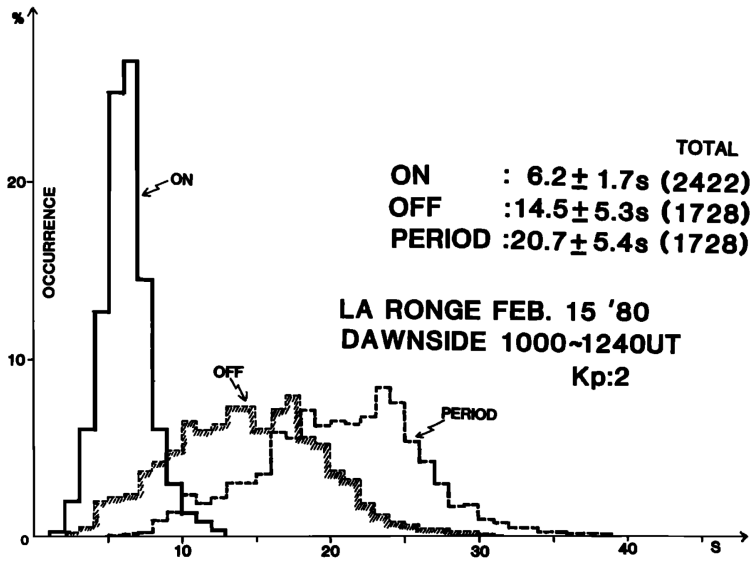

Figure 1.10: Occurrence distribution of the period of the main pulsation (dashed line) and the duration of the ON phase (solid line) and OFF phase (shaded line). This figure is from *Yamamoto* (1988).

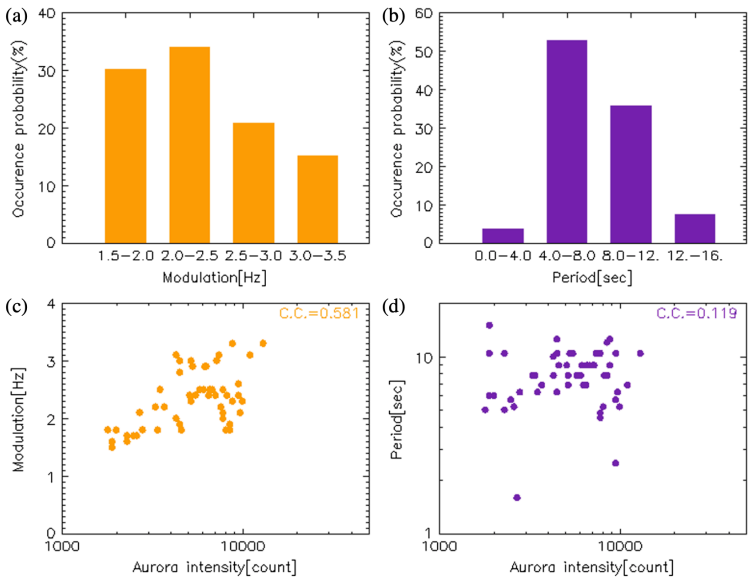

Figure 1.11: Histogram of the frequency of the internal modulation (upper left panel) and the period of the main pulsation (upper right panel). Scatter plots of the frequency of the internal modulation (lower left panel) and the period of the main pulsation (lower right panel) as a function of auroral intensity. This figure is from *Nishiyama et al.* (2014).

1.4.4 Generation mechanism

It has been widely accepted that PsA electrons are scattered owing to cyclotron resonance with plasma waves near the magnetic equator (*Johnstone*, 1983; *Davidson*, 1990). In particular, *Thorne et al.* (2010) showed that chorus waves are the most efficient agent to precipitate electrons with energies ranging from a few keVs to a few tens of keVs and thus contribute to PsA emission. Chorus waves are a type of whistler-mode wave with quasi-periodic emission and appear as clusters (or bundles) of individual chorus elements. Their frequency depends on the electron cyclotron frequency (f_{ce}), and chorus waves are known to occur at frequencies of 0.1 to 0.8 f_{ce} (*Tsurutani and Smith*, 1977; *Santolik et al.*, 2003). In particular, chorus waves are commonly divided into two distinct frequency ranges, namely, 1) the upper band chorus (UBC), with a frequency range of up to 0.5 f_{ce}, and 2) the lower band chorus (LBC), with frequencies below 0.5 f_{ce}. The LBC is considered to be primarily responsible for the precipitation of PsA electrons (*Miyoshi et al.*, 2015a). Figure 1.12 is a frequency–time (f–t) diagram of the electric field wave data from the Time History of Events and Macroscale Interactions during Substorm (THEMIS) satellite (*Li et al.*, 2012). The horizontal white line in Figure 1.12 indicates a frequency of 0.5 f_{ce}. As shown in the bottom panel, all chorus waves appear in the frequency band below 0.5 f_{ce}, which is 700–1500 Hz. This collective (and repetitive) occurrence of chorus waves is called bursts of chorus or chorus bursts. The upper panel is a magnified view of the period indicated by the red arrow in the bottom panel. Fine-scale structures (so-called chorus elements) are embedded in a single burst of chorus. In this way, like a PsA, chorus waves also exhibit hierarchical temporal variations.

Nishimura et al. (2010) recently reported a one-to-one correspondence between the optical time series of a PsA and the amplitude variation of the chorus wave. They conducted simultaneous observations using a ground-based all-sky imager and the THEMIS satellite to investigate the correlation between the auroral intensity and the chorus wave amplitude. The upper left panel in Figure 1.13 shows a schematic diagram of their simultaneous observations. The footprints of the THEMIS satellite are located within the FOV of the all-sky imager, and the THEMIS satellite obtained the f–t diagrams of the electric and magnetic field wave data near the magnetic equator, which represent the source region of the PsA (upper right panel in Figure 1.13). Intense LBC appears at frequencies below 0.5 f_{ce} in both f–t diagrams. A PsA was also observed in the ionosphere at the

same time. The lower left panel in Figure 1.12 shows four snapshots taken by the all-sky imager, where the purple square indicates the footprint of the THEMIS satellite, and the red arrow shows the region of the PsA patch. The lower right panel in Figure 1.13 shows the correspondence between the average amplitude variation of the chorus wave (blue line), which was obtained by sandwiching from 0.05 to 0.5 f_{ce}, and the optical time series of the PsA (red line) at the highest correlation pixel of the all-sky imager. In the lower right panel of Figure 1.13, higher wave amplitude and auroral intensity correspond to the bursts of chorus and main pulsation, respectively. Further, the correlation coefficient between them is 0.88, which indicates that there is a one-to-one correspondence between the chorus wave and PsA.

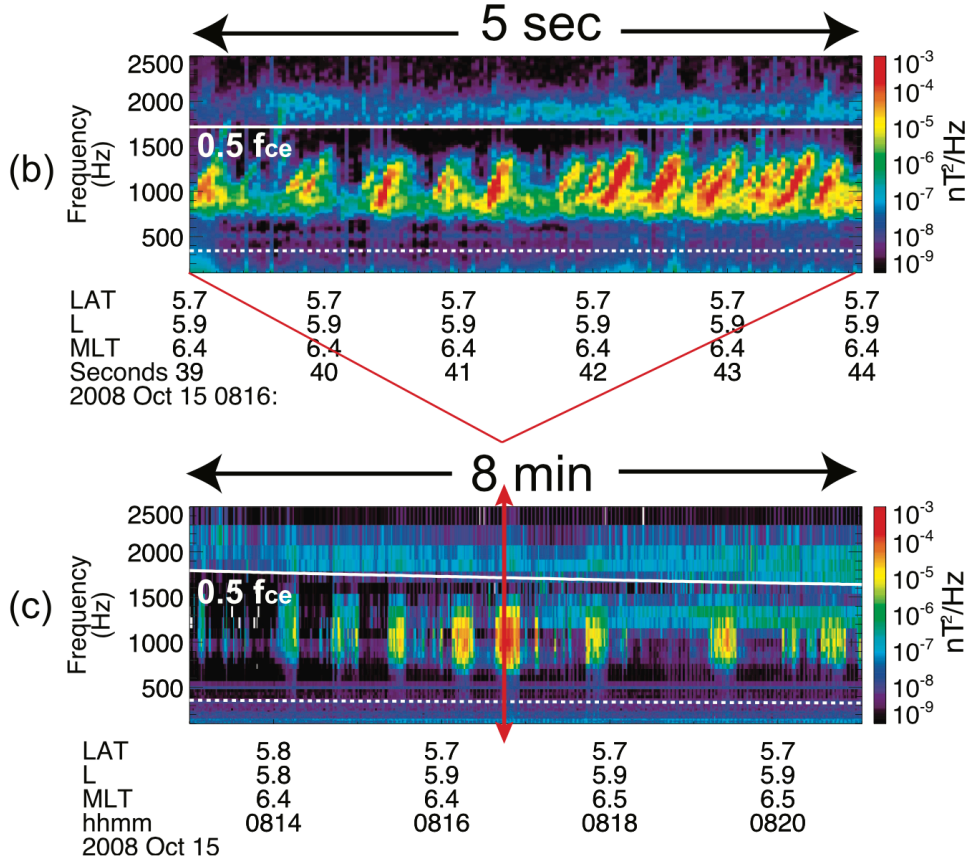

Figure 1.12: Frequency–time diagram of magnetic field observed by THEMIS satellite in 8 min interval (08:13–08:21 UT, October 15, 2008) (lower panel). Magnified view of 5 s indicated by red arrow in bottom panel (upper panel). This figure is from *Li et al.* (2012).

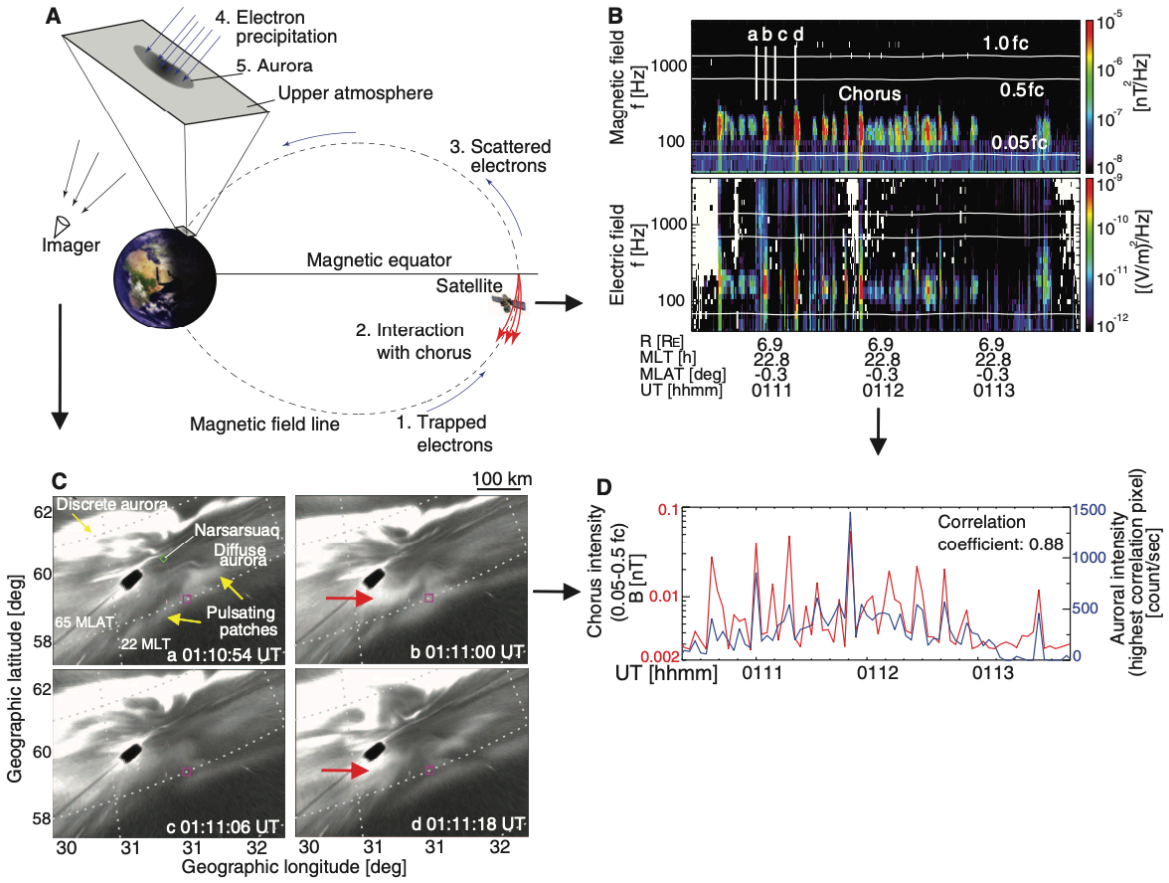

Figure 1.13: Schematic diagram of simultaneous observations conducted by *Nishimura et al.* (2010) (upper left panel). THEMIS satellite observations of bursts of chorus showing the frequency–time diagram of the electric field. White horizontal line indicates the local electron cyclotron frequency (f_{ce}), which is calculated from the measured magnetic field (upper right panel). Snapshots of the all-sky imager, which is projected to the geographic coordinates at 110 km. The red arrow indicates the PsA patch that shows the highest correlation with the chorus wave (lower left panel). Direct comparison between the amplitude variation of the chorus wave integrated over a frequency range of 0.05 to 0.5 f_{ce} and the optical time series of PsA at the highest correlation pixel (lower right panel). This figure is from *Nishimura et al.* (2010).

More recently, *Hosokawa et al.* (2020a) demonstrated an excellent correlation between a PsA and chorus waves, including a fine-scale structure (i.e., the internal modulation and chorus elements), by performing simultaneous observations using ground-based high-speed EMCCD all-sky imagers and the ARASE satellite. In these observations, two internal

modulations were obtained, one in Scandinavia and the other in Alaska. Figure 1.14 directly compares the internal modulation and the chorus elements. The top two panels show the keogram, and the bottom two panels represent the f–t diagram. In the left panels, which represent observations in Scandinavia, there is no clear signature of either the chorus elements or the internal modulation. In the right panels, which represent those in Alaska, a burst of chorus comprising discrete chorus elements is observed at the same time as fine-scale vertical stripes, which correspond to the internal modulation. From this set of observations, they concluded that the presence of chorus elements plays a significant role in controlling the hierarchical temporal variations of PsA.

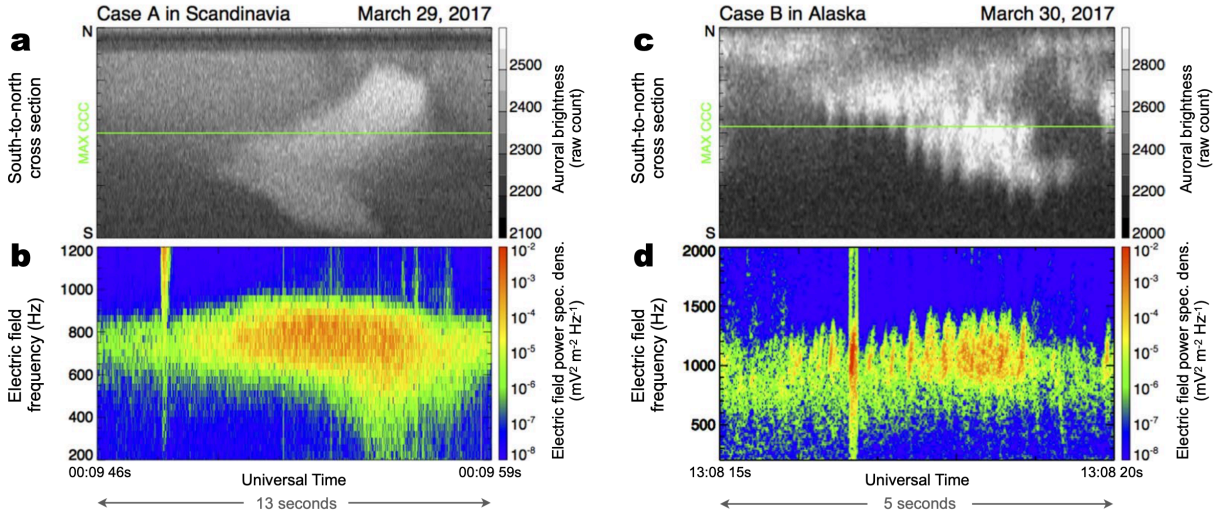

Figure 1.14: Direct comparison of the internal modulation of the PsA and the individual chorus elements. Magnified view of a single main pulsation of the PsA (upper left panel) and the corresponding bursts of chorus (lower left panel) from a simultaneous observation in Scandinavia. Magnified view of a single main pulsation (upper right panel) and the corresponding bursts of chorus (lower right panel) from a simultaneous observation in Alaska. This figure is from *Hosokawa et al.* (2020a).

Recent simultaneous ground-satellite observations have shown that chorus waves play a significant role in the generation of PsA. However, the factors that control the modulation of the chorus waves remain unclear, although there are several candidates. *Coroniti and Kennel* (1970) suggested that the linear growth rate of the chorus waves varies quasi-periodically because of geomagnetic pulsations. *Davidson* (1979, 1990) proposed a model based on relaxation oscillations. In this model, intense waves cause pitch-angle scattering,

which fills the loss cone with electrons. As the electrons in the loss cone precipitate into the ionosphere, the anisotropy decreases, and the process of wave growth transitions to the initial state. Then, the conditions for wave growth reappear, and the above process is repeated. They suggested that the repetition of this process causes the simultaneous appearance of chorus waves. *Demekhov and Trakhtengerts* (1994) proposed the flow cyclotron maser theory, which is based on the assumption that chorus waves are generated in a region of high plasma density in a plasma trough. This theory suggests that a flux tube with high cold plasma density acts as a duct for the chorus waves, and PsA occurs because the precipitating electrons fill the duct. Recent satellite observations have shown that chorus waves and the total electron density are strongly correlated (correlation coefficient: 0.9), indicating a one-to-one correspondence between the decrease in density and the increase in chorus wave amplitude. *Li et al.* (2011) calculated the linear growth rate of the chorus waves using the observed plasma parameters and demonstrated that the density depletion intensifies the chorus waves. They suggested that density depletion plays a significant role in the chorus wave modulation and thus may contribute to the periodicity of PsA.

1.5 Open questions and motivation of the thesis

PsA has been intensively studied since the 1960s. More recently, simultaneous ground-based and satellite observations have reported a one-to-one correspondence between PsA and chorus waves, indicating that studies of PsA are important for better understanding of chorus waves and wave–particle interactions in the magnetosphere. However, fundamental questions about the characteristics of PsA have not been answered. Although the amplitude variation of chorus waves has been shown to be fundamental to the temporal variations of PsA, it is not entirely clear how the hierarchical temporal variations, which are the most significant characteristics of PsA, are controlled. It was reported recently that the hierarchical temporal variations of PsA are due to the periodicity of the chorus wave as well as the transit time required for the PsA electrons to precipitate from the magnetosphere to the ionosphere (*Miyoshi et al.*, 2010; *Nishiyama et al.*, 2014). This transit time depends on the energy of PsA electrons, which have a wide range of energies (*Sandahl et al.*, 1980) as well as a tendency toward MLT variation (*Hosokawa and Ogawa*, 2015). Thus, there is a certain diversity in the energy of the precipitating electrons which

contribute for PsA, and this diversity may play an important role in controlling the hierarchical temporal variations of PsA. However, conventional rocket and IS radar observations are constrained by a limited observation time, and it is difficult to monitor the PsA electron energy (i.e., emission altitude) continuously. Therefore, it is necessary to clarify the statistical properties of the PsA electron energy using optical observations, which enable steady-state observation. It is also necessary to consider the mechanism controlling the hierarchical temporal variations of PsA in terms of the range of PsA electron energies. Therefore, in Chapter 3, we estimate the emission altitude of a PsA from a large amount of data using a method proposed by *Scourfield et al.* (1981) and verify the dependence of the PsA electron energy on MLT. In Chapter 4, we investigate the spatial distribution of the hierarchical temporal variations of PsA using highly sensitive EMCCD all-sky imagers installed at four stations in Scandinavia and discuss the factors, excluding chorus waves, that can control the hierarchical temporal variations by considering the range of PsA electron energy obtained in Chapter 3.

Chapter 2

Instruments

The internal modulation of PsA occurs at 3 ± 1 Hz. Thus, ground-based optical observation must have high temporal resolution to identify and investigate the characteristics of PsA. In this section, we briefly introduce the ground-based optical instruments with high temporal resolution that were used in this work. We employed a five-wavelength photometer in Tromsø, Norway (69.6°N, 19.2°E) and four EMCCD all-sky imagers installed in locations in Scandinavia, including Tromsø. The five-wavelength photometer and the EMCCD all-sky imagers have temporal resolutions of 400 and 100 Hz, respectively; both these devices can observe and determine the hierarchical temporal variations of PsA. In particular, the author was involved in the development of the EMCCD all-sky imager observation system described in Section 2.2.

2.1 Five-wavelength photometer

The five-wavelength photometer has been operative in Tromsø, Norway. A schematic diagram of the photometer is shown in Figure 2.1. The main components are the head part, four dichroic meters, five optical band-pass filters, and five photomultiplier tubes. Light incident on the head part (for example, an auroral emission) is split by the four dichroic meters and five optical band-pass filters, which allows the photometer to simultaneously observe the optical emission at five wavelengths (427.8, 557.7, 630.0, 777.4, and 844.6 nm). As this photometer simultaneously observes optical emissions at five wavelengths, it is possible to estimate the energy of precipitating electrons (*Adachi et al.*, 2017) and to derive the variation in the densities of oxygen molecules and oxygen atoms (*Scourfield et*

al. 1971) by comparing the optical time series at each wavelength.

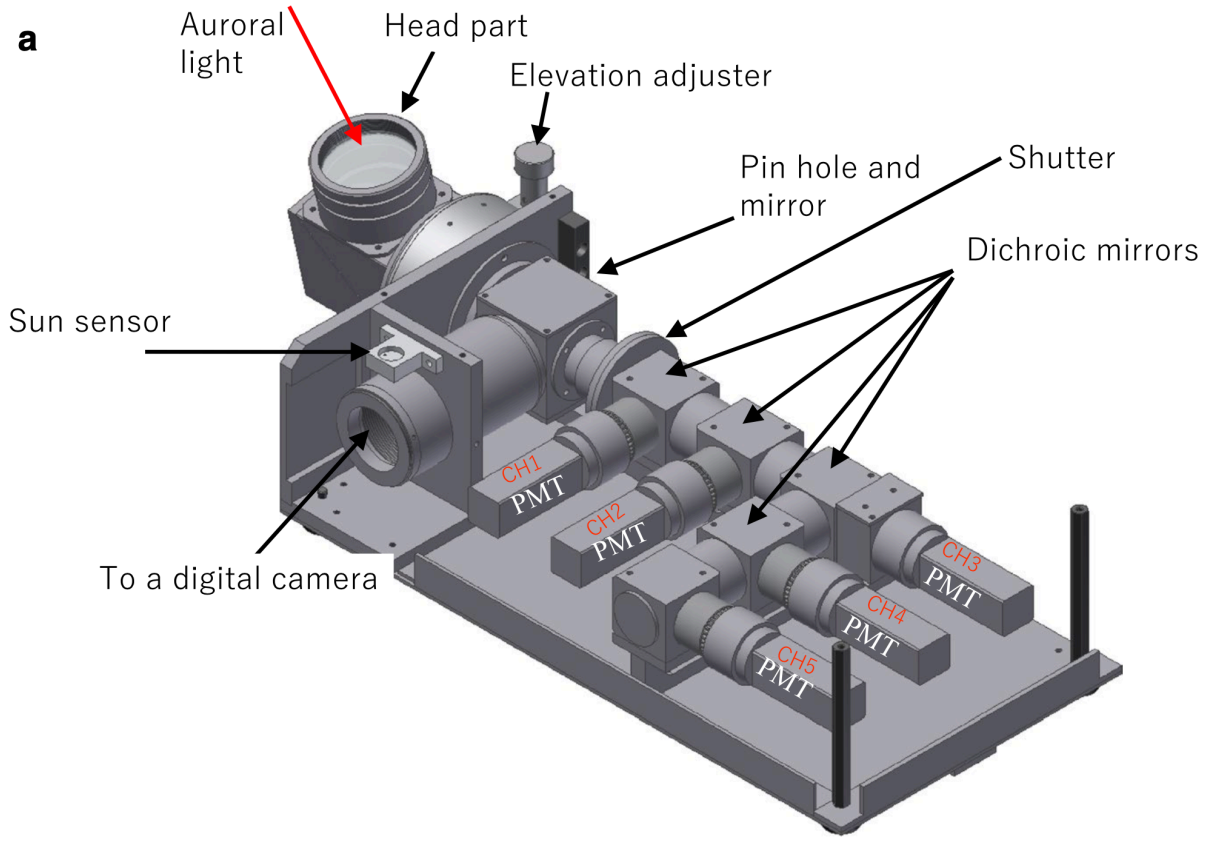

Figure 2.1: Schematic diagram of the five-wavelength photometer. This figure is from *Nozawa et al.* (2018).

The five-wavelength photometer observes the optical emission in the field-aligned direction at a sampling rate of 400 Hz. This sampling rate is sufficient to identify the temporal variation of PsA. To improve the signal-to-noise ratio, the time series were averaged to 1 s in this study. Figure 2.2 shows the optical time series from the five-wavelength photometer at each wavelength (427.8, 557.7, 630.0, 777.4, and 844.6 nm) during a 1 min interval from 03:39 to 03:40 UT on February 14, 2018. Quasi-periodic variation, which is a characteristic feature of PsA, is clearly observed in the time series at all the wavelengths. In addition, there is a time lag between the 427.8 and 557.7 nm emissions.

In Chapter 3, we calculate the lifetime of O(^{1}S) by comparing the 427.8 and 557.7 nm emissions and use this lifetime to estimate the emission altitude of PsA. Note that the five-wavelength photometer is described in detail in *Nozawa et al.* (2018).

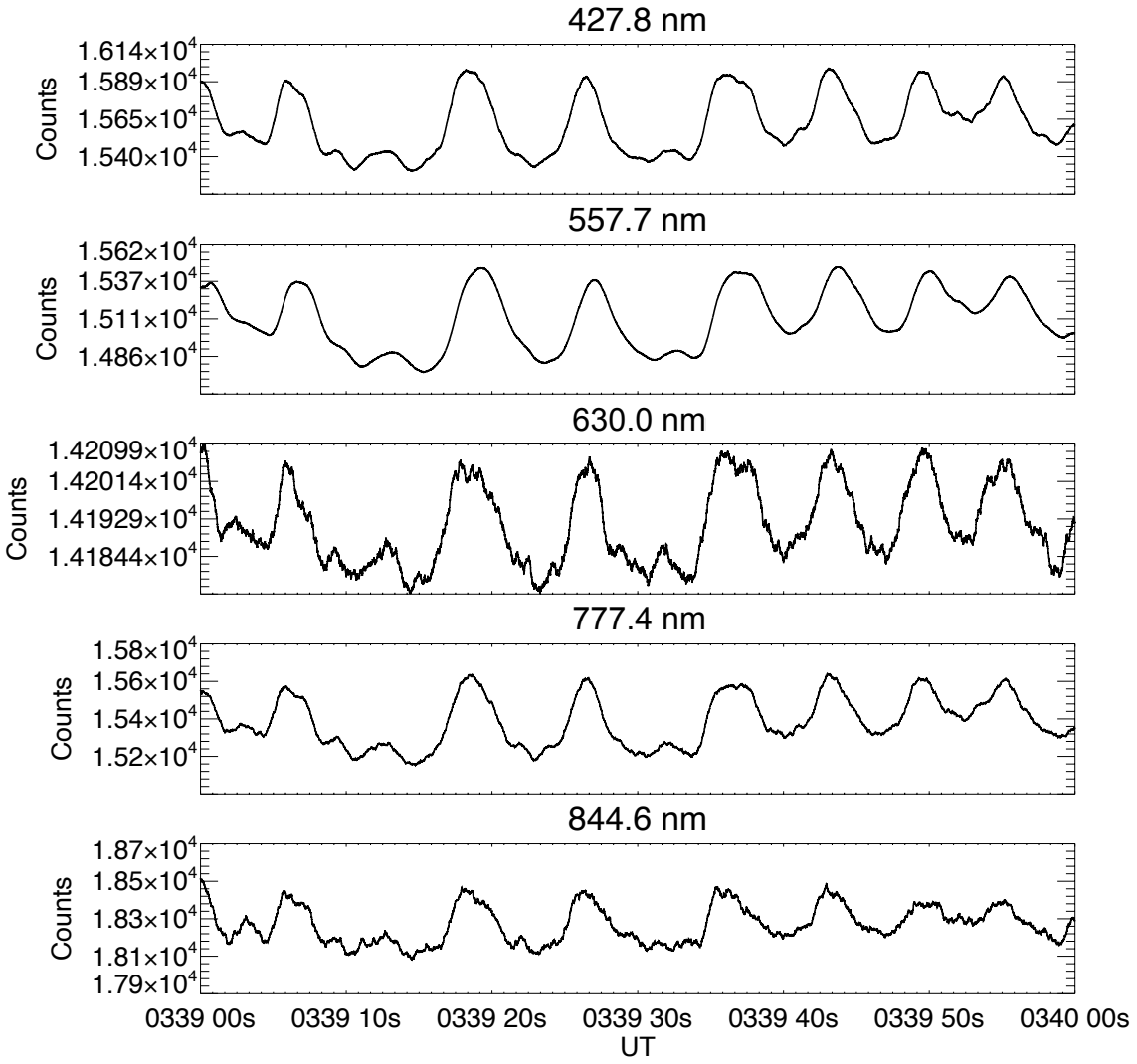

Figure 2.2: Time series of auroral emission at 427.8, 557.7, 630.0, 777.4, and 844.6 nm obtained with five-wavelength photometer during a 1 min interval from 03:39 to 03:40 UT on February 14, 2018.

2.2 EMCCD all-sky imagers

To capture the rapid variations in PsA, such as the internal modulation, we employed four EMCCD all-sky imagers (Hamamatsu Photonics, C9100-23B) with fish-eye lenses (Fujinon Co. Ltd., FE185C086HA-1). A photograph of an EMCCD all-sky imager is shown in Figure 2.3. These imagers have been installed at four stations in Scandinavia. Their FOV covers a region extending from 15° to 35° geographic longitude and from 64° to 73° geographic latitude, which corresponds to a coverage of 500 × 500 km^2. This combined FOV is sufficient to observe PsA occurring on a spatial scale of a few tens to a few hundreds of kilometers.

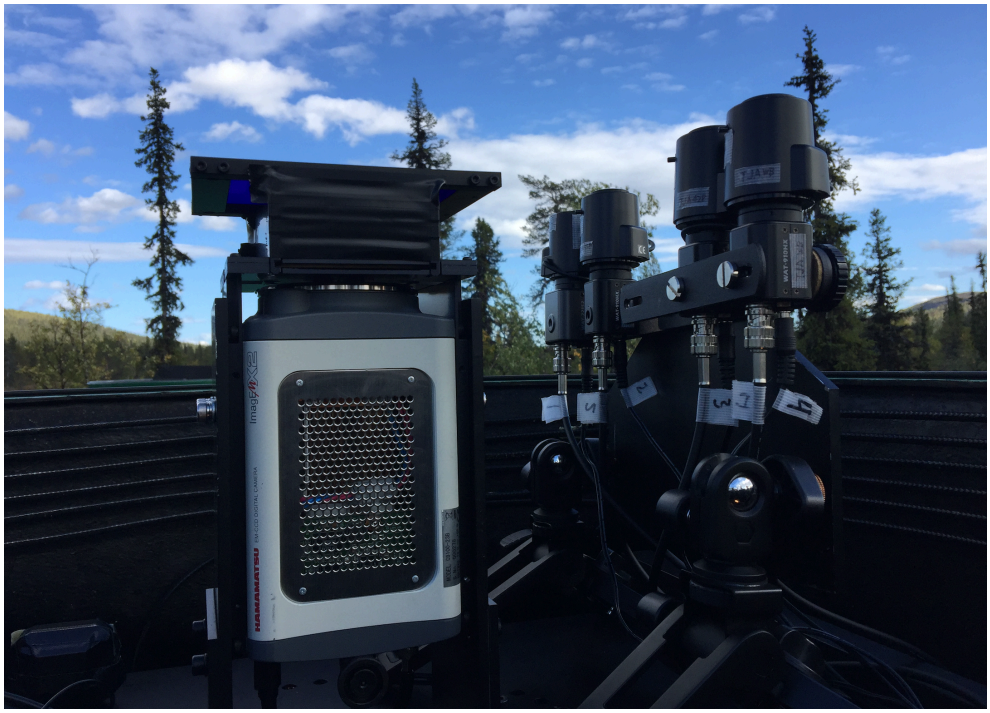

Figure 2.3: EMCCD all-sky imager (Hamamatsu Photonics, C9100-23B) that was used in Tjautjas, Sweden.

As mentioned above, a time delay between electron precipitation and auroral emission occurs at some wavelengths. This time delay may smear the faster variations. For example, the lifetime of $O(^1S)$ at 557.7 nm is approximately 0.7 s, as shown in Section 3; this time delay would smear subsecond variations such as the internal modulation. Thus, wavelengths with such time delays are not suitable for capturing the internal modulation. The EMCCD all-sky imagers employed a BG3 glass filter to observe the N_2^+ first negative

band emission at 427.8 nm, which is a prompt emission. The transmission characteristics of the BG3 glass filter are shown in Figure 2.4. The orange line shows the transmission characteristics of BG3. The vertical lines mark several representative lines and bands of auroral emission at 427.8, 557.7, 630.0, and 650–700 nm. The blue line shows the transmission properties of another glass filter, RG665; however, we did not use this glass filter in this work. The BG3 glass filter enables the EMCCD all-sky imagers to eliminate contamination by the auroral emission at 557.7 and 630.0 nm and observe only the N_2^+ first negative emission at 427.8 nm.

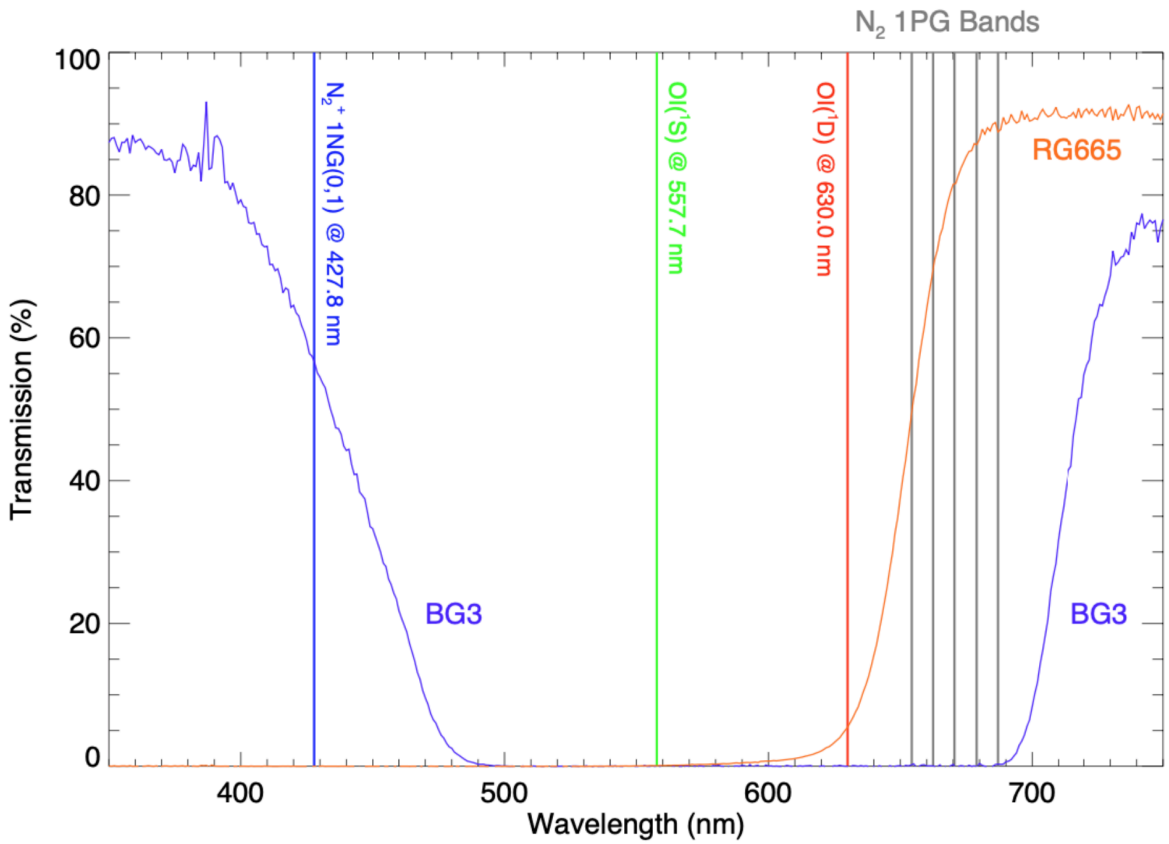

Figure 2.4: Transmission characteristics of BG3 glass filter used on the EMCCD all-sky imagers. The vertical lines mark typical auroral emission lines (427.8, 557.7, and 630.0 nm). This figure is from *Hosokawa et al.* (2020b), which has been submitted to *J. Geophys. Res.: Space Phys.*

The temporal resolution of the EMCCD all-sky imagers is 100 Hz, which is sufficient to capture the internal modulation at a few Hz. The EMCCD all-sky imager used in this system has an imaging component with a spatial resolution of 512 × 512 pixels, but

images are binned in a 2 × 2 window before they are read out. Thus, the final output image has a spatial resolution of 256 × 256 pixels. Figure 2.5 shows the hierarchical temporal variations of PsA observed in Tjautjas, Sweden on March 15, 2018. The top panel shows the time series along a south-to-north cross section, which is called the keogram. A number of vertical stripes appear in the keogram, regardless of the latitude, and each vertical stripe corresponds to the main pulsation of the PsA. In addition, by focusing on the repetition of these stripes, we can see that the stripes appear with various periods (i.e., the periodicity of the main pulsation is very diverse). The middle panel is a magnified view of the green box in the top panel. Several increases in the raw counts can be seen in the northern half of the panel. These increases represent the main pulsation of the PsA. In addition, during the ON phase of the main pulsation, fine vertical stripes appear, which correspond to the internal modulation of the PsA. The bottom panel shows the time series of the raw optical intensity, which was sampled along the horizontal red and blue lines in the middle panel. A hierarchical temporal variation appears, in which the internal modulation is superimposed on the main pulsation, as confirmed from the keogram.

As mentioned above, these EMCCD all-sky imagers have both high temporal resolution and wide FOV coverage. By contrast, conventional ground-based optical observations of PsA have lower temporal resolution or FOV coverage. For example, THEMIS-Ground Based Observatory (THEMIS-GBO) has deployed a number of all-sky imagers in the North American region to reveal the large-scale features of PsA, such as their duration and occurrence distribution (e.g., *Jones et al.*, 2011). However, the time resolution of the THEMIS-GBO all-sky imagers is 3 s, and it is difficult to capture subsecond variations such as the internal modulation of PsA. Most recent ground-based observations with high temporal resolution have been narrow-FOV imagers or single all-sky imager observations. Thus, a combination of four EMCCD all-sky imagers with a high temporal resolution (100 Hz) has never been used before and is ideal for verifying the large-scale characteristics of the hierarchical temporal variations of PsA, especially their latitudinal or longitudinal dependence. Note that in the work described in Chapter 4, we averaged 100 Hz data with a resolution of 25 Hz to reduce the random noise and facilitate effective analysis.

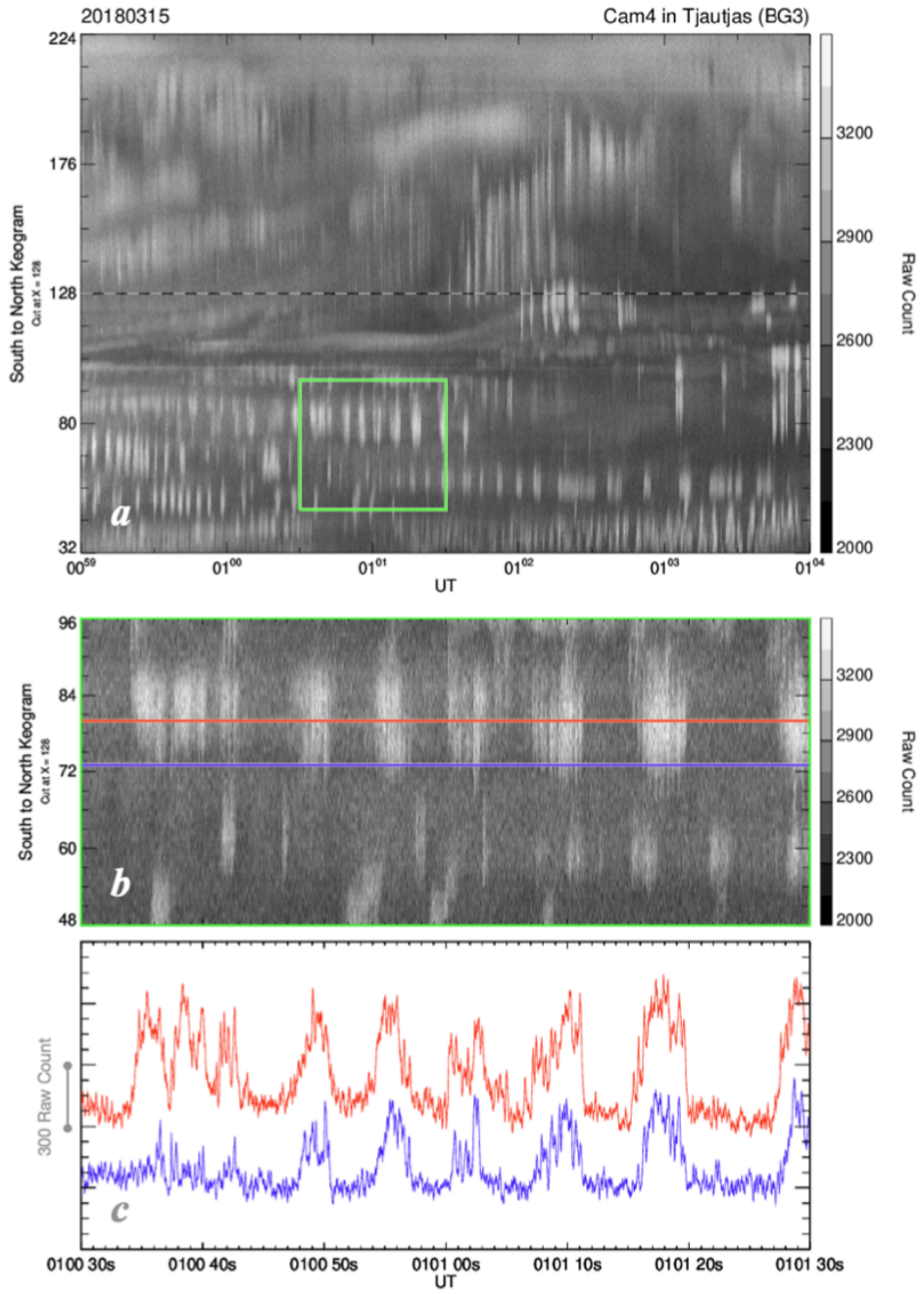

Figure 2.5: Typical example of the hierarchical temporal variations of PsA obtained with the EMCCD all-sky imager in Tjautjas, Sweden on March 15, 2018. Optical time series from 00:59 to 01:04 UT in the form of a south-to-north keogram (top panel), magnified view of the 1 min optical time series within the green box in the southern half of the top panel (middle panel), and two time series of the raw count sampled along the red and blue lines in the middle panel (bottom panel). This figure is from *Hosokawa et al.* (2020b), which has been submitted to *J. Geophys. Res.: Space Phys.*

Chapter 3

Estimation of the emission altitude of pulsating aurora using the five-wavelength photometer

The subject of this chapter is the emission altitude of PsA (i.e., the energy of PsA electrons). As mentioned in the introduction, continuous monitoring of the precipitating electron energy by sounding rockets and IS radar observations has been difficult owing to the limited opportunity for observations. Here, we evaluate a method of estimating the emission altitude of PsA using multiwavelength optical data from a ground-based five-wavelength photometer, which has been operative in Tromsø, Norway, and discuss the characteristics of the PsA electron energy by considering the estimated altitude of the emission. The contents of this chapter were reported in *Kawamura et al.* (2020).

3.1 Introduction

The temporal variation of PsA is associated with quasi-periodic precipitation of energetic electrons from the magnetosphere (e.g., *Sandahl et al.*, 1980). Previous studies have suggested that this quasi-periodic precipitation is caused by wave-particle interaction between whistler-mode chorus waves and ambient electrons, whose energy ranges from a few keVs to a few tens of keVs (e.g., *Miyoshi et al.*, 2010, 2015a, b). In particular, there is reportedly a one-to-one correspondence between the amplitude variation of chorus waves and the luminosity modulation of PsA (*Nishimura et al.*, 2010, 2011). These observational

results imply that PsA is a two-dimensional projection of the behavior of chorus waves in the magnetosphere. Although recent analyses of simultaneous ground-satellite observations have revealed a correspondence between PsA and chorus waves (e.g., *Kasahara et al.*, 2018; *Hosokawa et al.*, 2020a), the factors that control these periodic variations remain unclear.

The emission altitude of PsA has been studied intensively since the 1970s using optical data from ground-based all-sky video cameras (e.g., *Brown et al.*, 1976). The altitude of PsA emission contains information about the energy of the precipitating electrons, which allows us to infer the nature of the wave-particle interaction process. Thus, many studies have investigated the altitude of PsA and the energy of the precipitating electrons. *Brown et al.* (1976) estimated the lower cutoff altitude of PsA emission by the triangulation of two all-sky TV cameras having a common FOV. They showed that the height of PsA emission ranges from 82 to 115 km; the corresponding electron energies range from 50 to 5 keV, which is consistent with direct in-situ observations of PsA electrons by sounding rockets (e.g., *Sandahl et al.*, 1980). However, *Brown et al.* (1976) analyzed only 2 h of optical observations from three nights. A more recent similar analysis by *Partamies et al.* (2017) demonstrated that the height of PsA is slightly lower on the morning side. However, it is still unclear whether this trend is statistically significant because only limited data are available. *Jones et al.* (2009) estimated the energy of PsA electrons from ionospheric electron density observations by the PFISR. More recently, *Hosokawa and Ogawa* (2015) studied the variation in the electron density profile during PsA using the EISCAT radar. They demonstrated that the energy of PsA electrons, inferred from the altitude of ionization, tends to be higher on the morning side (i.e., in the later MLT sector). *Miyoshi et al.* (2015a) identified electron precipitation at a few hundred keVs during simultaneous measurements of PsA with EISCAT and the Van Allen Probes. Then, they proposed a model explaining the scattering of electrons in a wide energy range by considering the propagation of chorus waves toward higher latitudes. As mentioned earlier, the ionospheric electron density variations during PsA have been studied in detail using IS radars. However, the MLT dependence of the altitude of PsA has not been examined using sufficient data. The statistical properties of the PsA electron energy are still unknown. To solve this problem, we need a statistical method of deriving the altitude of PsA emission. *Scourfield et al.* (1971) proposed a procedure for estimating the emission altitude of PsA using the lifetime of $O(^1S)$ excited state atoms from optical observations. Because the

transition from O(^{1}S) to O(^{1}D), which produces 557.7 nm emission, is forbidden, and its lifetime is approximately 0.7 s, a time series of the 557.7 nm emission exhibits a systematic time lag compared to that of an allowed transition such as that at 427.8 nm, which has a lifetime of $\sim 10^{-8}$ s (*Nozawa et al.*, 2018). *Scourfield et al.* (1971) estimated the altitude of the 557.7 nm emission from this delay time because the delay time is longer at higher altitudes. It may be possible to use their method to estimate the energy of PsA electrons. However, *Scourfield et al.* (1971) proposed only the method described earlier, which has not actually been used for the statistical analysis of the altitude of PsA.

In this study, we performed a statistical analysis by applying the method of *Scourfield et al.* (1971) to multiwavelength photometer observations in Tromsø, Norway. This approach enables us to derive the statistical characteristics of the emission altitude of PsA, which provide fundamental information about the energy of PsA electrons and the wave-particle interaction process in the magnetosphere.

3.2 Instruments and datasets

In the current statistical analysis, we employed a five-wavelength photometer (*Nozawa et al.*, 2018) and an EMCCD all-sky imager, both of which were deployed in Tromsø, Norway [69.6°N, 19.2°E, 66.7° magnetic latitude (MLAT)]. The five-wavelength photometer has a FOV of approximately 0.98° and measures the auroral emissions in the field-aligned direction at five wavelengths simultaneously (427.8, 557.7, 630.0, 777.4, and 844.6 nm). The original sampling rate is 400 Hz. The EMCCD all-sky imager observes primarily the N_2 first positive band emissions with a temporal resolution of 100 Hz. This temporal resolution is sufficient to detect the main pulsation of PsA, which has a period ranging from a few seconds to a few tens of seconds. In this study, we employed images from the all-sky camera to identify the appearance of a PsA at the sensing point of the photometer. Figure 3.1 shows a typical example of PsA during a 1 min interval from 03:02 to 03:03 UT on February 24, 2018. Figure 3.1a shows an image from the all-sky imager at 03:02:30 UT. The red circle indicates the FOV of the photometer. Figure 3.1b and 3.1c show the time series of the emission intensity from the photometer at the 427.8 and 557.7 nm, respectively. Note that both time series were averaged using an integration time of 1 s to improve the signal-to-noise ratio. Quasi-periodic fluctuation with a period of approximately 5 s is clear in the time series. In addition, a systematic time lag appears

between the 427.8 and 557.7 nm emissions. By comparing data from these two optical instruments, we identified 37 nights with PsA events during 3 months (January to March, 2018), which were used for statistical analysis.

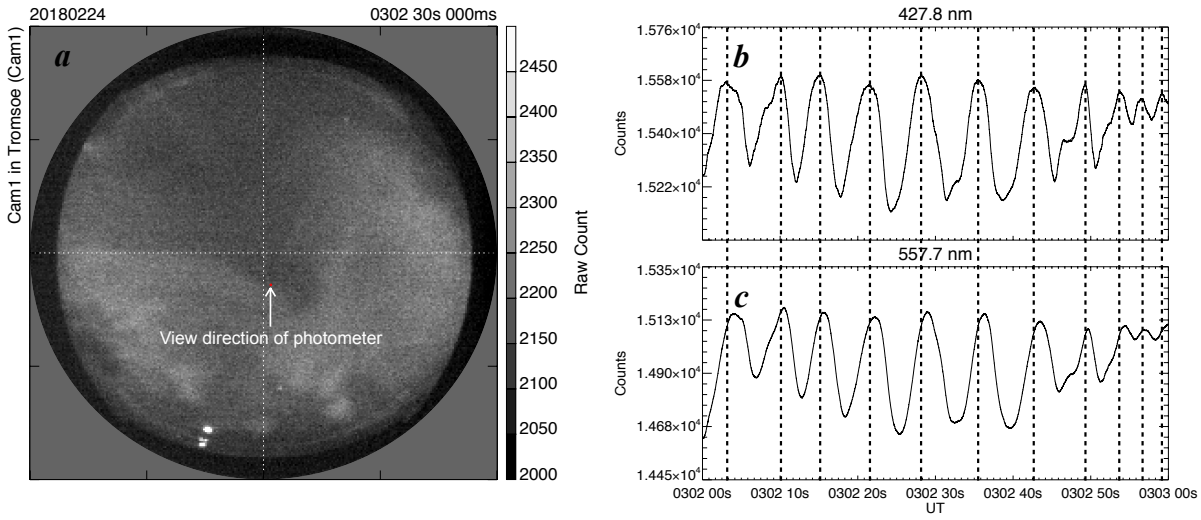

Figure 3.1: **a** Image recorded by the EMCCD all-sky imager in Tromsø at 03:02:30 UT on February 24, 2018. The red circle indicates the FOV of the five-wavelength photometer. Time series of auroral emissions at **b** 427.8 nm and **c** 557.7 nm obtained from the five-wavelength photometer in a 1 min interval from 03:02 to 03:03 UT on the same day.

3.3 Methodology for estimating the lifetime of O(^{1}S)

Before presenting the statistical results, we introduce the methodology for estimating the lifetime of O(^{1}S) using the PsA illustrated in Figure 3.2. In this study, we calculated the lifetime of O(^{1}S) every 1 min by performing a cross-correlation analysis of the time series of the 427.8 and 557.7 nm emissions. We decided to use relatively short (1 min) time intervals for the correlation analysis to eliminate contributions from slower variations. Figure 3.2a and 3.2b show the time series of the 427.8 and 557.7 nm emissions in the same interval shown in Figure 3.1. The time series of the 557.7 nm data clearly has a time delay of 1 s or less compared to that of the 427.8 nm data. Here, we define the lifetime of O(^{1}S) as the time lag giving the maximum cross-correlation coefficient. Note that the correlation coefficient is calculated by shifting the lag from 0 to 2 s with a resolution of

0.01 s, where the time window of the analysis is 30 s. The result of the correlation analysis is presented in Figure 3.2c, where the dashed line indicates the time series at 557.7 nm, and the solid line shows the time-shifted (i.e., delayed by the estimated time lag) variation at 427.8 nm. In this case, the lifetime of O(^{1}S) is estimated to be 0.67 s, as that lag gives the maximum correlation coefficient, 0.99.

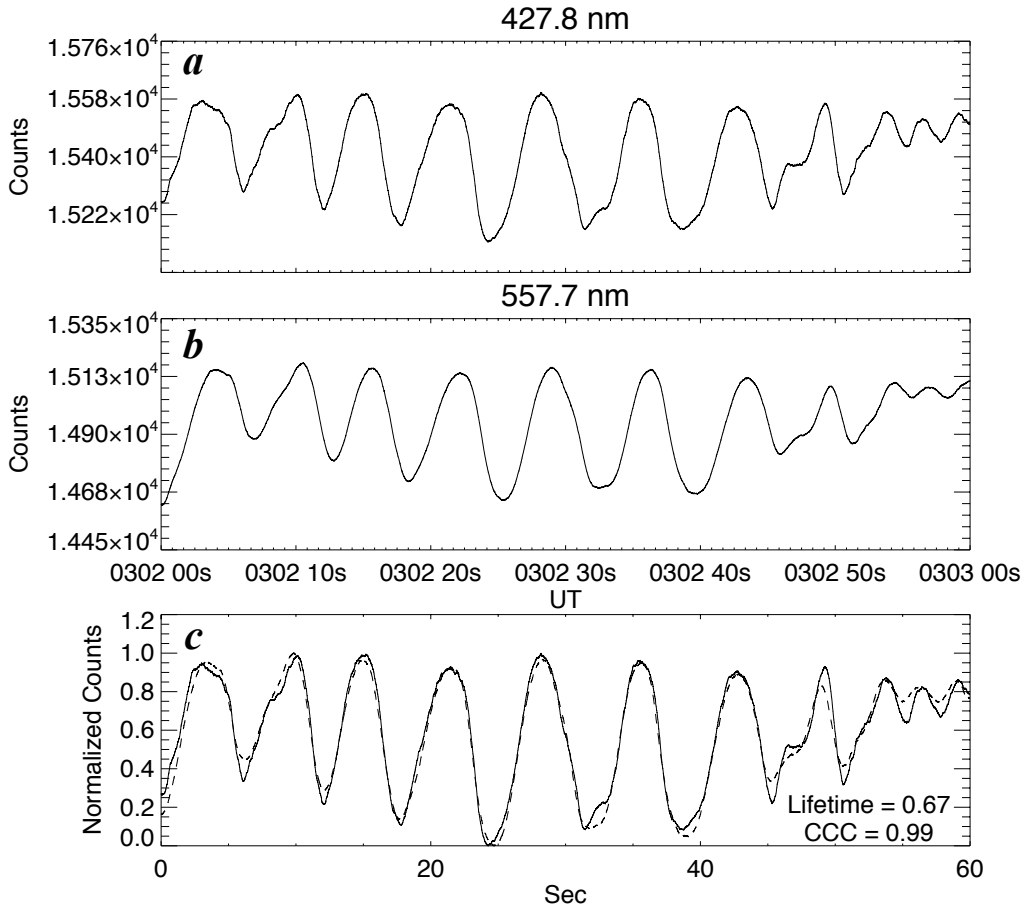

Figure 3.2: Time series of auroral emissions at **a** 427.8 nm and **b** 557.7 nm observed at Tromsø for a 1 min interval from 03:02 to 03:03 UT on February 24, 2018. **c** Comparison of time series of 557.7 nm (dashed line) and 427.8 nm (solid line) emissions. The time series of the 427.8 nm emission is delayed by 0.67 s, which corresponds to the lifetime of O(^{1}S).

3.4 Statistics of distribution of the lifetime of O(^{1}S)

Figure 3.3a shows the distribution of the lifetime of O(^{1}S) derived by applying the procedure described earlier to 2856 PsA events, each of which had a duration of 1 min. The distribution has a prominent peak (mode) at approximately 0.7 s, and the mean of the distribution is 0.67 s. *Brekke and Henriksen* (1972) also calculated the lifetime of O(^{1}S) using a photometer in Tromsø, Norway. In their result, the lifetime was distributed from 0.5 to 1 s, and the mean was 0.80 s. Our result generally agrees with that of *Brekke and Henriksen* (1972). In our analysis, however, the mean value is slightly shorter than theirs. The time window for the cross-correlation analyses of *Brekke and Henriksen* (1972) was 5 min, whereas our study used a 1 min window. This difference might have resulted in the slight difference between these two results. However, when we performed the cross-correlation analysis using several different time windows, no significant differences were found; thus, the reason behind the difference is still unclear.

We classified events according to MLT and investigated the MLT dependence of the lifetime of O(^{1}S). The results are summarized in Figure 3.3b–3.3d. These panels show the distributions of the lifetime in three MLT sectors, i.e., 20–03 MLT, 03–05 MLT, and 05–08 MLT, respectively. The mode and mean of the lifetime are 0.70 and 0.70 s for 20–03 MLT, 0.65 and 0.69 s for 03–05 MLT, and 0.50 and 0.64 s for 05–08 MLT. In addition, the shape of the distributions reveals that the weight is shifted to the shorter area on the morning side. In particular, for 05–08 MLT (Figure 3.3d), there is a significant population having a lifetime of approximately 0.60 s, which is not seen before 05 MLT (Figure 3.3b and 3.3c). In the following section, we will estimate the altitude of the PsA emission from these lifetime values.

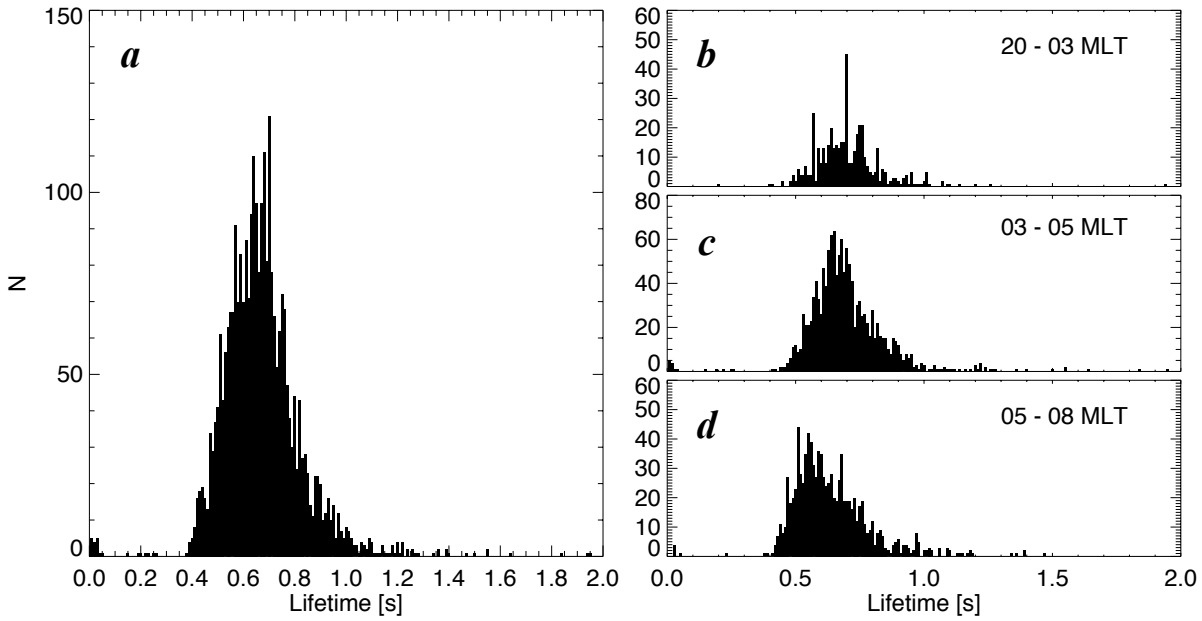

Figure 3.3: **a** Statistical distribution of the lifetime of O(^{1}S). The distributions of the lifetime for three MLT sectors: **b** 20–03 MLT, **c** 03–05 MLT, and **d** 05–08 MLT.

3.5 Calculating the effective altitude of pulsating aurora

Here, we introduce a method of deriving the altitude of the 557.7 nm emission from its lifetime (*Scourfield et al.*, 1971). There are three routes through which an oxygen atom in the excited state transitions to the ground state. Here, we define I as the intensity of the 557.7 nm emission, which can be expressed as follows (*Brekke and Henriksen*, 1972):

$$I = A_{32}/(A_{31} + A_{32} + d_3) \times Q_0 \tag{3.1}$$

where A_{31} and A_{32} are the probabilities of radiative transitions from the O(^{1}S) state to the O(^{1}D) and O(^{3}P) states, respectively, and d_3 is the probability of the collisional transition of the O(^{1}S) state. Q_0 is the excitation rate of the O(^{1}S) state. The lifetime of the O(^{1}S) state is calculated as follows using these parameters:

$$\tau = 1/(A_{31} + A_{32} + d_3) \tag{3.2}$$

The values of A_{31} and A_{32} in this equation have been estimated experimentally as 1.28 s^{-1} and 0.078 s^{-1}, respectively (*Brekke and Henriksen*, 1972). Because we can estimate τ

from actual observations of PsA, the collisional transition probability d_3 can be derived for each PsA. Assuming that there is no collisional change in the O(^{1}S) state, the lifetime is approximately 0.74 s. Therefore, in the estimation of the emission altitude, we used only lifetime values that were less than or equal to 0.74 s. Here, we assumed that the collisional transition is owing to O_2 and N_2, and thus, d_3 can be expressed as follows:

$$d_3 = q_{O_2} \times n(O_2) + q_{N_2} \times n(N_2) \tag{3.3}$$

where q_{O_2} and q_{N_2} are the quenching rate coefficients of O_2 and N_2, and $n(O_2)$ and $n(N_2)$ are the densities of O_2 and N_2, respectively. Using the theoretical values of q_{O_2} and q_{N_2}, which are 3.0×10^{13} cm^3 s^{-1} (*Zipf*, 1969) and $< 10^{17}$ cm^3 s^{-1} (*Hunten and McElroy*, 1966), respectively, the collisional transition owing to N_2 can be ignored. Thus, d_3 can be simply expressed by the following equation (*Scourfield et al.*, 1971):

$$d_3 = q_{O_2} \times n(O_2) \tag{3.4}$$

Using the theoretical value of q_{O_2}, we can determine the density of O_2 and then estimate the emission altitude of PsA by comparing the obtained value of $n(O_2)$ with that from the neutral atmosphere model (Mass Spectrometer and Incoherent Scatter: MSIS, *Hedin*, 1991) sampled every 1 km. Figure 3.4 is the altitude profile of $n(O_2)$ obtained by the MSIS model at 01:00 UT on February 19, 2018. The vertical and horizontal axes indicate the altitude and $n(O_2)$, respectively. We defined the emission altitude of PsA as that where the difference between the modeled $n(O_2)$ obtained by MSIS and that estimated by our method is minimum. The emission layer of PsA can be measured by IS radar observations such as those of EISCAT, and its thickness is approximately 20 km (*Jones et al.*, 2009; *Hosokawa and Ogawa*, 2015). However, our method cannot directly estimate the lower cutoff altitude of the optical emission or the thickness of the emission layer. The reason is simply that it is difficult to obtain the height profile of the emission from optical observations. Therefore, we need to bear in mind that the emission altitude estimated in this study is the volume altitude, which is, roughly, the center of the emission layer rather than the lower cutoff altitude.

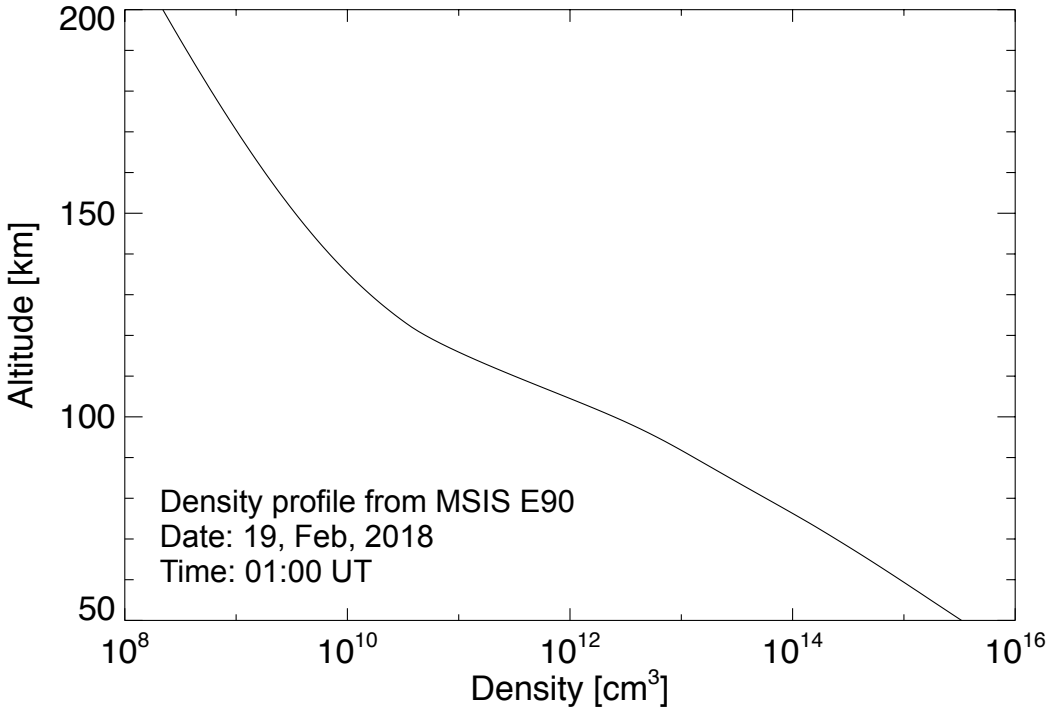

Figure 3.4: Altitude profile of $n(O_2)$ obtained by MSIS model calculation.

3.6 Accuracy of estimating of the emission altitude

To evaluate the validity of the current method, we compare the emission altitude of a PsA estimated from the lifetime of O(^{1}S) and the altitude profile of the electron density from the EISCAT UHF radar, which has a FOV of $< 0.7°$. The raw electron density (i.e., power profile data) was obtained with an altitude resolution of approximately 0.6 km. During 2.5 h, from 00:30 to 03:00 UT on February 19, 2018, an intense PsA and the corresponding ionization were observed by the five-wavelength photometer and the EISCAT UHF radar, respectively, at the same location. Figure 3.5a shows the variation in the ionospheric electron density from the EISCAT UHF radar. In this time interval, especially after 01:00 UT, a PsA was observed almost continuously by the photometer. However, the low-altitude cutoff of the ionization varied with time, indicating that the characteristic energy of the precipitating electrons was not uniform during this episode.

Figure 3.5b plots time series of the emission altitude of the PsA derived from the lifetime analysis (blue line) and from h_mE (the peak height of the E region electron

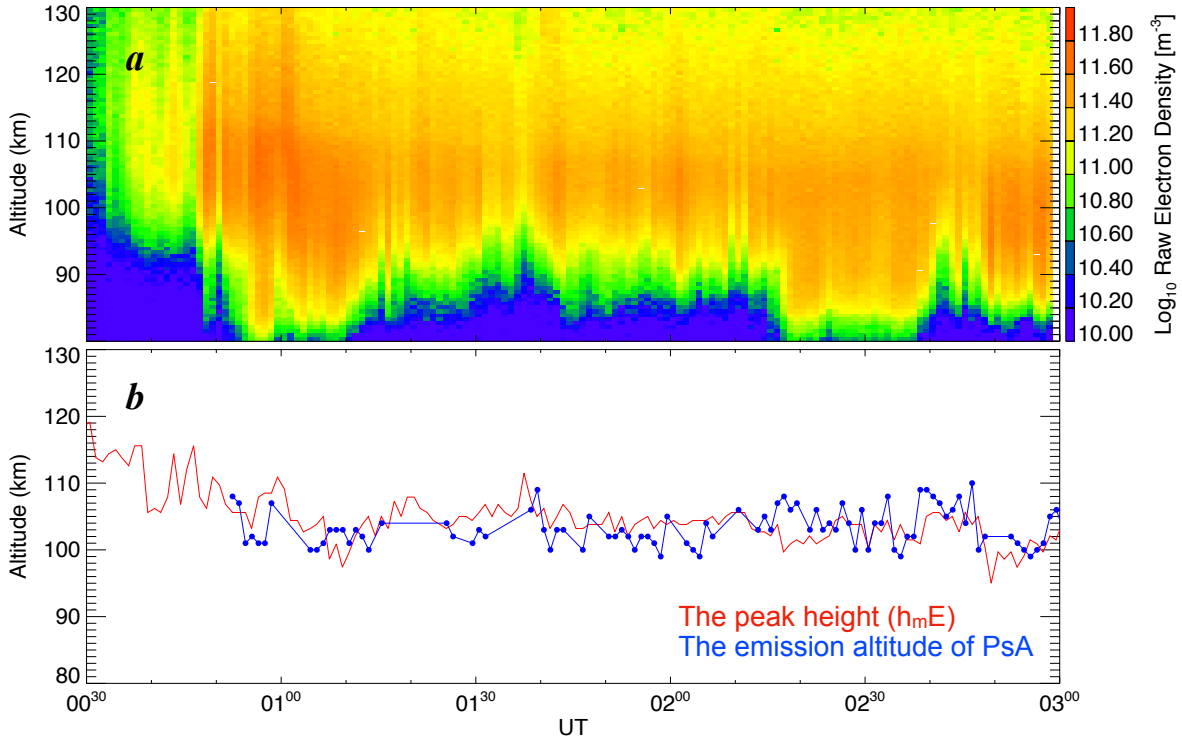

Figure 3.5: **a** Altitude–time plot of the ionospheric raw electron density (i.e., power profile data) obtained by the EISCAT UHF radar during a PsA from 00:30 to 03:00 UT on February 19, 2018. **b** Time series of the emission altitude of the PsA estimated from the lifetime of O(^{1}S) (blue line) and the peak height of E region ionization (h_mE) from the EISCAT UHF radar (red line).

density enhancement: red line). h_mE was derived directly from the altitude profile of the electron density shown in Figure 3.5a. Note that we averaged the original h_mE values in a time window of 1 min to improve the signal-to-noise ratio.

Although they differ slightly, mainly because of the limited altitude resolution of h_mE, the altitude ranges based on PsA emission and h_mE are similar. In particular, during the 30 min from 02:30 to 03:00 UT, they show rather good agreement. This indicates that the emission altitude of a PsA can be a good proxy for the energy of the precipitating electrons during the PsA.

3.7 Dependence of altitude of pulsating aurora on magnetic local time

Figure 3.6a shows the MLT distribution of the occurrence of PsA events. Most events are distributed from magnetic midnight to 08 MLT, and the mode of the distribution is located around 04 MLT. This distribution is in good agreement with those reported in past studies of the occurrence distribution of PsA (e.g., *Jones et al.*, 2011). Figure 3.6b shows the MLT variation in the PsA emission altitude estimated in this study. Each dot corresponds to the emission altitude derived for a PsA interval. The red crosses indicate the averages calculated in each 1 h MLT bin, and the red bars give the standard deviation of the distribution. The emission altitude is lower on the morning side, especially after 06 MLT, whereas the central altitude remains high at approximately 108 km in the earlier MLT sector. After 06 MLT, the minimum emission altitude is as low as ∼95 km, which corresponds to a precipitating electron energy of 30 keV.

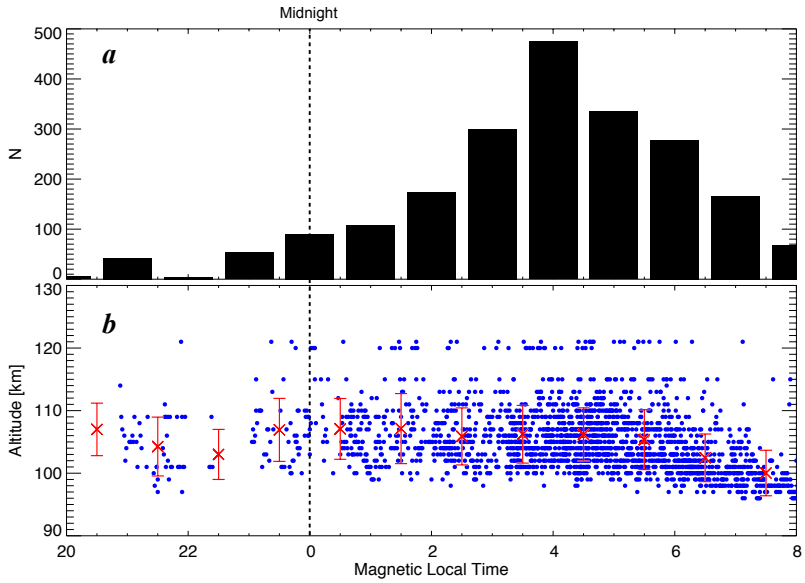

Figure 3.6: **a** MLT distribution of intervals of PsA sampled from 37 nights of observations. **b** Dependence of PsA altitude on MLT. The red crosses and vertical bars indicate the average and standard deviation, respectively, of the PsA altitude calculated in each 1 h MLT bin.

3.8 Discussion

As shown in Figure 3.5b, the emission altitude of PsA is distributed from 95 to 115 km, which corresponds to the precipitation of 5–30 keV electrons (*Turunen et al.*, 2009). This result is consistent with several early observations of PsA electrons by sounding rockets (*Sandahl et al.*, 1980; *Yau et al.*, 1981). *Miyoshi et al.* (2010, 2015b) also used simultaneous particle and optical data from the Reimei satellite to identify the precipitation of few-keV electrons causing a PsA. *Hosokawa and Ogawa* (2015) investigated the variation in the ionospheric electron density profile during PsA using the EISCAT radars and indicated that the energy of PsA electrons tends to be higher on the morning side. This tendency appears in Figure 3.5b, where the emission altitude decreases drastically after 06 MLT. This systematic change is consistent with the MLT variation in the E region peak height (h_mE) demonstrated by *Hosokawa and Ogawa* (2015). A similar MLT dependence was reported by *Partamies et al.* (2017), who showed the MLT dependence of the emission layer of PsA.

Here, we discuss the reason that the emission altitude of PsA decreases after 06 MLT. One possible explanation is the change in the background magnetic field intensity in the magnetosphere with MLT, which occurs because the resonance energy of electrons in first-order cyclotron resonant scattering with chorus waves is proportional to the square of the ambient magnetic field intensity (*Kennel and Petschek* 1966):

$$E_R = \frac{B^2}{2\mu_0 N}\frac{f_{ce}}{f}(1-\frac{f}{f_{ce}})^3 \tag{3.5}$$

where B is the ambient magnetic field intensity, μ_0 is the permeability of vacuum, N is the thermal plasma density, f_{ce} is the cyclotron frequency, and f is the chorus wave frequency. Note that this approximation is valid when we assume $f_{pe}/f_{ce} \gg 1$ or $f/f_{ce} \ll 1$(*Kennel and Petschek*, 1966). *Hosokawa and Ogawa* (2015) calculated the magnetic field intensity and discussed the MLT variation in the resonance energy. However, they did not evaluate the contribution of the thermal plasma density to the resonance energy. We calculated the magnetic field intensity at the conjugate point of Tromsø using the Tsyganenko 89 magnetic field model (*Tsyganenko*, 1989) and the thermal plasma density using the model of *Sheeley et al.* (2001) for the PsA event on February 19, 2018. However, the calculated value of the resonance energy changed very slightly with MLT, implying that the drastic decrease in emission altitude cannot be explained only by the effect of MLT

on the ambient parameters. *Miyoshi et al.* (2015a) recently reported that the resonance energy increases as a chorus wave propagates from the magnetic equator to off-equator. If chorus waves propagate further off-equator on the morning side, more energetic electrons can be precipitated by cyclotron resonance. Thus, the energy of PsA electrons should be analyzed considering both the ambient parameters (magnetic field intensity and thermal plasma density) and the propagation characteristics of chorus waves along the field lines.

3.9 Conclusions

In the work described in this chapter, we estimated the emission altitude of PsA using the lifetime of O(^{1}S) derived from observations using the five-wavelength photometer in Tromsø, Norway. The main results are summarized as follows:

1. We statistically analyzed the emission altitude of PsA using the observed value of the lifetime of O(^{1}S). The distribution of the lifetime has a strong peak at approximately 0.7 s, and the mean lifetime is 0.67 s. These automatically estimated time constants are in good agreement with those derived in previous studies, implying the feasibility of the method for estimating the lifetime.

2. By comparing the emission altitude of a PsA with the peak height of the E region ionization obtained by the EISCAT UHF radar, we demonstrated that the peak height of the electron density (i.e., the peak of ionization) roughly matches the central emission altitude of the PsA.

3. Most of the emission altitudes of PsA ranged from 95 to 115 km, and the corresponding precipitating electron energies ranged from 5 to 30 keV. This energy range is consistent with the results of previous in-situ rocket observations.

4. The emission altitude tends to be significantly lower on the morning side after 06 MLT, suggesting that the energy of the precipitating electrons should be higher in the later MLT sector.

As mentioned earlier, PsA electrons have a wide energy range of 5 to 30 keV, and their energy tends to be higher toward the morning side. These results imply that PsA electrons have diverse characteristics (e.g., energy range and MLT variation). In the next

chapter, based on these diverse characteristics of PsA electrons, we discuss the formation mechanism of the hierarchical temporal variations of PsA.

Chapter 4

Factors controlling the internal modulation of pulsating aurora: Multi-point high-speed optical observations in Scandinavia

In this chapter, by considering the energy range of PsA electrons revealed in the previous chapter, we discuss the generation mechanism of the hierarchical temporal variations of PsA. These variations (i.e., the presence/absence of internal modulation) depends not only on the discreteness of the chorus elements but also on the time required for electrons to move from the magnetosphere to the ionosphere. This travel time depends primarily on the electron energy; thus, it is possible that the variation in travel time controls the presence of internal modulation. Here, we derive the spatial distribution of the hierarchical temporal variations of PsA using the EMCCD all-sky imagers installed at four stations in Scandinavia. Based on the derived spatial distribution and the energy range of PsA electrons, we discuss the factors controlling the hierarchical temporal variations of PsA.

4.1 Introduction

Previous studies (e.g., those reviewed in *Li et al.* (2012)) have suggested that periodic electron precipitation during PsA is caused by wave-particle interactions between whistler-mode chorus waves (*Thorne at al.*, 2010) and trapped magnetospheric electrons with

energies of a few keVs to a few tens of keVs (e.g., *Miyoshi et al.*, 2015a). Similar to PsA, chorus waves are known to appear as clusters (or bursts) of individual chorus elements (e.g., *Santolik et al.*, 2003); chorus waves also exhibit two different periodicities: the so-called bursts of chorus and the repeated occurrence of individual chorus elements. This similarity has allowed us to discuss the characteristics of multiple temporal variations of PsA in association with the similar simultaneous appearance of chorus elements. In particular, some studies reported a one-to-one correspondence between the amplitude variation in chorus waves (i.e., bursts of chorus) and the main pulsation of PsA (*Nishimura et al.*, 2010, 2011; *Kasahara et al.*, 2018).

The period of PsA was extensively studied in the 1980s using images from ground-based all-sky video cameras. For example, *Duncan et al.* (1981) derived the occurrence distribution of the period of the main pulsation using optical data from seven nights. They concluded that the dominant period of the main pulsation ranged from 5 to 10 s. Later, *Yamamoto* (1988) investigated the periodicity of the main pulsation and showed that the average durations of the ON and OFF phases were 6.2 $\pm$ 1.7 s and 14.5 $\pm$ 5.3 s, respectively, and the average period was 20.7 $\pm$ 5.4 s. More recently, *Nishiyama et al.* (2014) examined high-time-resolution optical data from an EMCCD all-sky imager at Poker Flat, Alaska, and demonstrated the statistical properties of both the main pulsation and internal modulation. According to their statistical analysis, the frequency of the internal modulation was distributed from 1.5 to 3.3 Hz, which was consistent with the quasi 3 Hz modulation (e.g., *Royrvik and Davis*, 1977). Although the amount of data used in these studies was still limited, they revealed the statistical characteristics of the period of the hierarchical temporal variations of PsA to some extent.

Hosokawa et al. (2020a) recently identified a remarkable correlation between the internal modulation of PsA and the repeated appearance of chorus elements. This good correspondence was obtained during an interval of simultaneous observations of PsA with a ground-based high-speed EMCCD imager and the ARASE satellite. They concluded that the discreteness of the chorus elements is one of the primary factors controlling the presence/absence of subsecond internal modulation of the luminosity variations of PsA. However, owing to the lack of optical observations in a wide area with sufficient temporal resolution, it is still unclear how often the quasi 3 Hz internal modulation is embedded within the overall temporal variations of PsA. Specifically, we still do not know whether all PsA are accompanied by internal modulations. In this study, we use highly

sensitive EMCCD all-sky imagers at four stations in northern Scandinavia (Sodankylä and Kevo in Finland, Tromsø in Norway, and Tjautjas in Sweden) to analyze the periodicity of the hierarchical temporal variations of PsA. Specifically, we investigate the spatial distribution of the proportion of PsA with/without internal modulations. Based on the obtained spatial distribution, we discuss the extent to which the nature of discrete chorus elements can control the subsecond variations of PsA.

4.2 Instruments and Datasets

We employed four EMCCD all-sky imagers in northern Scandinavia. These imagers were deployed and have been used for simultaneous observations of PsA with the ARASE satellite. The locations of the imagers are summarized in Table 4.1. The FOV of these imagers is approximately 500 × 500 km^2, which is sufficient to capture PsA appearing in a region of several hundreds of square kilometers. Figure 4.1 shows an example of a mosaic image obtained by combining data from all four EMCCD all-sky imagers at 01:05:00 UT on March 15, 2018. These imagers employ a BG3 glass filter to observe the N_2^+ first negative band emission at 427.8 nm, which is a type of prompt auroral emission. The imaging component is 512 × 512 pixels. However, the images are binned in 2 × 2 windows before they are read out from the imager, and the data are saved as 256 × 256 pixel raw images. The temporal resolution of the imaging is 100 Hz, which is fast enough to capture the internal modulation at a few Hz. In this study, the 100 Hz sampled raw images are averaged with a resolution of 25 Hz to reduce the random noise and facilitate the analyses.

Table 4.1: Locations of four EMCCD all-sky imagers in northern Scandinavia

Station	Tromsø (TRO)	Sodankylä (SOD)	Kevo (KEV)	Tjautjas (TJA)
Geo. Lat.	69.58	67.37	69.76	67.31
Geo. Lon.	19.23	26.63	27.01	20.73
Mag. Lat.	66.76	64.19	66.57	64.39

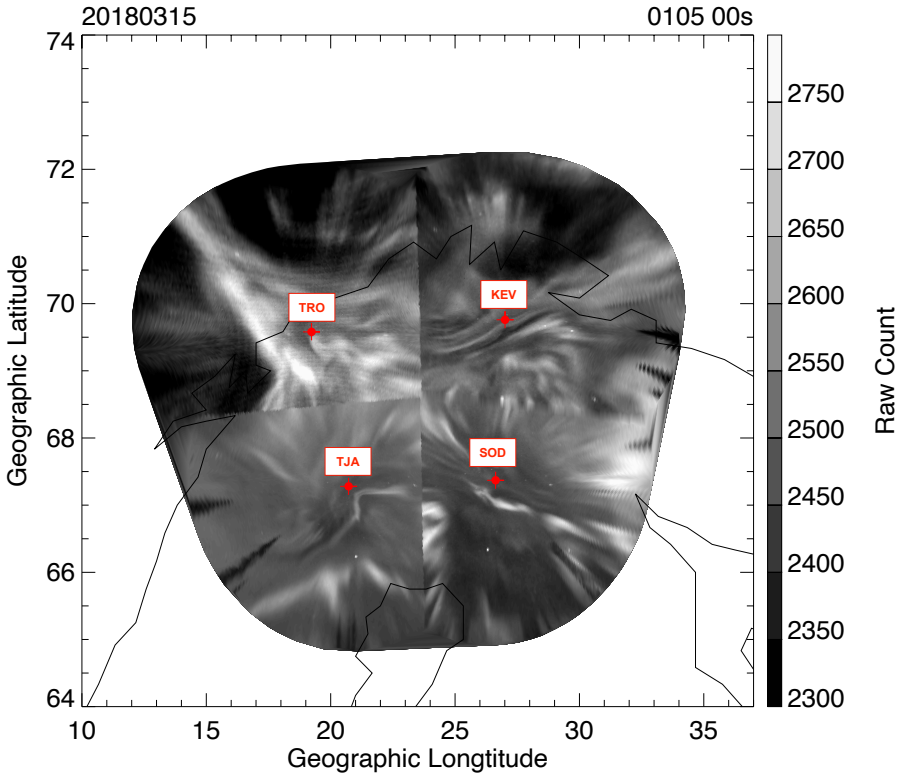

Figure 4.1: Mosaic image of four EMCCD all-sky imager observations at 01:05:00 UT on March 15, 2018.

Figure 4.2 displays a typical example of the temporal variation of PsA obtained by the EMCCD all-sky imager in Tjautjas during a 10 s interval from 01:03:20 to 01:03:30 UT on March 15, 2018. Figure 4.2a is a keogram along the south-to-north cross section near the center of the FOV. Two increases in optical intensity appear, from 01:03:22 to 01:03:24 UT and from 01:03:25 to 01:03:27 UT, which represent the main pulsation of the PsA. Fine-scale vertical stripes also appear during the ON phase of the main pulsation, which are the signatures of the quasi 3 Hz internal modulations. Figure 4.2b shows a time series of the raw optical intensity sampled along the horizontal black line in Figure 4.2a. Hierarchical temporal variations again appear, where the internal modulations are embedded in the main pulsation (very small peaks during the enhancement of the main pulsation). For this analysis, we extracted a PsA event during a 1 h interval from 00:30:00 to 01:30:00 UT on March 15, 2018, in which an intense PsA was simultaneously observed at the four stations in Scandinavia.

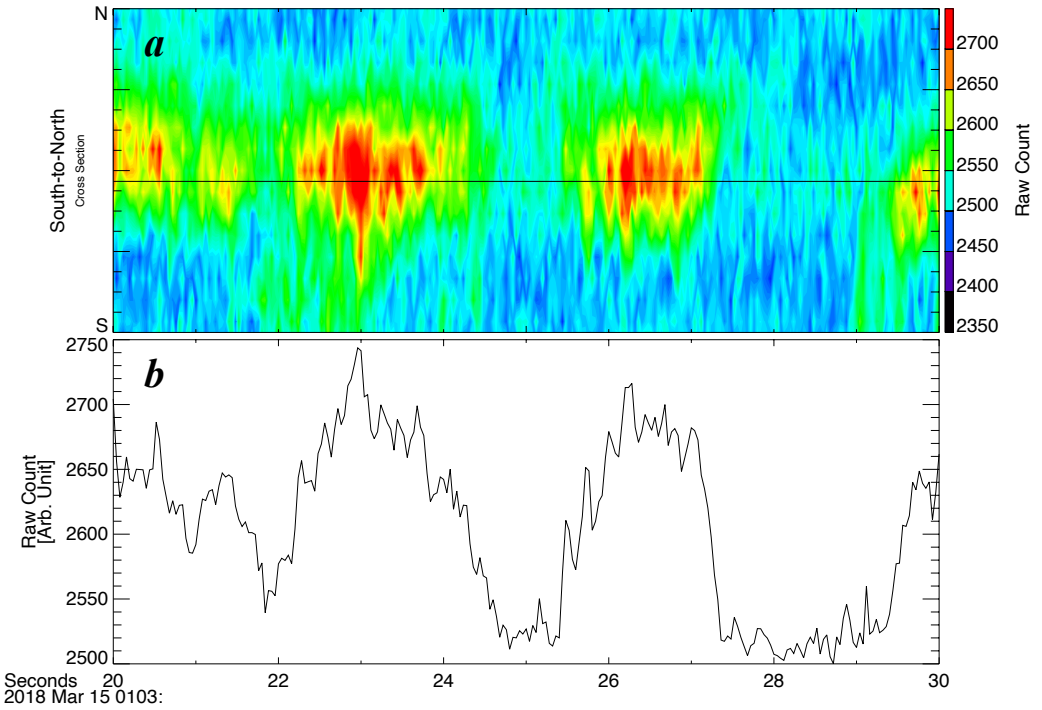

Figure 4.2: **a** South-to-north keogram from all-sky images taken in Tjautjas during a 10 s interval, from 01:03:20 to 01:03:30 UT, on March 15, 2018. **b** Time series of raw auroral luminosity along the horizontal black line in **a**.

4.3 Method

Before presenting the results, we introduce the data processing procedure by illustrating a few examples of the multiscale temporal variations of PsA. Figure 4.3a shows a time series of the temporal variations of PsA observed by the EMCCD all-sky imager at Tjautjas from 01:01:00 to 01:04:00 UT on March 15, 2018. In this time series, all the peaks in the raw count correspond to the main pulsation, which has a period of approximately 5 s. To analyze the main pulsation, we used 1 Hz averaged data to simplify the signal processing. Before analyzing the period of the main pulsation, we took the time derivative of the original time series to eliminate the contribution of slower variations. Figure 4.3b shows the main pulsation component obtained by taking the time derivative of the original time series (Figure 4.3a). We derived the period–time (p–t) diagram (Figure 4.3c) by applying the S-transformation to the fluctuating component in Figure 4.3b. Note that we produced

the p–t diagram every 30 min. Specifically, Figure 4.3a, 4.3b, and 4.3c are magnified views of 3 min of the 30 min time window. In the p–t diagram, increases in amplitude appear around or slightly below 5 s, which is in good agreement with the apparent period of the main pulsation observed in the raw time series (Figure 4.3a).

Figure 4.3d shows a magnified time series in a 10 s interval from 01:03:20 to 01:03:30 UT, which is part of the event shown in Figure 4.3a. Note that the temporal resolution of the time series in Figure 4.3d is 25 Hz, which is suitable for visualizing the subsecond internal modulations. Here, very small spiky peaks appear during the large-scale enhancement of the optical intensity (i.e., the main pulsation), which are signatures of the internal modulations. Before analyzing the frequency of the internal modulations, the slower variation associated with the main pulsation should be removed. For this purpose, we first produced a background trend representing the main pulsation by connecting local minimum points in a sliding window including five data points. Then, the main pulsation component was subtracted from the original time series to extract the internal modulations. The result is presented in Figure 4.3e, where only the spiky subsecond modulations appear. To estimate the frequency of the internal modulations, we applied the wavelet transform to the time series in Figure 4.3e and derived the f–t diagram, which is shown in Figure 4.3f. For the frequency analysis of the internal modulations, we produced the f–t diagram every 1 min. Figures 4.3d, 4.3e, and 4.3f are magnified views of 10 s of the 1 min time window. In the f–t diagram, a continuous band of large wavelet amplitude appears at approximately 3 Hz, which would correspond to the frequency of the internal modulation.

To perform an analysis using a certain amount of 2D data, we automatically selected the main pulsation and internal modulation from the p–t/f–t diagrams using the following method. First, we extracted the periods of the main pulsation and internal modulation when the S-transform/wavelet amplitude in the period range of the main pulsation (2–30 s) and the frequency band of the internal modulation (1–12.5 Hz) were larger than threshold values. We selected the main pulsation when the intensity of the obtained S-transform amplitude was larger than 100. For the internal modulation, we employed different threshold values of the wavelet amplitude for the four stations because of differences in the sensitivity and surrounding observation conditions of the EMCCD all-sky imagers. These threshold values were empirically determined to be 100, 15, 15, and 50 for Tromsø, Sodankylä, Tjautjas, and Kevo, respectively. In addition, to remove contam-

ination by discrete aurora, we discarded data points for which the brightness exceeded another threshold value. These threshold values for extracting PsA and discarding discrete aurora are constant over the entire time period analyzed. This method allowed us to automatically detect the hierarchical temporal variations of PsA from a large amount of data with high temporal resolution without manual inspection.

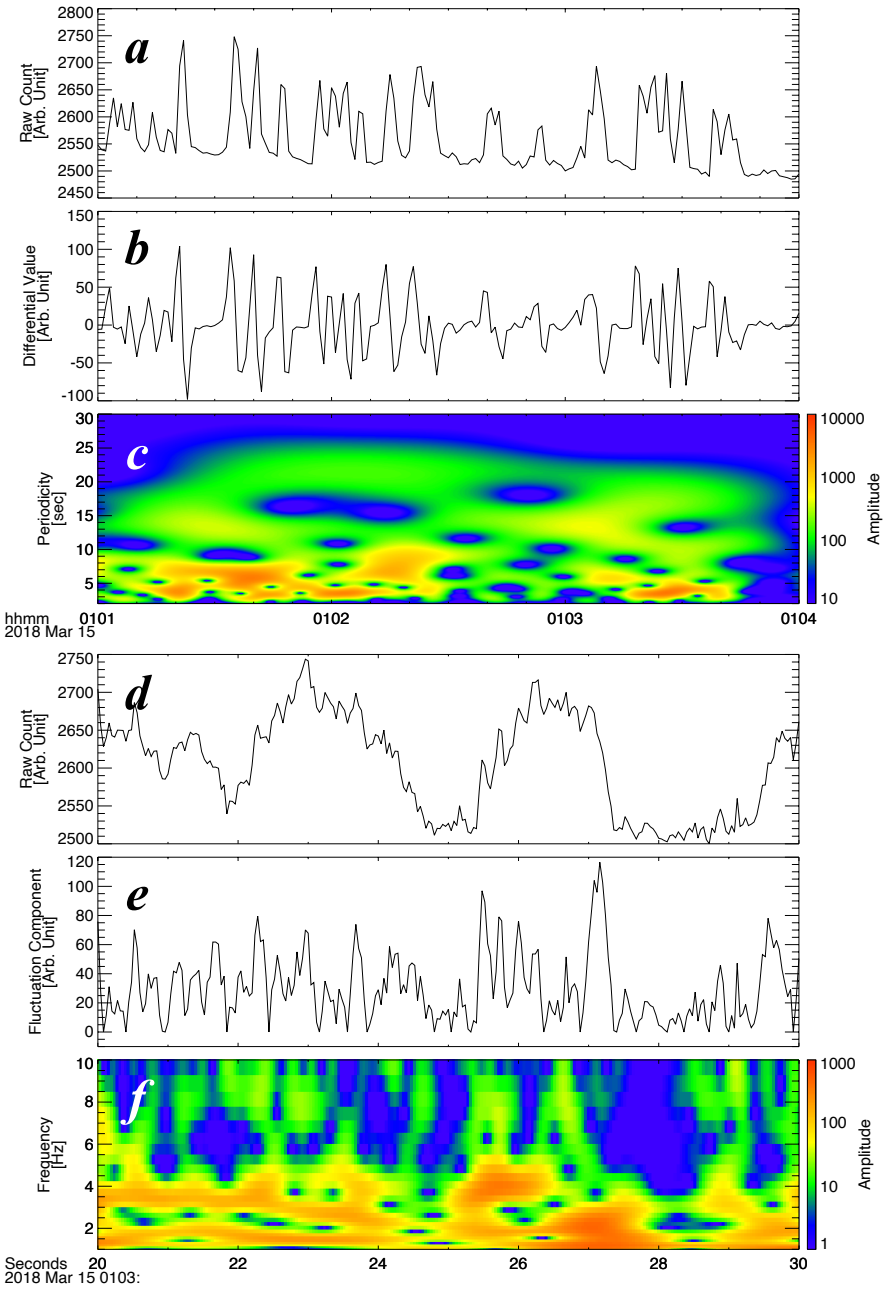

Figure 4.3: **a** Temporal variation of PsA observed by the EMCCD all-sky imager at Tjautjas during a 4 min interval from 01:01:00 to 01:04:00 UT on March 15, 2018. **b** Time derivative of the original time series in **a**. **c** Period–time diagram obtained by applying the S-transformation to the time-derivative time series in **b**. **d** Magnified view of the time series in **a** during a 10 s interval from 01:03:20 to 01:03:30 UT. **e** Component of the internal modulation obtained by subtracting the background trend of the main pulsation. **f** Frequency–time diagram obtained by applying the wavelet transform to the fluctuating component data in **e**.

4.4 Results

4.4.1 Distribution of multiple temporal variations of PsA

To confirm that the hierarchical temporal variations of PsA were selected by the described procedure, we checked the distributions of the main pulsation and internal modulation. Figure 4.4a and 4.4b show histograms of the period/frequency of the main pulsation and internal modulation, respectively. The vertical axis shows the number of events, which was self-normalized, and the horizontal axis shows the period of the main pulsation (left) and the frequency of the internal modulation (right). In Figure 4.4a, most of the main pulsation is distributed between 4 and 8 s, and a few samples appear at periods longer than 10 s. *Yamamoto* (1988) demonstrated that the average repetition period of the main pulsation was 20.7 ± 5.4 s using an all-sky TV imager at La Ronge (64.6° MLAT), Canada. The period derived by *Yamamoto* (1988) is clearly longer than that in our result. However, *Duncan et al.* (1981) derived the distribution of the period of the main pulsation using photometers at four stations in Canada: Saskatoon (61.3° MLAT), La Ronge (64.6° MLAT), Southend (66.0° MLAT), and Rabbit Lake (67.8° MLAT). They concluded that the dominant period of the main pulsation ranges from 5 to 10 s, which is in good agreement with our distribution of the main pulsation period. Thus, the main pulsation with a longer period reported by *Yamamoto* (1988) represents one of the classes (probably an exceptional case) of PsA.

As shown in Figure 4.4b, the internal modulation ranges from 1.5 to 4.0 Hz, which is consistent with the 3 ± 1 Hz modulation (*Royrvik and Davis*, 1977). Most of the internal modulation is concentrated around 2.5 Hz. *Nishiyama et al.* (2014) statistically analyzed the frequency of the internal modulation using an EMCCD all-sky imager at Poker Flat, Alaska and found that it ranged from 1.5 to 3.5 Hz, which is consistent with our result. In contrast, some previous studies reported that the chorus elements, which have been considered to be the magnetospheric counterpart of the internal modulation, often vary more rapidly than the quasi 3 Hz internal modulation of PsA. For example, *Tracktehngerts et al.* (2014) statistically demonstrated that the repetition frequency of the chorus elements had a wide range, from a few Hz to several tens of Hz. In addition, *Miyoshi et al.* (2010) investigated the time series of the energy flux of PsA electrons from the REIMEI satellite and reported that the energy fluxes of 1.1 and 8.6 keV electrons

fluctuate with a frequency of up to ∼10 Hz, which is well beyond the internal modulation at ∼3 Hz.

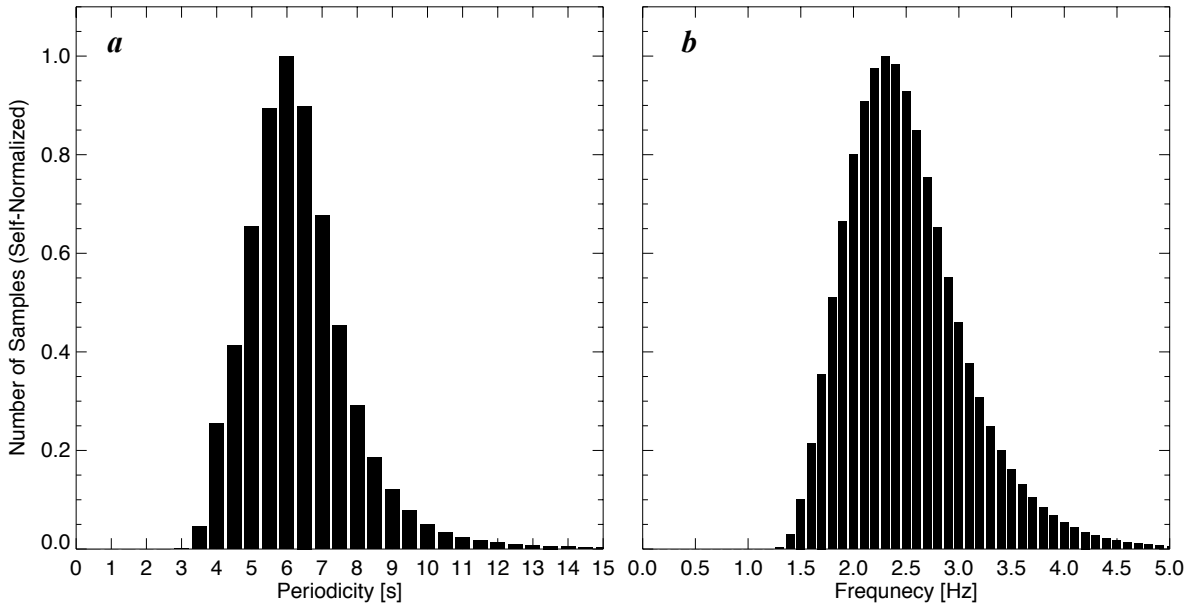

Figure 4.4: Distributions of **a** period of main pulsation and **b** frequency of internal modulation during the 1 h interval analyzed in this study.

As shown in Chapter 3, the PsA electrons are not mono-energetic but have an energy range from a few keVs to a few tens of keVs. For instance, *Sandahl et al.* (1980) showed, using in-situ data from a sounding rocket, that the energy of PsA electrons ranges from 5 to 40 keV. Therefore, the hierarchical temporal variations of PsA should be characterized by the combined effects of the temporal variations of all the precipitating electrons in those energy bands. The time required for precipitating electrons to travel from the magnetosphere to the ionosphere depends on their energy; thus, the travel time of PsA electrons varies. This effect may smear the faster variation of the chorus elements. In fact, *Nishiyama et al.* (2014) mentioned this possibility but did not further investigate how the variation in the travel time affects the frequency of the internal modulation. In the Discussion section, we will consider how this effect can smear the faster variation of the chorus elements and ultimately control the existence of the internal modulation.

4.4.2 Proportion of the internal modulation

By using the main pulsations and internal modulations detected by the procedure described earlier, we classified all the PsA samples into two categories: PsA with and without internal modulation. Specifically, if at least one internal modulation was detected in the pixel where the main pulsation was detected, we regarded the sample as a PsA with internal modulation. Samples that did not meet this criterion were classified as PsA without internal modulation. This classification process was applied to all the pixels of the four EMCCD all-sky imagers and enabled us to derive the spatial distributions of PsA with/without internal modulation. Figure 4.5a shows a snapshot of the spatial distribution of PsA with/without internal modulation at 01:00:00 UT on March 15, 2018, where the red (blue) dots indicate PsA with (without) internal modulation. At least in this time interval, most of the PsAs within the combined FOV were not accompanied by internal modulation. Interestingly, however, there were clusters of PsAs showing internal modulation in the lower-latitude portion of the combined FOV, which suggests that the presence/absence of internal modulation might exhibit a latitudinal dependence.

We calculated the proportion (i.e., percentage) of PsAs with internal modulation for all the PsA samples in the 1 h interval. The average occurrence rate of PsAs with internal modulation was approximately 43% of the total cases, which is consistent with the snapshot shown in Figure 4.5a. This finding indicates that PsAs are not always accompanied by internal modulation. Figure 4.5b shows the latitudinal dependence of the percentage of PsAs with internal modulation for geographic latitudes of 65° to 72°. The percentage tends to decrease as the latitude increases. This result implies that, as suggested by Figure 4.5a, the presence of internal modulation depends on the latitude. In the Discussion section, we consider the reason for this latitudinal dependence.

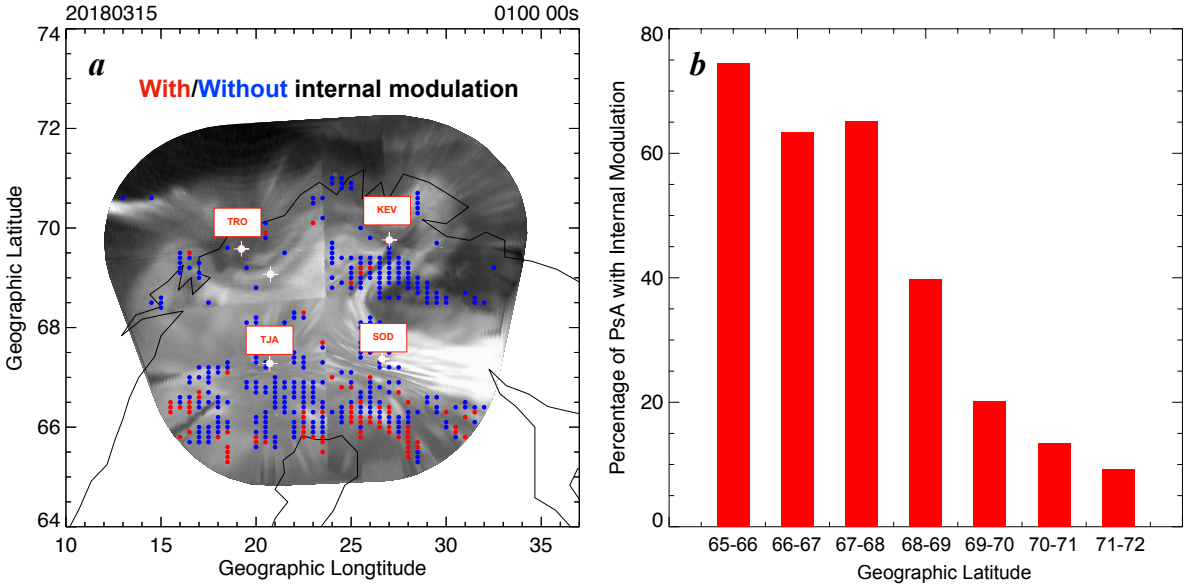

Figure 4.5: **a** Spatial distribution of PsAs with/without internal modulation at 01:00:00 UT on March 15, 2018. The red and blue dots indicate PsAs with/without internal modulation, respectively. **b** Latitudinal dependence of the percentage of PsAs with internal modulation.

4.5 Discussion

First, we discuss why the frequency of internal modulation of PsA is generally 3 ± 1 Hz, whereas the chorus elements and corresponding flux changes of precipitating electrons vary considerably more rapidly. As briefly mentioned in the previous section, a possible explanation is the variation in the time of flight (TOF) of precipitating PsA electrons; we speculate that the variation in TOF may introduce a difference between the frequency of the internal modulation and the repetition period of chorus elements, which was first noted by *Nishiyama et al.* (2014).

To prove this hypothesis, we simulated how the variation in TOF affects the time series of the optical intensity, including the internal modulation, observed from the ground (i.e., the way that faster variations can be smeared by the variation in TOF) by following the TOF simulation proposed by *Miyoshi et al.* (2010). Figure 4.6 shows a schematic diagram of the TOF simulation model taken from *Miyoshi et al.* (2010). *Miyoshi et al.* (2010) considered not only the TOF of electrons in terms of wave-particle interaction in

the ionosphere but also the time needed for chorus waves to propagate along a field line from the magnetic equator to the point of resonance. Thus, we estimated the total time delay from the generation of the chorus at the magnetic equator to the arrival of scattered electrons at ionospheric altitudes.

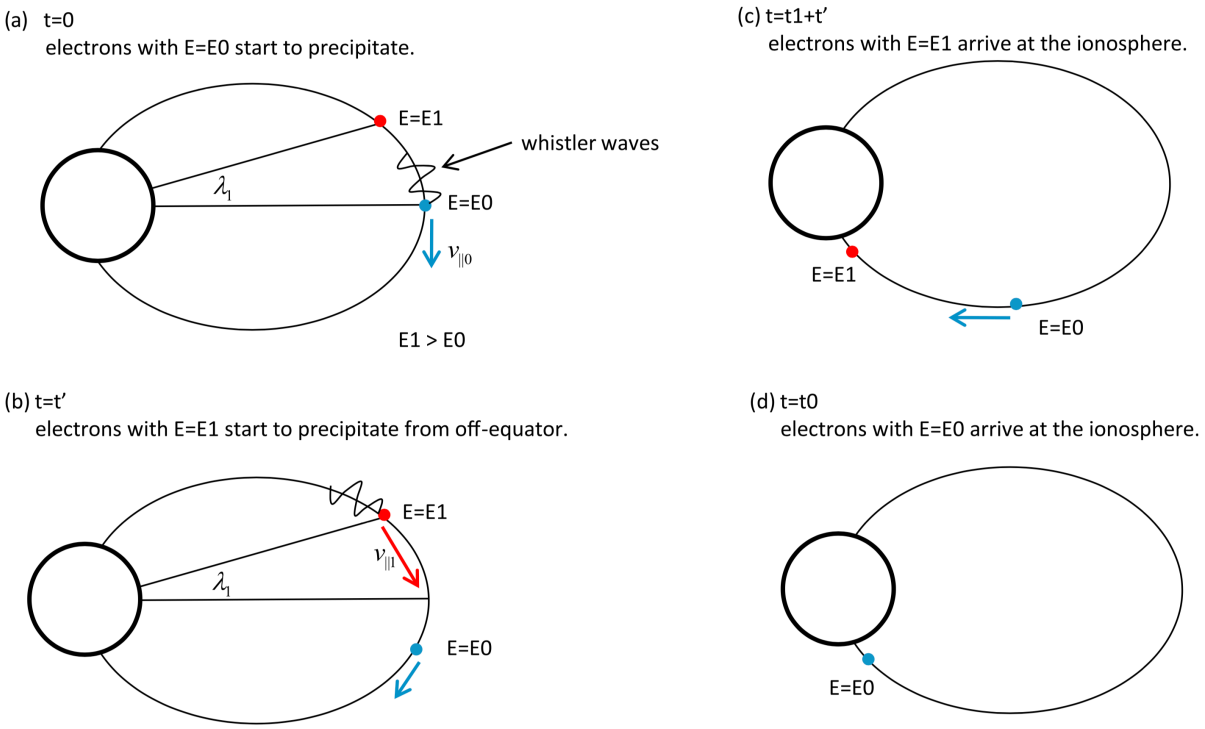

Figure 4.6: Schematic diagram of TOF simulation from *Miyoshi et al.* (2010).

For simplicity, we assumed that the propagation of chorus waves is perfectly parallel to the magnetic field. First, using the ambient magnetic field intensity B calculated using the Tsyganenko 04 magnetic field model (*Tsyganenko and Sitnov*, 2005), we estimated the resonance energy of electrons in first-order cyclotron resonant scattering with the chorus wave (*Kennel and Petschek*, 1966):

$$E_R = \frac{B^2}{2\mu_0 N}\frac{f_{ce}}{f}(1-\frac{f}{f_{ce}})^3 \tag{4.1}$$

where B is the ambient magnetic field intensity, μ_0 is the permeability of vacuum, N is the thermal plasma density [which is assumed to be 2.8 cm^{-3} on the basis of an empirical model (*Carpenter and Anderson*, 1992)], f_{ce} is the cyclotron frequency, and f is the chorus wave frequency. As the chorus wave propagates to higher latitudes along the field line, the resonance energy increases because B is stronger in regions closer to Earth (*Miyoshi et*

al., 2015). Lower-energy electrons are scattered near the magnetic equator, whereas more energetic electrons are scattered at higher latitudes. In this case, the travel distance from the region of wave-particle interaction to the ionosphere increases because the interaction occurs in the opposite hemisphere. We also need to consider the time required for the chorus waves to propagate from the magnetic equator to the resonance scattering region. Thus, both the location and timing of resonance scattering are determined by the electron energy; thus, the dependence of the travel distance and precipitation start time on the electron energy are slightly complicated.

Considering an electron with energy E that resonates with the chorus at magnetic latitude λ, the total delay time from the generation of the chorus at the magnetic equator to the arrival of scattered electrons at the ionosphere, τ, can be expressed as follows:

$$\tau = t_E + t_W \tag{4.2}$$

where t_E is the travel time of electrons with energy E from magnetic latitude λ (i.e., the resonance scattering region) to the ionosphere, and t_W is the time required for the chorus wave to propagate from the magnetic equator to magnetic latitude λ. When we estimated t_W, we used the group velocity of the chorus in the parallel direction calculated by the following equation (*Ozaki et al.*, 2019):

$$v_g = 2c\frac{f^{\frac{1}{2}}(f_{ce}\cos\theta_{\kappa B} - f)^{\frac{3}{2}}}{f_p f_{ce}\cos\theta_{\kappa B}} \tag{4.3}$$

where c is the speed of light, f_p is the plasma frequency, and $\theta_{\kappa B}$ is the wave normal angle to the magnetic field line. Note that we assumed that chorus waves propagate up to 20° of magnetic latitude. We estimated the delay time τ for three L values (L = 5, 6, and 7). Figure 4.7 shows τ for electron energies of 5 to 30 keV. The colors indicate the chorus wave frequency normalized by f_{ce}. Importantly, there is a time difference of approximately 0.5 s between the 5 and 30 keV electrons even at $L = 5.0$, and the variation in τ with energy becomes larger with increasing L. This result suggests that the variation in τ smears the contribution of the faster variations of the chorus elements to the subsecond temporal variations of PsA.

To demonstrate the smearing process in detail, we reproduced a time series of the temporal variation of PsA as observed from the ground from an input fundamental waveform. During this reproduction process, we considered the values of τ for various electron energies. Before presenting the results, we introduce the methodology for reproducing

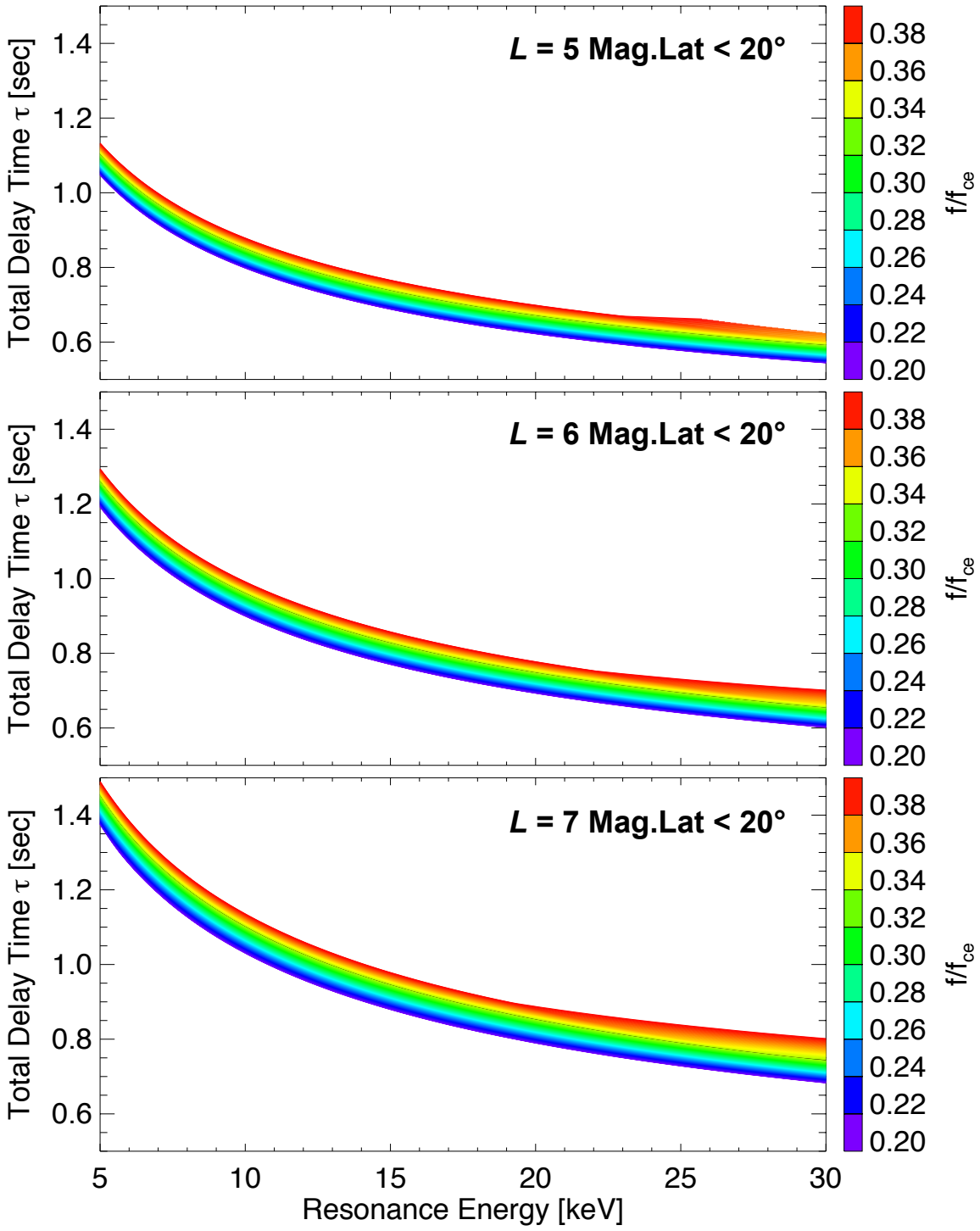

Figure 4.7: Variation of τ with electron energy between 5 and 30 keV for three L values (L = 5, 6, and 7). Colors indicate the chorus frequency f normalized by the electron gyrofrequency f_{ce}.

the temporal variation of PsA. Figure 4.8a shows the fundamental test wave forms, which reveal that there is no delay time as input whose modulation frequency is 3 Hz. When we reproduced the time series of PsA emission, we began by generating multiple time series representing the energy flux of electrons with various energies. We estimated the delay time τ for each electron energy and shifted each time series accordingly. Then, we generated the time series of the PsA emission by blending multiple time series for different τ, where the blending was weighted by considering the energy spectrum of PsA electrons in *Sandahl et al.* (1980). By integrating multiple time series for different τ, which is the smearing process that we are interested in, we reproduced the hierarchical temporal variations of PsA that should be observed as prompt emission of auroral light (e.g., at 427.8 nm). Figure 4.8b shows the reproduced time series of the PsA luminosity calculated by this procedure. The increases in auroral intensity in Figure 4.8b correspond to the ON phase of the main pulsation, and the fine-scale spiky structures superimposed on the main pulsation are the signatures of the internal modulation. The signatures of the 3 Hz modulation in the original time series (Figure 4.8a) are still recognizable in Figure 4.8b, although the amplitude of the peaks is decreased by smearing. This result indicates that the 3 Hz modulation of the input fundamental waveform can survive the smearing process and can be identified as the internal modulation of PsA observed from the ground. We applied the wavelet transform to these time series using the same procedure as that in the frequency analysis of actual optical data. Figure 4.8c shows the frequency–time diagrams. Frequency bands showing a larger wavelet amplitude appear at 3 Hz.

The latitudinal distribution of the wavelet amplitude at each geographic latitude was obtained by performing the earlier procedure for various input frequencies ranging from 2 to 10 Hz at 1 Hz intervals. The results are presented in Figure 4.9. The vertical and horizontal axes represent the geographic latitude and frequency of the input waveform, respectively, and the colors indicate the wavelet amplitude. Figure 4.9 shows that the amplitude decreases as the input frequency increases. Specifically, at frequencies above 6 Hz, the wavelet amplitude is remarkably small, indicating that the internal modulation is well smeared by the variation in τ. However, even around 5 Hz, where little internal modulation was observed, the wavelet amplitude was large. The reason may be the contribution of electrons with energies below 5 keV, although we assumed that the electrons contributing to PsA emission have an energy range of 5–30 keV in the simulations. For PsA electrons with energies below 5 keV, the variation in τ would be even larger, and

thus, a more significant smearing effect is expected. In addition, the energy flux (or energy spectrum) of the electrons in the simulation may differ from the observations. However, it is important to note that higher-frequency variations tend to be smeared more effectively by the variation in τ, which prevents rapid variation in the internal modulation with time.

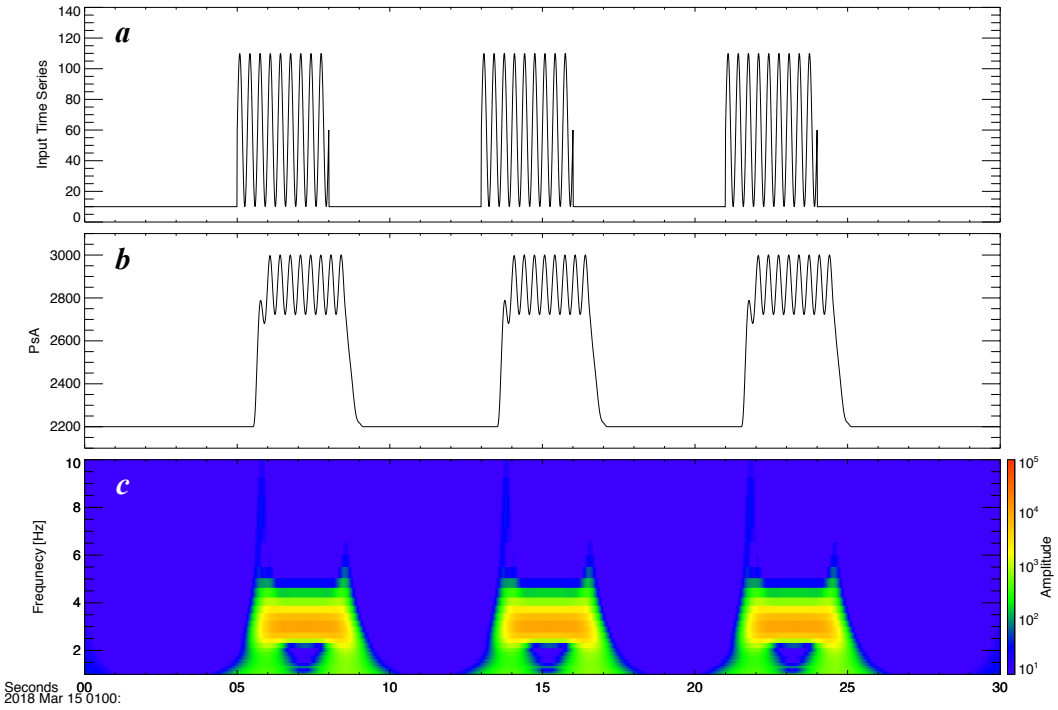

Figure 4.8: **a** Fundamental (input) time series with a modulation frequency of 3 Hz at a geographic latitude of 68.5°. **b** Time series of PsA emission reproduced considering the variation effect. **c** Frequency–time diagrams of the reproduced time series shown in **b**.

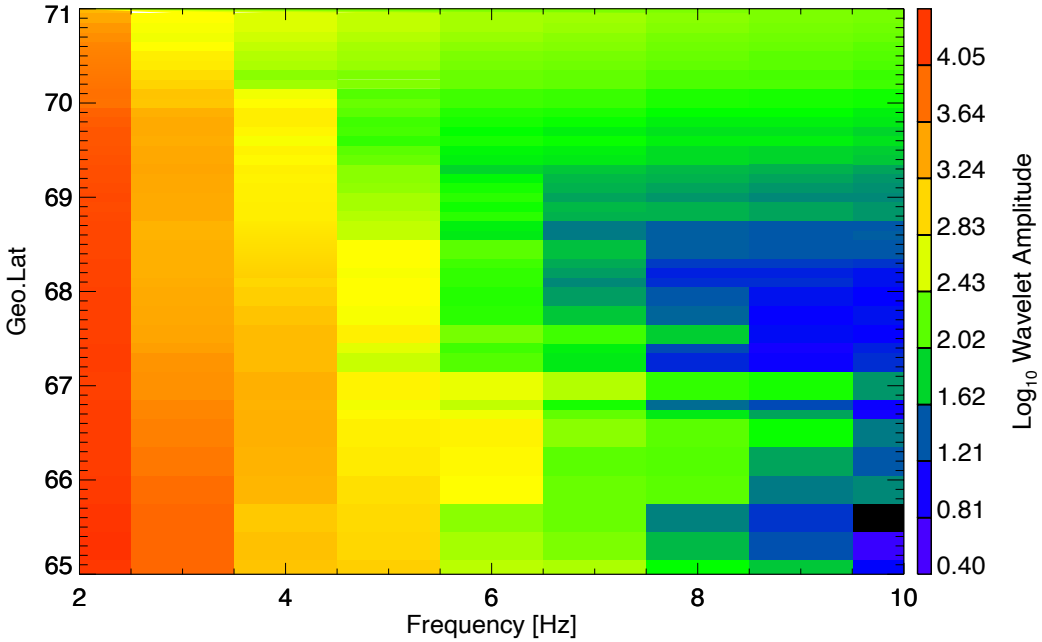

Figure 4.9: Latitudinal distribution of the wavelet amplitude of the internal modulation.

Here, we discuss the reason that PsA with internal modulation is more frequently observed at low latitudes. At high latitudes, the variation in τ increases (as shown in Figure 4.7) because PsA electrons must travel farther at larger L values. Therefore, PsA without internal modulation is likely to be observed more frequently at lower latitudes. This dependence is also illustrated in Figure 4.9, where the wavelet amplitude decreases at higher latitudes for each frequency of the input waveform. To evaluate the effect of this latitudinal change in the variation in τ on the amplitude of the internal modulation, we also reproduced the time series of PsA for a geographical latitude of 66° and a geographical longitude of 70°. Figure 4.10a shows the test waveform of a chorus wave with a modulation frequency of 3 Hz. Figure 4.10b and 4.10c show the reproduced time series of PsA emission at geographical latitudes of 66° and 70°, respectively. In both the cases, the reproduced time series shows hierarchical temporal variations (i.e., the internal modulation superimposed on the main pulsation). However, the amplitude of the internal modulation at a geographical latitude of 70° is smaller than that at a geographical latitude of 66°. As the geographic latitude increases (i.e., at larger L values), the electrons follow a longer path to travel from the magnetosphere to the ionosphere. Therefore, the effect of the variation in τ (i.e., the smearing effect) is more significant at higher geographic lati-

tudes than at lower latitudes. This result is consistent with the latitudinal dependence of PsA without internal modulations, which is more frequently observed at lower latitudes.

Recent studies have reported that the energy of PsA electrons depends on MLT and tends to be higher on the morning side (*Hosokawa and Ogawa*, 2015; *Kawamura et al.*, 2020). As shown in Figure 4.7, the variation in τ decreases as the energy of the precipitating electrons increases. For example, if the bulk energy of a PsA is carried by 15–30 keV electrons, the variation is only approximately 0.1 s, which may allow the PsA to respond to more rapid variation in the chorus elements. This result suggests that PsAs with internal modulation can be observed more frequently on the later morning side. Next, the dependence of PsAs with internal modulation on MLT needs to be examined.

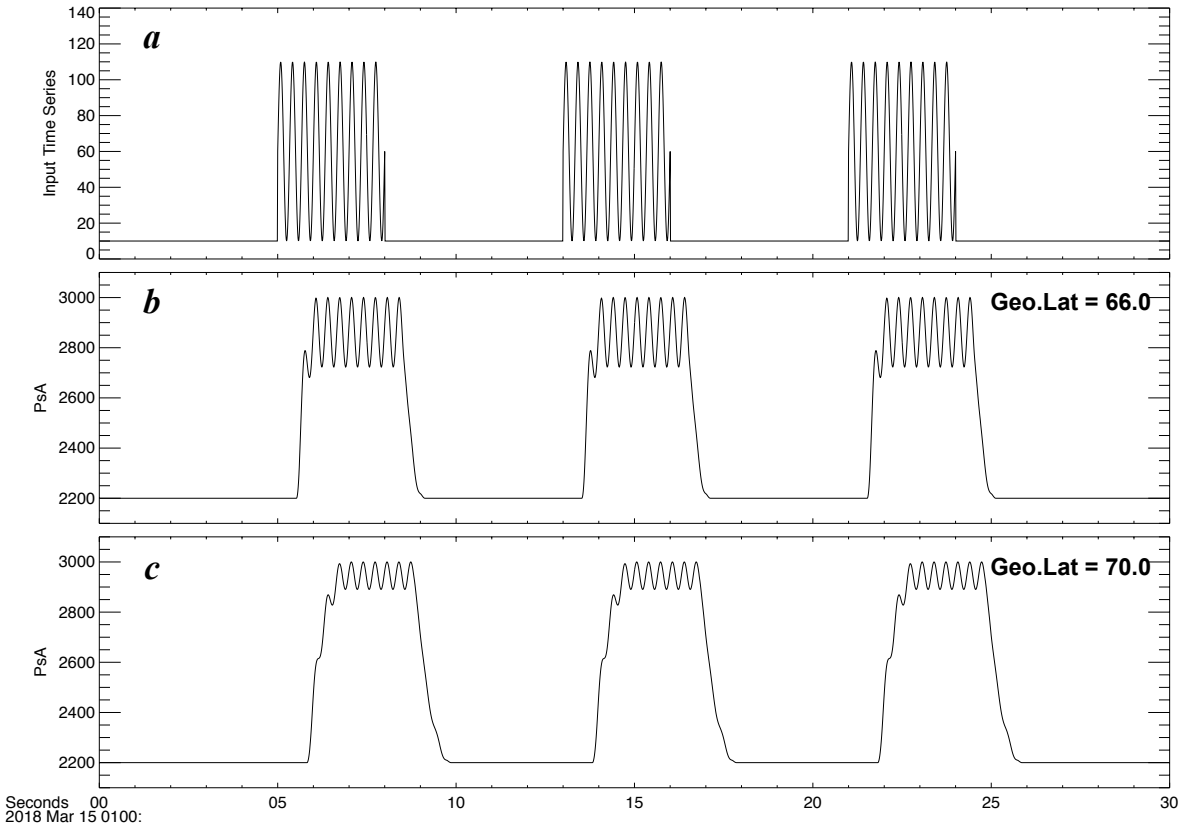

Figure 4.10: **a** Fundamental (input) time series with a modulation frequency of 3 Hz. **b**, **c** Reproduced time series of PsA emission at geographical latitudes of 66° (**b**) and 70° (**c**).

4.6 Conclusions

The characteristics of the internal modulation of PsA were investigated using data from EMCCD imagers at four locations in northern Scandinavia with simultaneous observations by the Arase satellite. Specifically, we investigated a PsA that was observed simultaneously by all four EMCCD all-sky imagers during a 1 h interval. The combination of data from four high-speed (100 Hz sampling) imagers and a simple numerical simulation yielded the following results:

1. We detected multiple temporal variations of PsA (i.e., the main pulsation and internal modulations) and derived their period/frequency distributions. The period of the main pulsation is typically 4–8 s, whereas the frequency of the internal modulations was 2–3 Hz. These characteristics are fairly consistent with previous studies of the periods of PsA, which confirms the accuracy of the frequency analyses employed in this study.

2. Not all the PsAs were accompanied by the ∼3 Hz subsecond modulation. In these results, the average occurrence rate of PsAs with 3 Hz internal modulation is 43% of the total. It was also found that the proportion (percentage) of PsAs with internal modulation was higher at lower latitudes. The internal modulation is less frequent at larger L values.

3. To determine the factors controlling the presence/absence of internal modulation, we simulated the effect of the variation in delay time from the generation of the chorus to the arrival of electrons at the ionosphere. The simple simulation suggested that the effect of this variation (i.e., the smearing process) eliminates the faster variation in the original time series of the chorus, and more rapid variations (faster than 5 Hz, say) cannot be identified in the time series of PsA emission.

4. The observed latitudinal dependence of the presence/absence of internal modulation can also be explained by the smearing process because the travel time from the point of resonance scattering in the magnetosphere to the ionosphere is longer for larger L values (i.e., at higher latitudes). At higher latitudes, the smearing process is more effective; thus, the 3 Hz internal modulation sometimes cannot survive the trip from the magnetosphere to the ionosphere.

The temporal variation in the chorus, especially the discreteness of the chorus elements, is one of the most important factors controlling the temporal variation of PsA. The results of this study, however, suggest that the difference in the travel time of electrons having different energies and the propagation of chorus waves from the magnetic equator to the point of resonance scattering also play a significant role in characterizing the temporal variation of PsA as observed from the ground. In addition, the presence/absence of internal modulation may provide additional information about the energy of the precipitating electrons causing a PsA.

Chapter 5

Concluding remarks

5.1 Summary and conclusions

In the work reported herein, we investigated the fundamental characteristics of PsAs (specifically, the formation mechanism of the hierarchical temporal variations) using high-speed optical observations. To reproduce the hierarchical temporal variations of PsA, the delay time of the PsA electrons must be considered, in addition to the time series of the chorus waves (*Miyoshi et al.*, 2010; *Nishiyama et al.*, 2014). However, the energy of the PsA electrons and its MLT dependence have not yet been analyzed statistically. Therefore, the effect of the characteristics of the PsA electrons on the development of the hierarchical temporal variations of PsA is unclear. In this work, we first derived the energy of PsA electrons and their MLT variation statistically. Then, we calculated the delay times of PsA electrons in the obtained energy ranges of PsA electrons and evaluated their effects on the hierarchical temporal variations of PsA. Several key results are summarized next.

In Chapter 3, we presented calculations of the lifetime of $O(^1S)$ obtained by a cross-correlation analysis of the time series of the emissions at 427.8 and 557.7 nm obtained by a five-wavelength photometer in Norway. Using the method proposed by *Scourfield et al.* (1981), we statistically estimated the distribution of the emission altitude of PsA. The emission altitude of PsA generally ranges from 95 to 115 km, and the energies of the precipitating electrons range from 5 to 30 keV. In addition, the emission altitude of PsA decreases toward the morning side, which indicates that the energy of PsA electrons tends to be higher in the later MLT sector. However, by simple calculations of the resonance energy of the chorus waves, we found that this tendency (harder PsA electrons on the

morning side) cannot be explained only by the effects of MLT on ambient parameters such as the magnetic field intensity and density of cold plasma. Therefore, when discussing the energy of PsA electrons, it is necessary to consider not only the ambient parameters but also the propagation characteristics of chorus waves along the magnetic field.

In Chapter 4, to determine the factors controlling the hierarchical periodic structure of PsA, we investigated the proportion of PsAs with internal modulation and their spatial distribution. An intense PsA was observed by four EMCCD all-sky imagers in Scandinavia on March 15, 2018, from 00:30 to 01:30 UT. By performing frequency analysis of the optical time series obtained during that interval, we demonstrated that 43% of all the PsA cases showed subsecond internal modulation and that the typical frequency of the internal modulation was approximately 3 Hz. However, the frequency of the chorus elements, which are considered to be the counterpart of the internal modulation, is widely distributed from a few Hz to several tens of Hz. We also derived the spatial distribution of PsAs with internal modulation and found that they were more frequently observed at lower latitudes. These results suggest that a certain process is smearing the fast variation of the chorus elements. We performed simple numerical simulations considering the time delay of chorus wave propagation and the TOF of PsA electrons whose energy range is estimated in Chapter 3. On the basis of the results, we suggest that, in addition to fine-scale structure in the chorus intensity, the variation in the travel time of PsA electrons from the magnetosphere to the ionosphere and the propagation of chorus waves play an important role in determining the hierarchical temporal variations of PsA (i.e., the presence/absence of $\sim$3 Hz internal modulation).

The results presented in Chapters 3 and 4 demonstrate that the energy of PsA electrons is approximately 5–30 keV and that the hierarchical temporal variations of PsA result from the variation in the delay time of these electrons and the discreteness of the chorus elements. Because the variation in the delay time depends on the energy of PsA electrons, its effect is expected to be less significant (i.e., the internal modulation is expected to be clearer) in PsAs caused by higher-energy electrons. Thus, we conclude that the range of electron energies plays a significant role in characterizing the hierarchical temporal variations of PsA. This finding further implies that the discreteness (i.e., visibility) of the internal modulation can be used as an indicator of the energy of the precipitating electrons causing a PsA.

5.2 Future work

In Chapter 3, we showed that the energy of PsA electrons tends to be higher toward the morning side. In addition, as discussed in the previous section, as the energy bands of PsA electrons become higher, the variation in the delay time becomes smaller. Then, the internal modulation becomes more evident. This suggests that PsAs with internal modulation can be expected to be more frequently observed on the morning side. Therefore, it is necessary to compare the effect of MLT on the presence/absence of internal modulation with that of the energies of PsA electrons.

In Chapter 4, we derived the spatial distribution of the hierarchical temporal variation using an example with a duration of 1 h. Therefore, it is necessary to statistically analyze the presence/absence of internal modulation using many datasets.

The method of estimating the emission altitude of PsA presented in Chapter 3 can also be applied to all-sky imager observations (e.g., by pointing the imagers observing at 427.8 and 557.7 nm in the same direction). This method enables us to estimate the emission altitude of PsA in two dimensions rather than at a single point within the FOV. Using this technique, we can estimate the relationship between the shape of a PsA and the energy of the precipitating electrons (i.e., where and how the electrons resonate with chorus waves).

The shape and propagation direction of PsA are very complex; therefore, it is difficult to analyze them visually using a large amount of data. However, the automated detection method described in Chapter 4 can be used to verify the relationship between the shape of PsA and its direction of propagation and hierarchical temporal variation. In particular, the shape of PsA is thought to reflect the spatial extent of the source of the chorus waves, which is a key parameter for gaining a better understanding of the unsolved problem of wave-particle interaction.

Publications

Publications Related to the Thesis

- Kawamura, Y., K. Hosokawa, S. Nozawa, Y. Ogawa, T. Kawabata, S.-i. Oyama, Y. Miyoshi, S. Kurita, and R. Fujii (2020), Estimation of the emission altitude of pulsating aurora using the five-wavelength photometer, *Earth, Planets Space 72*, 96, https://doi.org/10.1186/s40623-020-01229-8 (The content of Chapter 3)

International Conferences

- Kawamura, Y., K. Hosokawa, S.-i. Oyama, Y. Miyoshi, Y. Ogawa, S. Kurita, and R. Fuji, Spatial distribution of multiple temporal variations of pulsating aurora: multi-point high-speed optical observations in Scandinavia, Physics of Auroral Phenomena 43rd Apatity Seminar, Apatity, Mar 10, 2020

- Kawamura, Y., K. Hosokawa, S.-i. Oyama, Y. Miyoshi, Y. Ogawa, S. Kurita, and R. Fuji, Multiple temporal variations of pulsating aurora: multi-point high-speed optical observations in Scandinavia, American Geophysical Union Fall Meeting, San Francisco, Dec 13, 2019

- Kawamura, Y., K. Hosokawa, S. Nozawa, Y. Ogawa, T. Kawabata, and R. Fuji, The MLT dependence on the emission altitude of pulsating aurora, URSI-Japan Radio Science Meeting, The University of Electro-Communications, Sep 5, 2019

- Kawamura, Y., K. Hosokawa, Y. Ogawa, S. Kurita, J. Wygant, A. Brenneman, J. Bonnell, and D. Hartley, Relationship between pulsating aurora and repetitive bursts of magnetospheric chorus: a statistical analysis, American Geophysical Union Fall Meeting, Washington DC, USA, Dec 13, 2018

- Kawamura, Y., K. Hosokawa, Y. Ogawa, S. Kurita, J. Wygant, A. Brenneman, J. Bonnell, and C. Kletzing, Periodicity of PsA main pulsation and bursts of chorus: A statistical comparison, AOGS 2018, Honolulu, June 5, 2018

- Kawamura, Y., K. Hosokawa, Y. Ogawa, S. Kurita, J. Wygant, A. Brenneman, J. Bonnell, and C. Kletzing, Periodicity of PsA main pulsation and bursts of chorus: A statistical comparison, ISAR-5, Tokyo, Jan 5, 2018

References

[1] Adachi, K., S. Nozawa, Y. Ogawa, A. Brekke, C. Hall, and R. Fujii (2017), Evaluation of a method to derive ionospheric conductivities using two auroral emissions (428 and 630 nm) measured with a photometer at Tromso (69.6∘N), *Earth, Planets Space, 69*, 90, https://doi.org/10.1186/s40623-017-0677-4

[2] Akasofu, S.-I. (1964), The development of the auroral substorm, *Planet. Space Sci., 12*, 4, 273–282, doi:10.1016/0032-0633(64)90151-5

[3] Baumjohann, W., and R. A. Treumann (1997), *Basic Space Plasma Physics*, Imperial College Press, London

[4] Brekke, A., and K. Henriksen (1972), The intensity ratio I(5577)/I(4278) and the effective lifetime of O(1S) atoms in pulsating aurora, *Planet. Space Sci., 20*, 53–60, https://doi.org/10.1016/0032-0633(72)90140-7

[5] Brown, N. B., T. N. Davis, T. J. Hallinan, and H. C. Stenbaek-Nilsen (1976), Altitude of pulsating aurora determined by a new instrumental technique, *Geophys. Res. Lett., 7*, 403-404, https://doi.org/10.1029/GL003i007p00403

[6] Carpenter, D. L., and R. R. Anderson (1992), An ISEE/whistler mode of equatorial electron density in the magnetosphere, *J. Geophys. Res.: Space Phys., 97*, 1097–1108, doi:10.1029/91JA01548

[7] Coroniti, F. V., and C. F. Kennel (1970), Electron precipitation pulsations, *J. Geophys. Res., 75*, 7, 1279–1289

[8] Davidson, G. T. (1979), Self-modulated VLF wave-electron interactions in the magnetosphere: A cause of auroral pulsations, *J. Geophys. Res.: Space Phys., 84*, 6517–6523

[9] Davidson, G. T. (1990), Pitch-angle diffusion and the origin of temporal and spatial structures in morningside aurorae, *Space Sci. Rev., 53*, 45–82, https://doi.org/10.1007/BF00217428

[10] Demekhov, A. G., and V. Y. Trakhtengerts (1994), A mechanism of formation of pulsating aurorae, *J. Geophys. Res.: Space Phys., 99*, 5831–5841

[11] Duncan, C. N., F. Creutzberg, R. L. Gattinger, F. R. Harris, and A. Vallancejones (1981), Latitudinal and temporal characteristics of pulsating auroras, *Can. J. Phys., 59*, 1063–1069, https://doi.org/10.1139/p81-140

[12] Frank, L. A., and K. L. Ackerson (1971), Observations of charged particle precipitation into the auroral zone, *J. Geophys. Res., 76*, 3612

[13] Han, D. S., X. C. Chen, J. J. Liu, Q. Qiu, K. Keika, Z. J. Hu, J. M. Liu, H.-Q. Hu, and H.-G. Yang (2015), An extensive survey of dayside diffuse aurora based on optical observations at Yellow River Station, *J. Geophys. Res.: Space Phys., 120*, 9, 7447–7465, https://doi.org/10.1002/2015JA021699

[14] Hedin, A. E (1991), Extension of the MSIS thermosphere model into the middle and lower atmosphere, *J. Geophys. Res.: Space Phys., 96*, 1159–1172

[15] Hosokawa, K., and Y. Ogawa (2015), Ionospheric variation during pulsating aurora, *J. Geophys. Res.: Space Phys., 120*, 5943–5957, https://doi.org/10.1002/2015JA021401

[16] Hosokawa, K., Y. Miyoshi, M. Ozaki, S.-i. Oyama, Y. Ogawa, S. Kurita, Y. Kasahara, Y. Kasaba, S. Yagitani, S. Matsuda, F. Tsuchiya, A. Kumamoto, R. Kataoka, K. Shiokawa, T. Raita, E. Turunen, T. Takashima, I. Shinohara, and R. Fujii (2020a), Multiple time-scale beats in aurora: precise orchestration via magnetospheric chorus waves, *Sci. Rep., 10*, 3380, https://doi.org/10.1038/s41598-020-59642-8

[17] Hosokawa, K., S.-i. Oyama, Y. Ogawa, et al. (2020b), A ground-based instrument suite for integrated high-time resolution measurements of pulsating aurora with Arase, Submitted to *J. Geophys. Res.: Space Phys.*

[18] Hunten, D. M., and M. B. McElroy (1966), Quenching of metastable states of atomic and molecular oxygen and nitrogen, *Rev. Geophys., 4*, 303–328, https://doi.org/10.1029/RG004i003p00303

[19] Johnson, C. Y. (1966), Ionospheric comparison and density from 90 to 1200 kilometers at solar minimum, *J. Geophys. Res., 71*, 330

[20] Johnstone, A. D. (1983), The mechanism of pulsating aurora, *Ann. Geophys., 1*, 397–410

[21] Jones, S. L., M. R. Lessard, P. A. Fernandes, D. Lummerzheim, J. L. Semeter, C. J. Heinselman, K. A. Lynch, R. G. Michell, P. M. Kintner, H. C. Stenbaek-Nielsen, and K. Asamura (2009), PFISR and ROPA observations of pulsating aurora, *J. Atmos. Sol. Terr. Phys., 71*, 708–716, https://doi.org/10.1016/j.jastp.2008.10.004

[22] Jones, S. L., M. R. Lessard, K. Rychert, E. Spanswick, and E. Donovan (2011), Large scale aspects and temporal evolution of pulsating aurora, *J. Geophys. Res.: Space Phys., 116*, A03214, https://doi.org/10.1029/2010JA015840

[23] Kasahara, S., Y. Miyoshi, S. Yokota, T. Mitani, Y. Kasahara, S. Matsuda, A. Kumamoto, A. Matsuoka, Y. Kazama, H. U. Frey, V. Angelopoulos, S. Kurita, K. Keika, K. Seki, and I. Shinohara (2018), Pulsating aurora from electron scattering by chorus waves, *Nature, 554*, 337–340, https://doi.org/10.1038/nature25505

[24] Kataoka, R., Y. Miyoshi, D. Hampton, T. Ishii, and H. Kozako (2012), Pulsating aurora beyond the ultra-low-frequency range, *J. Geophys. Res.: Space Phys., 117*, A8, https://doi.org/10.1029/2012JA017987

[25] Kawamura, Y., K. Hosokawa, S. Kurita, S.-i. Oyama, Y. Miyoshi, Y. Kasahara, M. Ozaki, S. Matsuda, A. Matsuoka, B. Kozelov, Y. Kawamura, and I. Shinohara (2019), Tracking the region of high correlation between pulsating aurora and chorus: simultaneous observations with Arase satellite and ground-based all-sky imager in Russia, *J. Geophys. Res.: Space Phys., 124*, 2769–2778, https://doi.org/10.1029/2019JA026496

[26] Kawamura, Y., K. Hosokawa, S. Nozawa, Y. Ogawa, T. Kawabata, S.-i. Oyama, Y. Miyoshi, S. Kurita, and R. Fujii (2020), Estimation of the emission altitude of pulsating aurora using the five-wavelength photometer, *Earth, Planets Space, 72*, 96, https://doi.org/10.1186/s40623-020-01229-8

[27] Kennel, C. F., and H. E. Petschek (1966), Limit on stably trapped particle fluxes, *J. Geophys. Res., 71*, 1–28, https://doi.org/10.1029/JZ071i001p00001

[28] Lessard, M. (2012), A review of pulsating aurora, in Auroral Phenomenology and Magnetospheric Processes: Earth And Other Planets (eds. A. Keiling, E. Donovan, F. Bagenal, and T. Karlsson), *Geophysical Monograph Series, 197*, https://doi.org/10.1029/2011GM001187

[29] Li, W., J. Bortnik, R. M. Thorne, Y. Nishimura, V. Angelopoulos, and L. Chen (2011), Modulation of whistler mode chorus waves: 2. Role of density variations, *J. Geophys. Res.: Space Phys., 116*, A06206, https://doi.org/10.1029/2010JA016313

[30] Li, W., J. Bortnik, Y. Nishimura, R. M. Thorne, and V. Angelopoulos (2012), The origin of pulsating aurora: Modulated whistler mode chorus waves, in Auroral Phenomenology and Magnetospheric Processes: Earth And Other Planets (eds. A. Keiling, E. Donovan, F. Bagenal, and T. Karlsson), *Geophysical Monograph Series, 197*, https://doi.org/10.1029/2011GM001164

[31] Lin, C. S., and R. A. Hoffman (1982), Observations of inverted-V electron precipitation, *Space Sci. Rev., 33*, 415–457

[32] McEwen, D. J., and C. N. Duncan (1981), A campaign to study pulsating auroras, *Can. J. Phys., 59*, 1029–1033, https://doi.org/10.1139/p81-135

[33] Miyoshi, Y., Y. Katoh, T. Nishiyama, T. Sakanoi, K. Asamura, and M. Hirahara (2010), Time of flight analysis of pulsating aurora electrons, considering wave-particle interactions with propagating whistler mode waves, *J. Geophys. Res.: Space Phys., 115*, A10312 https://doi.org/10.1029/2009JA015127

[34] Miyoshi, Y., S. Oyama, S. Saito, S. Kurita, H. Fujiwara, R. Kataoka, Y. Ebihara, C. Kletzing, G. Reeves, O. Santolik, M. Clilverd, C. J. Rodger, E. Turunen, and F. Tsuchiya (2015a), Energetic electron precipitation associated with pulsating aurora: EISCAT and Van Allen Probe observations, *J. Geophys. Res.: Space Phys., 120*, 2754–2766, https://doi.org/10.1002/2014JA020690

[35] Miyoshi, Y., S. Saito, K. Seki, T. Nishiyama, R. Kataoka, K. Asamura, Y. Katoh, Y. Ebihara, T. Sakanoi, M. Hirahara, S.-i. Oyama, S. Kurita, and O. Santolik (2015b), Relation between energy spectra of pulsating aurora electrons and frequency spectra of whistler mode chorus waves, *J. Geophys. Res.: Space Phys., 120*, 7728–7736, https://doi.org/10.1002/2015JA021562

[36] Miyoshi, Y., T. Hori, M. Shoji, M. Teramoto, et al. (2018), The ERG Science Center, *Earth, Planets Space, 70*, 96, https://doi. org/10.1186/s40623-018-0867-8

[37] Motoba, T., Y. Ebihara, A. Kadokura, M. J. Engebretson, M. R. Lessard, A. T. Weatherwax, and A.J. Gerrard (2017), Fast-moving diffuse auroral patches: a new aspect of daytime Pc3 auroral pulsations, *J. Geophys. Res.: Space Phys., 122*, 1542–1554, https://doi.org/10.1002/2016JA023285

[38] Mozer, F. S., C. W. Carlson, R. B. Torbert, B. Parady, J. Yatteau, and M. C. Kelley (1977), Observations of paired electrostatic shocks in the polar magnetosphere, *Phys. Rev. Lett., 38*, 292

[39] Nakamura, R., and T. Oguti (1987), Drifts of auroral structures and magnetospheric electric fields, *J. Geophys. Res.: Space Phys. 92* (A10), 11241–11247. https://doi.org/10.1029/JA092iA10p11241

[40] Ni, B., R. M. Thorne, Y. Y. Shprits, and J. Bortnik (2008), Resonant scattering of plasma sheet electrons by whistler-mode chorus: contribution to diffuse auroral precipitation, *Geophys. Res. Lett., 35*, L11106, https:// doi.org/10.1029/2008GL034032

[41] Nishimura, Y., J. Bortnik, W. Li, R. M. Thorne, L. R. Lyons, V. Angelopoulos, S. B. Menda, J. W. Bonnell, O. Le Contel, C. Cully, R. Ergun, and U. Auster (2010), Identifying the driver of pulsating aurora, *Science, 330*, 81–84, https://doi.org/10.1126/science.1193186

[42] Nishimura, Y., J. Bortnik, W. Li, R. M. Thorne, L. Chen, L. R. Lyons, V. Angelopoulos, S. B. Mende, J. Bonnell, O. Le Contel, C. Cully, R. Ergun, and U. Auster (2011), Multievent study of the correlation between pulsating aurora and whistler mode chorus emissions, *J. Geophys. Res.: Space Phys. 116*, A11221, https://doi.org/10.1029/2011JA016876

[43] Nishiyama, T., T. Sakanoi, Y. Miyoshi, D. L. Hampton, Y. Katoh, R. Kataoka, and S. Okano (2014), Multiscale temporal variations of pulsating auroras: On-off pulsation and a few Hz modulation, *J. Geophys. Res.: Space Phys., 119*, 3514–3527, doi:10.1002/2014JA019818

[44] Nozawa, S., T. Kawabata, K. Hosokawa, Y. Ogawa, T. Tsuda, A. Mizuno, R. Fujii, and C. Hall (2018), A new five-wavelength photometer operated in Tromsø (69.6°N, 19.2°E), *Earth, Planets Space, 70*, 193, https://doi.org/10.1186/s40623-018-0962-x

[45] Oguti, T. (1975), Metamorphoses of aurora, *Mem. Nat' l Inst. Polar Res., Ser. A, 12*, 1–101

[46] Ozaki M., K. Shiokawa, Y. Miyoshi, K. Hosokawa, et al. (2018), Microscopic observations of pulsating aurora associated with chorus element structures: coordinated Arase satellite-PWING observations. *Geophys. Res. Lett., 45*, 12,125–12,134, https://doi.org/10.1029/2018GL079812

[47] Ozaki M., Y. Miyoshi, K. Shiokawa, K. Hosokawa, et al. (2019), Visualization of rapid electron precipitation via chorus element wave-particle interactions, *Nat. Commun., 10*, 257, doi:10.1038/s41467-018-07996-z

[48] Partamies, N., D. Whiter, A. Kadokura, K. Kauristie, H. Nesse Tyssøy, S. Massetti, P. Stauning, and T. Raita (2017), Occurrence and average behavior of pulsating aurora, *J. Geophys. Res.: Space Phys., 122*, 5606–5618, https://doi.org/10.1002/2017JA024039

[49] Rees, M. H. (1989), *Physics and Chemistry of the Upper Atmosphere*, Cambridge University Press, Cambridge, https://doi.org/10.1017/CBO9780511573118, 14, 15

[50] Rees, M. H., and R. G. Roble (1975), Observations and theory of the formation of stable auroral red arcs, *Rev. Geophys., 13*, 201, https://doi.org/10.1029/RG013i001p00201

[51] Royrvik, O., and T. N. Davis (1977), Pulsating aurora: local and global morphology, *J. Geophys. Res., 82*, 4720–4740, https://doi.org/10.1029/JA082i029p04720

[52] Samara, M., and R. G. Michell (2010), Ground-based observations of diffuse auroral frequencies in the context of whistler mode chorus, *J. Geophys. Res.: Space Phys., 115*, A00F18, https://doi.org/10.1029/2009JA014852

[53] Sandahl, I., L. Eliasson, and R. Lundin (1980), Rocket observations of precipitating electrons over a pulsating aurora, *Geophys. Res. Lett., 7*, 309–312, https://doi.org/10.1029/GL007i005p00309

[54] Santolik, O., D. A. Gurnett, J. S. Pickett, M. Parrot, and N. Cornilleau-Wehrlin (2003), Spatio-temporal structure of storm-time chorus, *J. Geophys. Res.: Space Phys., 108*, 1278, https://doi.org/10.1029/2002JA009791

[55] Sato, N., D. M. Wright, Y. Ebihara, M. Sato, Y. Murata, H. Doi, T. Saemundsson, S. E. Milan, M. Lester, and C. W. Carlson (2002), Direct comparison of pulsating aurora observed simultaneously by the FAST satellite and from the ground at Syowa, *Geophys. Res. Lett., 29*, 2041, https://doi.org/10.1029/2002GL015615

[56] Scourfield, M. W. J., N. I. Parsons, L. P. Dennis, and W. F. Innes (1971), Effective lifetime of O(^{1}S) in pulsating aurora, *J. Geophys. Res., 76*, 3692–3699, https://doi.org/10.1029/JA076i016p03692

[57] Sheeley, B. W., M. B. Moldwin, H. K. Rassoul, and R. R. Anderson (2001), An empirical plasmasphere and trough density model: CRRES observations, *J. Geophys. Res.: Space Phys., 106*, 25,631–25,641

[58] Thorne, R. M., B. Ni, X. Tao, R. B. Horne, and N. P. Meredith (2010), Scattering by chorus waves as the dominant cause of diffuse auroral precipitation, *Nature, 467*, 943–946, https://doi.org/10.1038/nature09467

[59] Torbert, R. B., and F. S. Mozer (1978), Electrostatic shocks as the source of discrete auroral arcs, *Geophys. Res. Lett., 5*, 135

[60] Trakhtengerts, V. Y., A. G. Demekhov, E. E. Titova, B. V. Kozelov, O. Santolik, D. Gurnett, and M. Parrot (2004), Interpretation of Cluster data on chorus emissions using the backward wave oscillator model, *Phys. Plasmas, 11*, 1345–1351

[61] Tsurutani, B. T., and E. J. Smith (1977), Two types of magnetospheric ELF chorus and their substorm dependences, *J. Geophys. Res., 82*, 5112–5128

[62] Tsyganenko, N. A. (1989), A magnetospheric magnetic field model with a warped tail current sheet, *Planet. Space Sci., 37*, 5–20, https://doi.org/10.1016/0032-0633(89)90066-4

[63] Tsyganenko, N. A., and M. I. Sitnov (2005), Modeling the dynamics of the inner magnetosphere during strong geomagnetic storms, *J. Geophys. Res.: Space Phys., 110*, A03208, https://doi.org/10.1029/2004JA010798

[64] Turunen, E., P. T. Verronen, A. Seppälä, C. J. Rodger, M. A. Clilverd, J. Tamminen, C.-F. Enella, and T. Ulicha (2009), Impact of different energies of precipitating particles on NO_x generation in the middle and upper atmosphere during geomagnetic storms, *J. Atmos. Sol. Terr. Phys., 71*, 1176–1189

[65] Turunen, E., A. Kero, P. T. Verronen, Y. Miyoshi, S.-i. Oyama, and S. Saito (2016), Mesospheric ozone destruction by high-energy electron precipitation associated with pulsating aurora, *J. Geophys. Res.: Atmos., 121*, 11, 852–11, 861, https://doi.org/10.1002/2016JD025015

[66] Yamamoto, T. (1988), On the temporal fluctuations of pulsating auroral luminosity, *J. Geophys. Res.: Space Phys., 93*, 897–911, https://doi.org/10.1029/JA093iA02p00897

[67] Yang, B., E. Donovan, J. Liang, J. M. Ruohoniemi, and E. Spanswick (2015), Using patchy pulsating aurora to remote sense magnetospheric convection, *Geophys. Res. Lett., 42*, 5083–5089. https://doi.org/10.1002/ 2015GL064700

[68] Yau, A. W., B. A. Whalen, and D. J. McEwen (1981), Rocket-borne measurements of particle pulsation in pulsating aurora, *J. Geophys. Res.: Space Phys., 86*, 5673–5681. https ://doi.org/10.1029/JA086iA07p05673

[69] Zipf, E. C. (1969), The collisional deactivation of metastable atoms and molecules in the upper atmosphere, *Can. J. Chem., 47*, 1863